

**MULTI-PHOTON PHOTOEMISSION STUDY OF TiO₂ FOR
PHOTOCATALYSIS**

BY

ADAM ARGONDIZZO

B.S. in Physics, GROVE CITY COLLEGE, 2010

M.S. in Physics, UNIVERSITY OF PITTSBURGH, 2012

Submitted to the Graduate Faculty of

The Dietrich School of Arts and Sciences in Partial Fulfillment

of the Requirements for the Degree of PhD in Physics and Astronomy

University of Pittsburgh

2017

UNIVERSITY OF PITTSBURGH
DIETRICH SCHOOL OF ARTS AND SCIENCES

**This thesis was presented
by**

Adam Argondizzo

It was defended on

December 6th, 2016

and approved by

David W Snoke, PhD, Professor

Daniel Boyanovsky, PhD, Professor

Ayres Freitas, PhD, Professor

Haitao Liu, PhD, Assistant Professor

Thesis Advisor: Hrvoje Petek, PhD, Professor

Copyright © by Adam Argondizzo

2017

MULTI-PHOTON PHOTOEMISSION STUDY OF TiO₂ FOR PHOTOCATALYSIS

Adam Argondizzo, PhD

University of Pittsburgh, 2017

Titanium Dioxide has been a material of interest for almost fifty years due to its ability to photocatalyze chemical reactions on its surface under UV excitation. This thesis discusses the properties of electrons in the conduction band of TiO₂, which are probed by a variety of new experimental techniques as well as novel combinations of techniques. These measurements give insight into the electronic and photocatalytic properties of TiO₂, as well as characterizing a number of new excitations that have not been detected until now. The discovery of a transition from an occupied Ti-3d defect band of t_{2g} symmetry to an unoccupied e_g symmetry d band (d-d transitions) in TiO₂ gives a better understanding of the electronic structure in the surface region as well as providing a new method for probing the distribution of defect carriers in the bulk and surface. Additionally this newly discovered transition allowed for the identification and characterization of the polaron character of the initial state in photoemission process. A polaron state has been predicted by the theory, but experimental verification has been hard to achieve by spectroscopic means. Finally the interactions of molecules including CO₂, CH₃OH, and O₂ with the defect states was characterized by observing the effect of molecular adsorption on the d-d transitions. By varying the temperature, surface preparation and coverage of the adsorbates, the electron dynamics and interactions of these molecules were studied and produced an increased understanding of the importance of molecular interactions in regards to photoactivity of the surface. This work advances the general knowledge of TiO₂ and gives a solid framework for determining the complex electronic interactions that define its photocatalytic activity.

Table of Contents

<u>1. Chapter One: Introduction and Motivation</u>	<u>1</u>
<u>1.1 Motivation and Purpose</u>	<u>1</u>
<u>1.2 TiO₂ Bulk Structure.....</u>	<u>2</u>
<u>1.3 TiO₂ Surface Structure.....</u>	<u>6</u>
<u>1.4 TiO₂ Electronic Structure.....</u>	<u>10</u>
<u>1.5 Molecule Adsorption</u>	<u>14</u>
<u>1.6 Excitation Techniques</u>	<u>16</u>
<u>1.7 Conclusion.....</u>	<u>17</u>
<u>2. Chapter Two: Photoemission Theory.....</u>	<u>18</u>
<u>2.1 Photoemission Spectroscopy (PES).....</u>	<u>18</u>
<u>2.1.1 Three Step Model of Photoemission</u>	<u>19</u>
<u>2.1.2 One Step Model of Photoemission</u>	<u>21</u>
<u>2.1.3 PES considerations.....</u>	<u>22</u>
<u>2.2 Two Photon Photoemission</u>	<u>23</u>
<u>2.2.1 States</u>	<u>24</u>
<u>2.2.2 Energy Spectrum.....</u>	<u>25</u>
<u>2.2.3 Excitation Schemes</u>	<u>28</u>
<u>2.3 Angle Resolved Photoemission.....</u>	<u>30</u>
<u>2.4 Time Resolved Photoemission</u>	<u>32</u>
<u>3. Chapter Three: Experimental Apparatus & Procedures</u>	<u>33</u>
<u>3.1 Non-Collinear Optical Parametric Amplifier (NOPA)</u>	<u>34</u>
<u>3.1.1 NOPA Theory.....</u>	<u>35</u>
<u>3.1.2 The NOPA Optical Setup</u>	<u>42</u>
<u>3.1.3 Operational Considerations</u>	<u>45</u>

3.2 Mach Zehnder Interferometer.....	48
3.3 UHV Chamber	50
3.3.1 Manipulator	50
3.3.2 Electron Analyzer	52
3.3.3 Delay Line Detector (DLD).....	57
3.3.4 Low Energy Electron Diffraction (LEED).....	60
3.3.5 UHV Chamber and Pumps.....	61
3.4 Sample Preparation	64
3.5 Sample Dosing.....	68
3.6 Quadrapole Mass Spectrometer.....	69
4. Chapter Four: Resonant d-d-band Transitions in TiO ₂ via Multi-Photon Photoemission	71
4.1 Introduction and Motivation	71
4.2 Experimental Details	73
4.3 Theoretical Discussion & Assignment.....	76
4.4 mpp Photoexcitation Dynamics	85
4.5 Conclusion.....	90
5. Chapter Five: Multi-Photon Photoemission Spectroscopy of Polarons on TiO ₂	92
5.1 Introduction	92
5.2 Experimental Details.....	96
5.3 Results and Discussion.....	97
5.4 Conclusion.....	106
6. Chapter Six: Multi-Photon Photoemission for Adsorbate Covered TiO ₂	107
6.1 Introduction	107
6.2 Experimental Details.....	107
6.3 Results & Discussion	108

6.3.1 2PP Spectroscopy of CH ₃ OH/TiO ₂	108
6.3.2 2PP Spectroscopy of CO ₂ /TiO ₂	116
6.3.3 2PP Spectroscopy of O ₂ /TiO ₂	123
6.4 Conclusion	127
7. Chapter Seven: Conclusion and Future Work	128
8. References	131

List of Figures

1.1 Rutile Crystal	3
1.2 TiO₂ Unit Cells.....	4
1.3 TiO₂ Bulk Structure.....	5
1.4 TiO₂ Crystalline Directions.....	6
1.5 TiO₂ STM Image.....	7
1.6 TiO₂ Energy Level Diagram.....	9
1.7 TiO₂ Band Structure.....	12
1.8 TiO₂ Imaginary part of Dielectric Constant	13
1.9 TiO₂ d-band distribution.....	14
2.1 Three Step Model of Photoemission	20
2.2 One Step Model of Photoemission	21
2.3 Universal Curve of Mean Free Path vs. Electron Energy.....	23
2.4 Standard Two Photon Photoemission Spectra	25
2.5 Two Photon Photoemission Excitation Line Profile	27
2.6 Excitation Schemes	29
2.7 Momentum Conservation.....	30
2.8 Energy Vs Momentum	31
2.9 Time Resolved Photoemission Scheme	32
3.1 Experimental Setup.....	34
3.2 White Light Distribution.....	37
3.3 Optical Parametric Amplification.....	39
3.4 Signal Wavelength vs. Phase Matching Angle	40
3.5 Group Velocity Mismatch vs. OPA Signal Wavelength	41
3.6 NOPA Schematic	42
3.7 NOPA Representative Spectra	43
3.8 DCM9 Mirrors	44
3.9 2PP Interferogram.....	45
3.10 Interferometer Setup Schematic	49
3.11 Manipulator Head.....	52
3.12 SPECS Hemispherical Analyzer.....	53
3.13 Analyzer Lens System.....	54
3.14 Sample and Analyzer Energy Levels.....	57
3.15 DLD Schematic	58
3.16 DLD and Computer Connections.....	59
3.17 LEED Operation	60
3.18 Scroll Pump Operation	62
3.19 Turbomolecular Pump Diagram.....	63
3.20 Ion Pump Diagram	64

3.21 TiO ₂ Sample Holder	65
3.22 TiO ₂ Sample Work Function via Various Preparation Methods	66
3.23 TiO ₂ LEED Pattern	67
3.24 Mass Spectrometer Readout	70
4.1 TiO ₂ d-band Excitation Diagram	71
4.2 TiO ₂ Spectra Line Profile with d-d Transition	73
4.3 TiO ₂ d-d Transition Energy vs. Momentum Spectra	73
4.4 Final State Energy vs. Photon Energy for d-d Transition	75
4.5 TiO ₂ 3d State Theoretical Band Structure and Transition Density	78
4.6 Temperature Dependent Line Profiles	79
4.7 Wavelength Dependent Line Profiles at 600 K	80
4.8 Final State Energy vs. Photon Energy at Various Temperatures	80
4.9 CH ₃ OH Dosing on Surface	81
4.10 Line Profiles of Surface Under Various Preparation Procedures	83
4.11 Multi-Photon Photoemission Spectra Under Various Laser Fluences	86
4.12 Interferometric 2-Pulse Correlation for TiO ₂ d-d Transition	87
4.13 3D Two-Pulse Autocorrelation Under High Laser Fluence	88
5.1 Polaron Cartoon	93
5.2 TiO ₂ Temperature Dependent Line Profiles	97
5.3 TiO ₂ Line Profile at 31 K Before and After Flash Heating	98
5.4 Energy Level Diagram With Changing Temperature	99
5.5 t _{2g} to e _g Transition Resonance at 300 K	100
5.6 Resonance Energy vs. Temperature	100
5.7 Final State Energy vs. Photon Energy for p & s polarization	101
5.8 Max Spectral Density of Initial State vs. Temperature	102
5.9 t _{2g} and e _g State Position Change vs. Temperature	103
5.10 Structure and Charge Density of Polaron in TiO ₂	104
5.11 Theoretical Temperature Dependence Curve	105
6.1 1ML CH ₃ OH Coverage on TiO ₂ surface	109
6.2 Increasing CH ₃ OH Coverage	110
6.3 CH ₃ OH Crystallization at 120 K	113
6.4 CH ₃ OH Temperature Dependence	113
6.5 High Temperature CH ₃ OH Dosing	115
6.6 Quenching of CO ₂ on TiO ₂	118
6.7 Warming of CO ₂ on TiO ₂	119
6.8 CO ₂ on TiO ₂ Charge Density Changes	120
6.9 Folded Oscillator Strength of CO ₂ Adsorption	120
6.10 Work Function Change with CO ₂ /H ₂ O Adsorption	122
6.11 O ₂ Exposure at 31 K	124
6.12 O ₂ Exposure at 80 K	125
6.13 O ₂ Exposure at 300 K	125
6.14 O ₂ Exposure at High Temperatures	127

List of Equations

1.1 Work Function.....	10
2.1 Photoelectric Effect.....	19
2.2 Electron Mean Free Path	19
2.3 Parallel Momentum	32
3.1 Crystal Polarization	36
3.2 Index of Refraction.....	36
3.3 Laser Pulse Intensity	36
3.4 Time Dependent Phase Shift.....	37
3.5 Intensity Dependent Frequency Shift	37
3.6 Manley Rowe Equation	38
3.7 Signal Beam Intensity.....	39
3.8 Signal Exponential Factor.....	39
3.9 Pulse Splitting Length.....	41
3.10 Analyzer Pass Energy.....	55
3.11 Analyzer Calibration Constant	55
3.12 Trim Coil Field	56
3.13 Cancelation Field.....	56
3.14 Phoibos 100 Magnetic Field	56
3.15 Electron Kinetic Energy Difference	56
4.1 Transition Dipole Moment.....	77
5.1 Polaron Coupling Constant	94

1. Chapter One: Introduction and Motivation

1.1 Motivation and Purpose

Discovery of practical methods for conversion of solar to chemical energy is an urgent task due to recognition of the harm caused by extraction and consumption of carbon based fossil fuels. With CO₂ emissions climbing ever higher, identifying and harnessing alternative sources of energy is becoming more urgent task for developing a sustainable energy economy. Titanium dioxide (TiO₂) is a material that has been studied extensively over the last 50 years for uses in clean energy technologies using the photovoltaic and photocatalytic effects.[1] Its potential uses range from solar photovoltaic cells, to photocatalytic splitting of water into hydrogen and oxygen as well as reduction of CO₂ into hydrocarbon fuels.[1-7] Almost all of the current energy problems have a potential solution involving TiO₂. In order to achieve the full potential of these technologies, one must first understand the underlying physics that drive these light-initiated excited state processes from a fundamental perspective, so that they can be enhanced and fine-tuned to deliver practical results. While the ultimate solution to the energy problem may not involve TiO₂, the understanding of what enhances, advances, and limits these reactions will help us in the search for practical solutions.

In order to gain a better understanding of photocatalysis, this thesis examines the conduction band carriers for the clean and molecule covered TiO₂ surfaces by use of ultrafast photoelectron spectroscopy. This powerful technique enables the study of electron dynamics of the TiO₂ system and its interaction with multiple species of molecules on the surface. By investigating these interactions and dynamics, I am able to advance the understanding of the TiO₂ surface and its uses as a potential source of photocatalytic and photovoltaic effects. What follows is an introduction of the TiO₂ bulk and surface structures and how they are studied in this dissertation.

1.2 TiO₂ Bulk Structure

Titanium dioxide is a large band gap semiconductor with a broad range of applications including as a white pigment in paints, pharmaceuticals, and foods. It is also used as an optical coating for self-cleaning windows, a biocompatible film on metal implants, and a dielectric film in optics. It occurs naturally in

several different structures (polymorphs) including brookite, anatase, and rutile. Here I will introduce some of the structures with a particular emphasis on the rutile polymorph, which is the material under study in this work. In order to properly understand the surface science and photocatalytic properties of TiO_2 , first one must understand the bulk crystal properties. The presentation will start by describing a stoichiometric structure, from which the surfaces and defects are derived. Next the common defects will be introduced and categorized to provide a deeper understanding of how they affect the bulk and surface properties that have been studied. Finally, I will introduce previous research, which motivated my studies. Titanium dioxide is a large band gap semiconductor with a 3.0-3.2 eV band gap. In nature it is found in three main crystallographic polymorphs, each with slightly different properties. The least studied of these forms is the brookite (orthorhombic structure with unit cell dimensions, $a = 5.436 \text{ \AA}$, $b = 9.166 \text{ \AA}$, $c = 5.135 \text{ \AA}$); it is not often studied due to difficulty in preparation of pure brookite crystals. Because its photocatalytic activity is believed to be inferior, it has not motivated much research. Anatase (tetragonal structure with unit cell dimensions, $a = b = 3.782 \text{ \AA}$, $c = 9.502 \text{ \AA}$) and rutile (tetragonal structure with unit cell dimensions, $a = b = 4.584 \text{ \AA}$, $c = 2.953 \text{ \AA}$) TiO_2 are the most abundant and the most often studied polymorphs.[8] While both exhibit photocatalytic and photovoltaic activity, anatase is the most photocatalytically active structure, and the most stable polymorph in form of nanoscale clusters.[9-11] Anatase is primarily studied in a nanocrystalline form, which is easy to prepare since it is more stable than rutile, and provides high surface area that is desirable for applications such as photocatalysis.[9,10,12] As a bulk crystal, however it is metastable with respect to thermal transformation to rutile, which is the most stable structure for large crystals. Both brookite and anatase will undergo a phase transition to the rutile phase upon heating, making their synthesis difficult.[13] Therefore the thermodynamic stability, ready availability, and ease of surface preparation make rutile by far the most studied TiO_2 polymorph in the single crystalline form. Due to its high index of refraction and birefringence, it is commonly used in dielectric coatings as well as polarization optics. However, its scientific interest primarily stems from its potential uses as a photocatalyst including for splitting of water, self-cleaning windows, environmental remediation, as well as in photovoltaic applications. Since the discovery of its ability to split water into O_2 and H_2 by Fujishima and Honda, there has been a significant amount of research on TiO_2 as a photoactive material.[1] Although the original study by Fujishima and Honda used anatase colloid, surface science experiments requiring the use of single crystals have shifted the focus to rutile, which has a similar structure but somewhat different physical and chemical properties. However, even after decades of study, a complete understanding of photoinduced processes on TiO_2 surfaces is still lacking.



Figure 1.1- Naturally occurring Rutile crystal.[14]

Both rutile and anatase forms of TiO_2 have tetragonal unit cell structures, but the nature of these structures is different. Rutile has a body centered tetragonal unit cell that can be described as a slightly stretched cube with titanium atoms making up the four corners and the center of the stretched cube, and six oxygen atoms connecting them. Anatase is stretched significantly more and has less symmetry than rutile. Figure 1.2 shows the lattice structures and unit cell dimensions for both the rutile and anatase structures.[15-17]

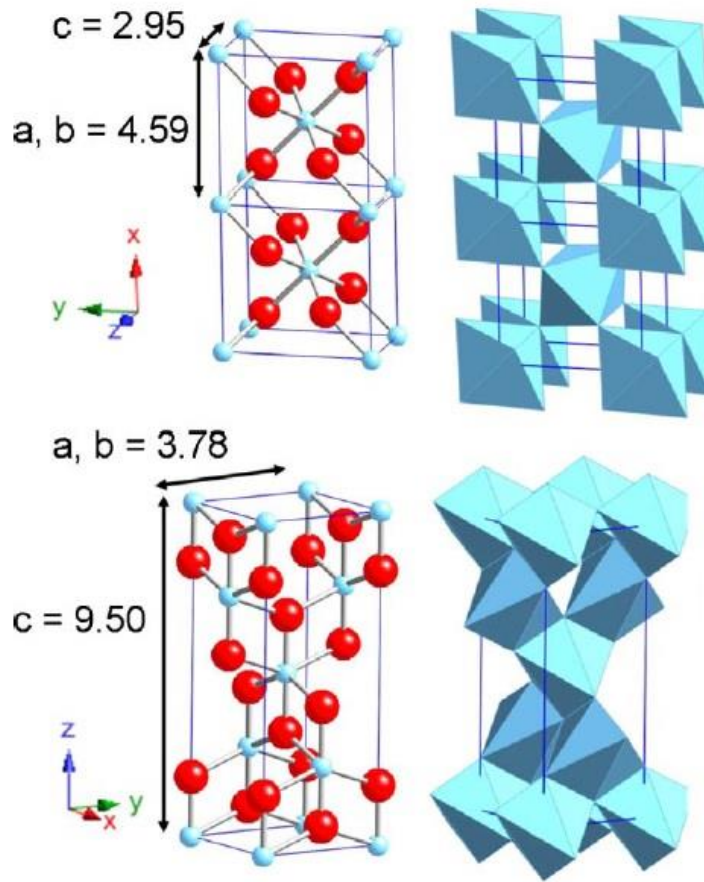


Figure 1.2 - (top) Rutile TiO₂ unit cell, (bottom) anatase TiO₂ unit cell. The smaller blue balls are the titanium atoms, while the larger red balls are the oxygen atoms. The rutile unit cell is made up of 5 Ti atoms and 6 O atoms while the anatase unit cell is made up of 13 Ti atoms and 18 O atoms. [17] The right side shows the arrangement of TiO₆ octahedra in both materials.

Both structures are composed of octahedral with a titanium atom, surrounded by six oxygen atoms in a distorted octahedral configuration. In rutile the octahedra are arranged with the long axes alternating by 90° with the body centered Ti atom at the center of an octahedron with the octahedral connected at vertices, as shown in figures 1.2 and 1.3. In anatase the center of the unit cell forms one octahedron and four others are stacked and rotated off axis from the center with one their oxygen atoms falling outside of the unit cell, and the octahedra are connected at their sides.

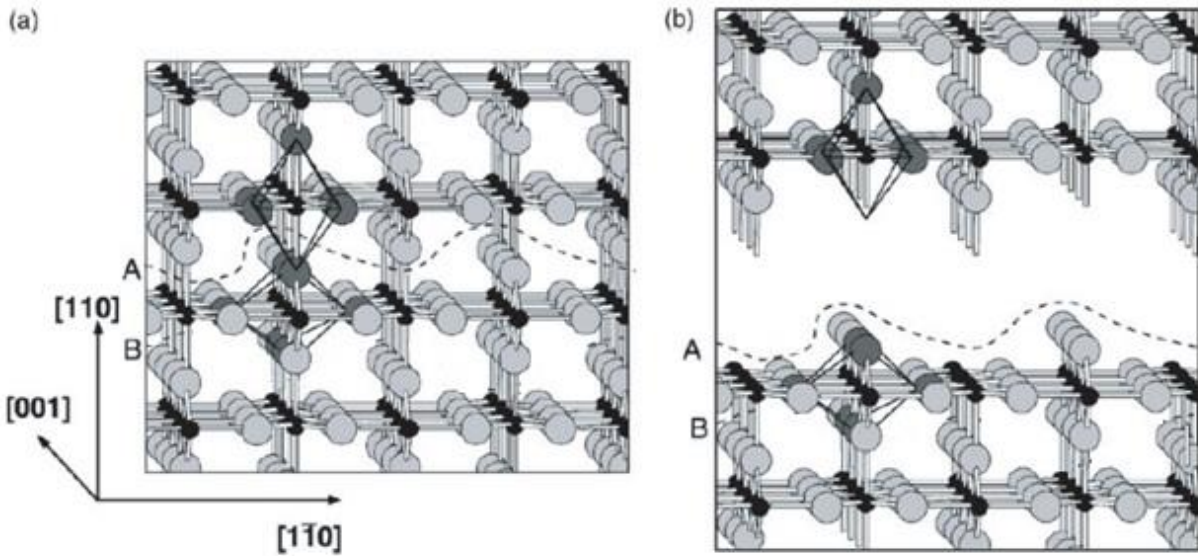


Figure 1.3 a) The bulk structure of rutile TiO_2 showing the stacking of the octahedra. b) cleaving the bulk at a (110) plane produces the (110) surface structure as shown by the area enclosed by the dotted lines. The smaller dark balls represent the Ti atoms while the larger and lighter colored balls represent the oxygen atoms.[8]

In both forms the stacking of the octahedra involves threefold coordinated oxygen atoms. Figure 1.4 shows the unit cell of rutile TiO_2 with the different crystalline directions labeled and the (110) surface plane indicated by the dashed red lines. These different crystalline faces have different stabilities. The (110) surface is most stable and therefore the most studied one.[8,12,13,18,19] Rutile TiO_2 is a positive uniaxial crystal. The high symmetry directions of the (110) surface correspond to the $[001]$ and $[1\bar{1}0]$ crystalline axes. The extraordinary c-axis is in the $[001]$ direction. Thus, the (110) surface is electrically and optically anisotropic, with $[001]$ being the slow axis and $[1\bar{1}0]$ the fast axis.[20,21] The optical anisotropy of TiO_2 is manifested in the spectroscopic studies to be described, and thus is an important part of the data analysis. This difference in the ordinary and extraordinary dielectric functions leads to strong anisotropies in the optical responses depending on the orientation of the sample and the polarization of the incident light.[15,17,20,22]

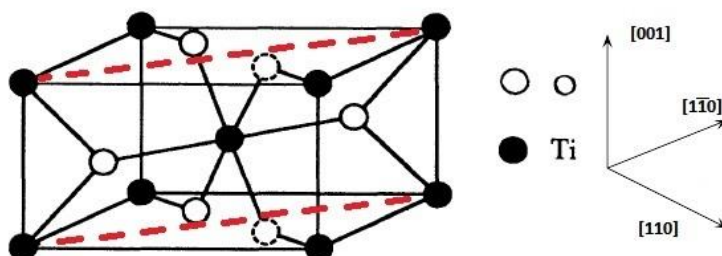


Figure 1.4- Rutile unit cell with the crystalline directions and the (110) surface shown as a cut by the dashed red lines.[22]

1.3 Surface Structure

The surface plays an integral role in the chemistry and photocatalysis on TiO_2 , and therefore it is important for interpreting the experimental results.[23,24] The ideal (110) surface is formed by cleaving the bulk crystal in the (110) plane, as shown in figure 1.3b. The 1x1 structure in figure 1.5 is the most stable for the (110) surface; it has half of the Ti atoms with six-fold coordination as in the bulk. The remaining half of the Ti atoms have five-fold coordination with one un-coordinated site in the surface. The oxygen atoms also exist two different configurations; the bulk like three-fold coordinated oxygen atoms form the surface plane, while an additional row of two-fold coordinated oxygen atoms rise above the surface plane.[8] The former oxygen atoms exist in the surface plane as indicated by the darker red balls in figure 1.5b, whereas the latter form the bridging oxygen rows. Thus, the 1x1 surface configuration corresponds to alternation of the bridging O atom rows and five-coordinated Ti atoms; it is the structure investigated in all experiments conducted in this thesis.

Figure 1.5a shows a Scanning Tunneling Microscope (STM) image of rutile $\text{TiO}_2(110)-(1 \times 1)$ surface. When tunneling into the unoccupied states the image shows alternating rows of titanium (bright rows) and oxygen atoms (dark rows) running in the [001] direction.

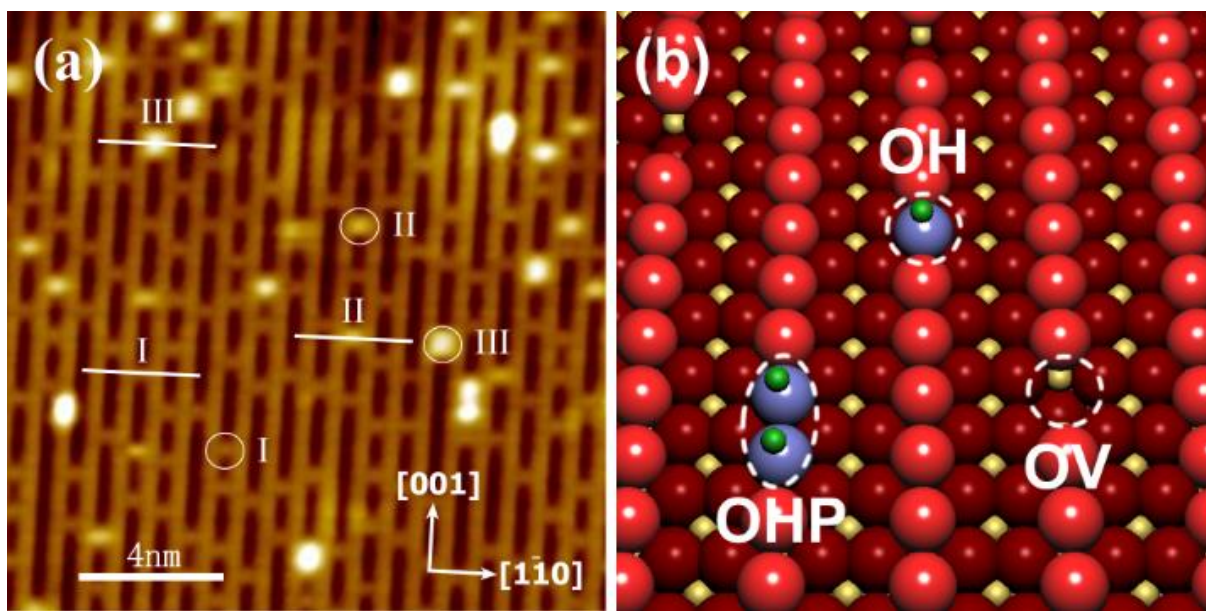


Figure 1.5- (a) STM image of TiO₂ surface. Circles indicate I - an oxygen vacancy site; II - an OH adsorbed onto the vacancy site; and III - an OH pair adsorbed onto the surface. (b) Ball and stick model of the TiO₂ surface showing rows of oxygen (red balls) and rows of titanium atoms (yellow balls), as well as the typical defects identified in (a).

When the surface is created it must relax from the bulk structure to compensate for the broken bonds. Surface X-ray diffraction experiments have shown that the surface relaxes with the six-fold coordinated Ti atoms moving upwards by $\sim 0.1 \text{ \AA}$, and the five-fold coordinated Ti atoms moving downwards by $\sim 0.2 \text{ \AA}$. [8] The oxygen atoms also move, with the bridging oxygen atoms moving downwards the most by 0.27 \AA . The moving and relaxation of the surface atoms will be important for understanding how adsorbates further modify the surface structure, as explained in chapter 6. [25,26] Heating the 1×1 surface to above 1000 K causes the surface to reconstruct into a (1×2) structure. [27] This structure has different properties and interactions and was not studied during the course of this work.

The actual TiO₂ samples are never the ideal structures shown for the bulk and the surface in figure 1.3. In order to perform photoemission experiments, the samples need to be sufficiently conductive so that they do not charge up under ionizing irradiation. For this purpose, the TiO₂ samples must be reduced to introduce n-type doping. This is accomplished by annealing the samples under UHV conditions, which leads to removal of O atoms from the surface and bulk in form of O₂ molecules. The removal of O atoms from the bulk creates interstitial Ti³⁺ ions. At the surface, however, due to the coordinative undersaturation O atoms are removed from the bridging oxygen rows. Consequently, annealed samples

have typically 10% O atom vacancy defects, as can be seen in the STM image of Figure 1.5a. The defects appear as brighter spots within the otherwise dark oxygen rows (labeled OV in figure 1.5b) in STM images of the unoccupied states of TiO₂.

For each O atom vacancy there is a charge of 2e⁻ left behind on the surface.[28,29] This charge remains at or near the surface and occupies the otherwise empty Ti-3d orbitals to form what is referred to as the defect band. This defect band is observed in photoemission spectra as a broad peak centered at ~0.8 eV below and extending up to the Fermi level. The occupation of the Ti-3d orbitals moves the Fermi level from mid-gap to about 0.1 eV below the Conduction Band Minimum (CBM).[18,30-33] Whether the defect electrons exist directly at the surface, where they can act as reactants with adsorbed molecules, or beneath the surface, where they can still be spectroscopically detected, but their interactions with molecules are more subtle, has been a subject of debate.[29,34,35]

In addition to thermal processing, electron bombardment can also increase the oxygen vacancy defect density on the surface. High energy electrons can cause the bridging oxygen atoms to desorb via an interatomic Auger recombination process.[36] This mechanism is less effective in reducing TiO₂ than thermal annealing, which may be due to smaller density of generated defects or different spatial distribution.[36] An energy level diagram with the position of the Fermi level in a reduced TiO₂ sample, as well as the defect density of states (DOS) is shown in figure 1.6.

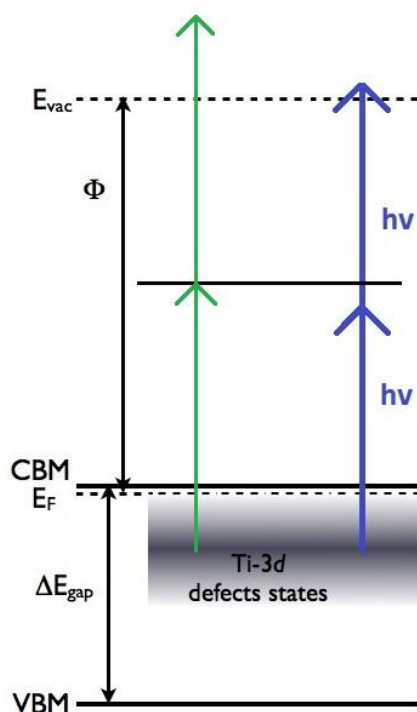


Figure 1.6- Energy level diagram of the TiO₂ gap and defect states. The defects cause the Fermi level to shift to just below the CBM and form new set of states in the gap. Blue arrows show the non resonant excitation of the surface via two photon photoemission. Green arrows show a resonant excitation of the t_{2g} to e_g transition as will be discussed in chapter 4.

The energy level diagram in figure 1.6 explains the basics of the spectroscopic studies performed in this thesis. UV light can be used as an excitation source to excite electrons from the defect states into unoccupied states above the CBM. The primary mode of probing the electronic structure and dynamics of TiO₂ in this thesis is two-photon photoemission (2PP). In 2PP experiments on TiO₂ electrons are excited from the occupied defect states directly below the Fermi level (E_F) via multiple photons (usually 2). If the excitation terminates above the vacuum, electrons can be emitted into the vacuum and detected in an energy and momentum resolved manner. The photoelectrons carry the information on both occupied states as well as unoccupied states if they serve as intermediate resonance in the 2PP process. Additional information is obtained by tuning the photon energy and thereby obtaining information on resonances between the occupied and unoccupied states. This process is the primary spectroscopic method I used for probing TiO₂ and will be discussed in greater detail in chapter 2.

In figure 1.6, another parameter that is important for 2PP experiments is the work function, ϕ , of the sample. Work function is defined as the energy required to remove an electron from the top of the Fermi level to the point where it is at rest in the vacuum just outside the surface of the material.

$$\phi = E_{vac} - E_F \quad (1.1)$$

For a nearly perfect $\text{TiO}_2(110)$ surface with minimum number of surface defects ϕ is ~ 5.4 eV.

Considering further the work function, it has both bulk and surface contributions. The bulk contribution is from the chemical potential, μ , which corresponds to the binding energy of the electrons to the positive ions forming the solid. The surface contribution is given by the anisotropic charge distribution due to electrons spilling out into the vacuum to create negatively and positively charged regions above and below the surface, i.e, a surface dipole. This surface dipole layer can be significantly modified by molecular adsorption. Chemisorption or physisorption of molecule causes charge transfer or redistribution, which modifies the surface dipole layer. As the adsorbate coverage increases, increasing the dipole-dipole interaction reduces the charge transfer to lower the free energy of the adsorbed molecules. This leads to a saturation of the work function at higher coverages. [37,38]

1.4 Electronic Structure

Before discussing the surface electronic structure and dynamics of TiO_2 , it is important to introduce the electronic structure and properties of the bulk. The band gap of a semiconductor defines the minimum energy required to excite electrons into the conduction band and holes into the valance band. The excited carriers can then be separated and used to generate a current or transferred to other materials/molecules for photocatalysis, before the electron-hole pair has a chance to recombine to convert the energy into heat or light. One of the main reasons why TiO_2 has attracted attention for photocatalytic applications is because its conduction band lies near the threshold energy for H_2 formation from H_2O , and the formation potential of O_2 is in the mid gap.

The band gap, between the valance band maximum (VBM) and the CBM, depends on the method of measuring. If measured by optical absorption an electron-hole pair is created and the optical band gap of 3.03 eV is obtained. [39,40] Alternatively, photoemission experiments measure the energies of adding

or removing an electron, and obtain the electronic band gap as the difference between electron affinity and ionization potential. The electronic band gap is larger than the optical band gap due to the excitonic binding between the electron and hole, which reduces the optical band gap energy. The electronic band gap energy for rutile TiO_2 can be measured by a variety of methods including Ultraviolet Photoemission Spectroscopy (UPS) and Inverse Photoemission Spectroscopy (IPES), which obtain the electronic gap between 3.3 and 3.6 eV. [41] [42]. All the experiments and data obtained in this thesis involve the detection of excited electrons by absorption of photons, and therefore the optical band gap will always be used.[17]

The band structure of TiO_2 has been calculated at various levels of theory. Figure 1.7 shows the DFT band structure for rutile polymorph using the GGA functional as well as the GW corrections.[17] DFT is known to underestimate the band gaps of solids, so one must resort to many-body perturbation theory to obtain more accurate results. The correction to the DFT results at the G_0W_0 level are shown by yellow dots in Figure 1.7. The calculated band structure helps to interpret experiments including angle resolved photoemission spectroscopy[43], photoconductivity and photoluminescence[40,44], x-ray adsorption spectroscopy (XAS)[24,45,46], Raman spectroscopy[40,47], and electron energy loss spectroscopy (EELS).[48,49] The DFT calculations show that the valence band is made up of predominantly O 2p states hybridized with Ti 3d states, while the conduction band is mostly made up of empty Ti 3d states. These 3d states are of pivotal importance in this thesis. [17]

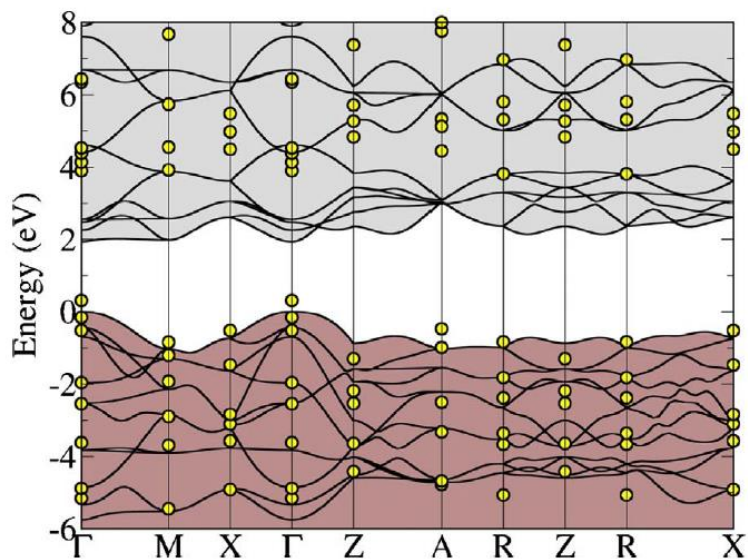


Figure 1.7- Rutile TiO₂ band structure obtained via GGA calculation (black lines). The G₀W₀ corrections to the GGA band structure (yellow dots) are shown at the critical points of the band structure [17]

Due to the large band gap, the photocatalytic and photovoltaic activity of TiO₂ are limited to the UV region. The optical absorption has a weak onset at ~400 nm (~3.03 eV) due to the direct band gap absorption, which is symmetry forbidden.[17,39,50,51] Figure 1.8 shows the measured and calculated imaginary part of the dielectric function for electric field polarization along the extraordinary and ordinary axes of rutile TiO₂; the imaginary part of the dielectric function corresponds to the optical absorption. Optical absorption at the band edge is weak, and increases to a peak around 300 nm.[52,53] Because only a small fraction of the solar spectrum can be absorbed by intrinsic TiO₂, various metals and ligands have been incorporated into TiO₂ samples, to little effect, with the goal of shifting the optical absorption, and therefore potentially photocatalytic activity, to the visible region.[2] The extraordinary axis corresponds to the [001] crystalline direction. Thus, the optical response of TiO₂ is anisotropic in the (110) plane. This anisotropy will play an important role in the reported spectroscopy and dynamics.

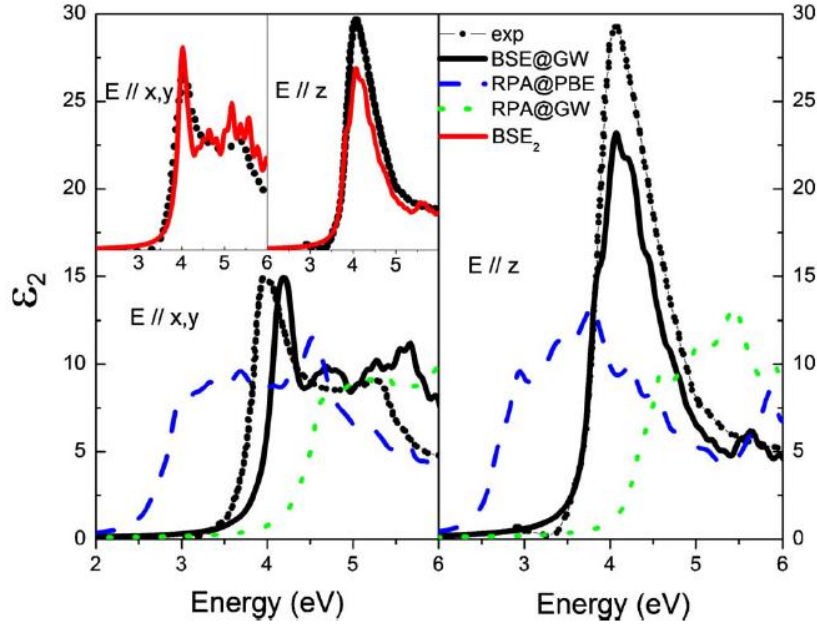


Figure 1.8 Imaginary part of the dielectric constant for rutile TiO_2 for various theoretical and experimental measurements.[17]

As previously introduced, the bulk and the surface of TiO_2 can have a number of characteristic defects. On a stoichiometric surface there are no defects, and the 3d-orbitals of Ti^{4+} ions are empty. TiO_2 is a reducible oxide, and therefore introducing defects causes the Fermi level to shift close to the CBM as the d-bands accept the excess charge. These partially filled d-bands are the initial states for photoemission in my experiments.

Upon forming a crystal the five degenerate 3d-orbitals of a Ti atom are split by the crystal field. The 3d orbitals that align with the oxygen atoms in the lattice experience a high repulsion from the electrons localized around the oxygen atoms, while the orbitals that are aligned between the oxygen atoms have a lower repulsion. In an octahedral field, three d-bands with t_{2g} symmetry move to a lower energy, while the remaining two d-orbitals with e_g symmetry move to a higher energy. [22] Therefore the defect electrons occupy the t_{2g} orbitals; they serve as the initial states for photoexcitation in most of the experiments on TiO_2 in this thesis.

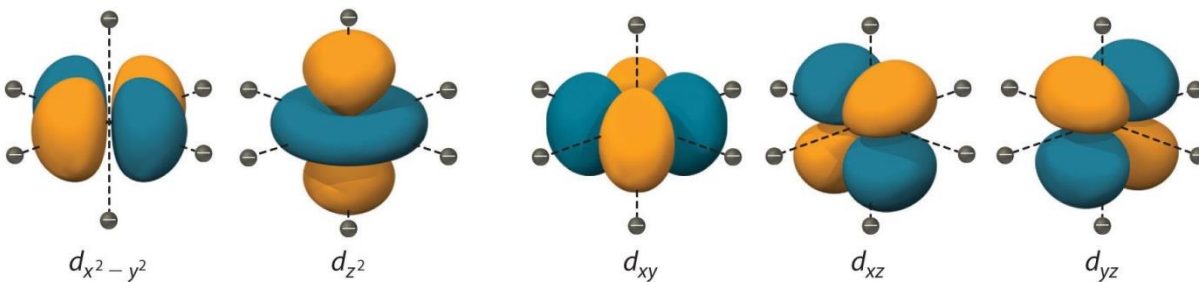


Figure 1.9- distribution of the TiO_2 d-orbitals showing their alignment in relation to the nearest neighbor oxygen atoms (gray balls). Orbitals pointing into the oxygen atoms have a higher potential and e_g symmetry while the orbitals aligned between the oxygen atoms have a lower potential and t_{2g} symmetry.[54]

1.5 Molecular Adsorption

One of the most important properties of TiO_2 is the reactivity of its surface. In order to understand it, first we must consider how molecules adsorb and interact with the surface. Atoms and molecules (adsorbates) can adsorb via two separate channels: physisorption and chemisorption. In the physisorbed state adsorbates interact weakly with the surface via the Van der Waals force with little or no charge transfer. Chemisorption involves charge exchange between adsorbates and surface leading to formation of chemical forces. Since chemisorption involves charge transfer, the bond is generally stronger than for physisorption. When H_2O or CH_3OH are adsorbed on TiO_2 , charge transfer occurs and the work function of the sample is lowered. These adsorbates are electron donors because they have relatively low ionization potential and can donate charge to the unoccupied Ti-3d orbitals of the surface. Other molecules such as oxygen are instead electron acceptors and receive charge from the sample. Finally molecules such as CO_2 are amphoteric and can receive charge at the C atom and donate charge from the O atoms. The specific molecule-surface interactions can thus change the work function in different ways. Unfortunately, in multiphoton photoemission experiments both physisorption and chemisorption can cause similar changes in the surface charge distribution and thus distinguishing the difference through photoemission alone is difficult. In general since physisorption involves weaker Van der Waals forces the adsorbed molecules should desorb at a lower energy compared to chemisorbed molecules. Using this knowledge as well as information from different experiments, such as STM, we can characterize the molecule-surface interaction.

In addition to intact chemisorption, molecule such as H_2O and CH_3OH can dissociate on the surface. For example, when water adsorbs at oxygen vacancy (O_v) defect sites on a reduced surface, it can

dissociate into OH pairs on the bridging oxygen rows as shown in figure 1.5. Consequently, if exposed to water, OH will exist on the surface at temperatures below 490 K, while above 490 K two OH species will recombine and desorb as a single water molecule.[55,56] Additionally, near room temperature, and above, oxygen dosed onto the surface will also dissociate and adsorb to fill the bridging oxygen vacancies.[57,58] This healing of vacancies is important in preparing the surface and determining the amount of vacancies that are present for adsorbing other molecules. This will be discussed at length in the experimental section dealing with adsorbed molecules. Other molecules such as CO₂ and CH₃OH can be adsorbed on the surface in addition to H₂O and O₂. [59-66] These surface adsorbates modify the work function as previously discussed, and can contribute to or remove charge from the Ti d-bands. For this reason it is important to know what is on the surface and how long can the surface remain clean before becoming contaminated by the residual gases in the vacuum chamber. In the experimental section this will be discussed further as it relates to the background gas pressure and the sample preparation. The charge transfer between the surface and adsorbed molecules has been studied in past experiments and is important for understanding the chemistry that occurs on the TiO₂ surface.[67-70] By understanding how charge is moved to or from the TiO₂ surface to adsorbed molecules we can gain better insight into how to effectively use TiO₂ for reduction or modification of adsorbed molecular species.

Previous experiments in our laboratory on the TiO₂ surface looked extensively at the H₂O or CH₃OH covered surface. This work led to the discovery of the wet electron states, where electrons transiently occupy diffuse unoccupied orbitals centered on multiple H atoms of surface OH and H₂O.[70-75] The vacancies can also be partially filled by annealing the sample in an oxygen background, causing some of the defects to heal. This healing of the defects can lead to nearly perfect surfaces with a very low defect density.[36] These experiments formed the basis for the exploration of other adsorbed molecules on the surface and how they interact with the other states on the surface, such as the d-d transition discovered by this work. The experiments in chapter 6 will expand upon this topic and provide further insight into the nature of the interaction between the surface and adsorbed molecules.

1.6 Excitation Techniques

In order to probe the spectroscopy and dynamics of TiO_2 surface, advanced optical techniques are required. Experiments using fixed wavelength excitation give limited information on the electronic structure and intermediate state dynamics that determine photoelectron distribution in 2PP spectra. The broad application of two 2PP spectroscopy was stimulated by development of femtosecond laser oscillators based on Ti-Sapphire gain medium.[76] Nanosecond and picosecond lasers could excite 2PP signal in some cases, but the time resolution and signal strengths were insufficient for measurements other than on the image potential states.[77] The pulse durations available from femtosecond laser oscillators matched well the time scales of electron dynamics in solids and thereby opened up an entirely new realm of study in solid-state physics. The primary excitation source used in previous 2PP studies of TiO_2 in our laboratory were Ti-Sapphire lasers, which are capable of <10 fs pulse generation centered at $\sim 800\text{nm}$. Ti-Sapphire oscillators typically operate at high repetition rates ($\sim 80\text{MHz}$), which makes them well suited as excitation sources in spectroscopies that count single electrons.[78] The limited tunability provided by Ti-Sapphire laser fundamental output and its harmonics could be overcome by means of optical parametric amplifiers (OPA's).[79,80]

The work conducted here uses a variant of the OPA, called the non-collinear parametric amplifier (NOPA), which adds a second degree of freedom to the phase matching condition for the parametric light conversion, namely the angle between the pump and seed beams. This added degree of freedom enables separate optimization of the wavelength and the bandwidth, allowing a broader tuning range as well as significantly shorter pulses. While traditional OPA's generally obtain final pulse widths in the <100 fs range, the NOPA configuration can generate <10 fs pulses under ideal condition. Such ultra-short pulses are beneficial for the generation of photoelectrons in multi-photon photoemission mPP experiments. [81,82]

During the course of my PhD research, I designed and built a NOPA based on the design of Riedle and coworkers[83]; this system optimizes several aspects for applications in 2PP spectroscopy by enabling generation of ultra short pulses ($<20\text{fs}$), at high repetition rates ($>1\text{MHz}$) from near-IR to the UV spectral regions (1000-220nm), with high conversion efficiency. The broad tunability, short pulse duration, and high pulse energy (up to $1 \mu\text{J}$ per pulse) enables to probe a number of systems in completely new ways. The wavelength tunability with nanometer precision enables spectroscopic studies of resonant 2PP

processes where excitation is enhanced by tuning into resonances with real intermediate states. The ability to obtain spectra where the excitation wavelength is tuned and 2PP intensity and spectra are monitored identifies previously unknown intermediate states, which illuminate the electronic structure and dynamics of a sample. In addition, high conversion efficiency delivers greater pulse energy, enabling multi-photon photoemission experiments to be performed that were previously inaccessible. In the case of metal surfaces, we have been able to observe up to 9 photon photoemission.[84,85]

1.7 Conclusion

In order to understand the photocatalytic properties of TiO₂ surfaces, a deeper understanding of the electron dynamics on the surface is needed. By studying first the clean surface, and then the adsorbate covered surface this thesis provides new understanding on the underlying processes that drive interactions on the surface and in the bulk on TiO₂. Now that the physical properties of TiO₂ and excitation techniques have been discussed in this chapter, the theory behind the photoemission experiments used will be discussed in chapter two. Chapter three will describe the experimental apparatus and its various components used for performing the experiments. In chapter 4, I will discuss the clean TiO₂ surface and how it can be probed by 2PP spectroscopy. The broad tunability of the NOPA excitation source enabled the electronic transition between d-bands in the sample to be discovered and characterized, and gave new insights into the origin and physical characteristics of the defect states of the sample as well as provided new information on how the sample optical anisotropy can be used to probe electronic transitions. Using the information provided by this first study, chapter 5 discusses the observation of a polaron state in the sample. A polaron, or lattice distortion caused by a localized electron, is important when discussing how charges move in and interact with an ionic crystal. This newly observed polaron state also provides additional information on the TiO₂ defects as well as opens up new avenues of study for how the sample changes with temperature. Finally these new techniques and discoveries are combined to obtain new information on the interaction of adsorbates with the surface. Using the previously found method of probing the system anisotropy to separate various electronic transitions, the interaction of CH₃OH with the surface is explored through a range of temperatures in chapter 6. Using knowledge obtained from the study of d-band transition I am able to determine the cause of the interaction of methanol with these electronic transitions. Additional experiments with O₂ and CO₂ are performed, which provide insight into the interaction of the surface with these materials. By looking at changes in the work function, the intensity of the d-d transition and

variations of the sample with temperature we are able to further characterize the surface and how electronic transitions are modified by adsorbed molecules.

These experiments and the new methods used represent a significant step forward in the understanding of TiO₂ electronic structure and how to analyze it. The fundamental spectroscopic studies contained here can be used as a starting point for future studies as well as applied to other materials with similar properties. This work will continue in our laboratory, expanding on what has been done to help obtain a clearer picture of the interaction of TiO₂ with adsorbates, which can hopefully advance our understanding of these processes and pave the way to new methods of improving the photocatalytic efficiency of these materials.

2. Chapter Two: Photoemission Theory

2.1 Photoemission Spectroscopy (PES)

Multi-photon photoemission (mPP) is a method for studying the electronic structure and electron dynamics of a solid-state material. The mPP method takes advantage of the photoelectric effect to excite electrons within a sample above the vacuum level, whereby they can escape into the vacuum and be collected and analyzed with respect to energy, momentum, spin, time between pump and probe pulses, etc.[86] In conventional photoemission the excitation occurs via a single photon, while the technique used in the experiments that follow utilize mPP. In mPP the pump photon excites an electron from below the Fermi level into a transiently excited intermediate state. In some cases this state is a virtual state because no optical transitions are available. Before the excited electron can decay a second photon, either from the same or a different pulse can excite that electron out into the vacuum. This broadly applicable technique is the best and easiest way to directly probe the unoccupied electronic band structure of a material.[87-91] Recent advances in laser technology and the work discussed in this thesis allowed me to enhance this technique even further by extending the wavelength coverage and measurements to higher multiphoton orders. What follows is a brief discussion on the basics of this technique, how it is used, and some points to consider.

The photoelectric effect provides us with a fundamental understanding of how to perform spectroscopy of a material by with light and detecting the consequent electron emission. A photon with energy $h\nu$ impinging on a surface with work function Δ can generate an electron with maximum kinetic energy E in vacuum given by

$$E_{kin} = h\nu - \Delta \quad (2.1)$$

As long as $E_{kin} > 0$ then the emitted electron can be detected and analyzed with respect to its energy and momentum. This allows us to map out the occupied electronic band structure of a material to a depth that is limited by the photon energy. In two-photon photoemission experiments, as will be discussed in section 2.2, unoccupied states can also be probed. With sufficiently high laser intensities and short duration pulses, the first photon can excite an electron into an unoccupied state, and the second photon can excite it further to above the vacuum level. What follows are the two basic models used to describe conventional photoemission spectroscopy.

2.1.1 Three Step Model of Photoemission

The conceptually simplest model for describing the photoemission process is the three step model. This model breaks the process into three distinct steps:[88,92,93]

1. Optical excitation of a wave packet. In the first step a photon excites an electron from either a core or valence state. The initial states are described by energy and momentum within a reduced Brillouin zone scheme. Assuming the momentum of the photon is zero, the transition is then considered a direct transition between states, modeled as a localized wave packet. If the photon energy does not match the transition energy, then the excitation is said to be non-resonant and the photon excites a “virtual” state. The difference between the state energy and the virtual state energy can be measured as ΔE which defines the lifetime of the virtual state based on the uncertainty principle. If there is no final state to excite, a single photon, or multiple photons can still excite an electron to higher energy via virtual states in a coherent excitation. As long as the excited electron has the required energy and momentum it can still be emitted in the same way.[94,95]

2. Travel to the surface. The second step of this model is the transport of the excited electron to the surface. The primary consideration is the scattering of electrons through the material on the way to the surface. The electron mean free path λ and its lifetime τ are related through the wave packet group velocity v_g :

$$\lambda(E, k) = \tau * v_g. \quad (2.2)$$

If the penetration depth of the photons is much greater than the mean free path of electrons (discussed in section 2.1.3), some reduced fraction of excited electrons will reach the surface without scattering.

The primary mode of scattering in this regime is via electron-electron interaction, although electron-phonon interactions can also contribute.

3. Escape of the electron into vacuum. The final step of this model is the transmission of electrons into vacuum. This transmission is limited to the “escape cone” in which the component of the kinetic energy of the electron that is normal to the surface is sufficiently large to overcome the surface potential barrier. An electron that does not have enough energy to overcome this barrier is reflected at the surface back into the bulk. It is important to note that the parallel component of the momentum is conserved, which will become important in the discussion of angle-resolved PES.

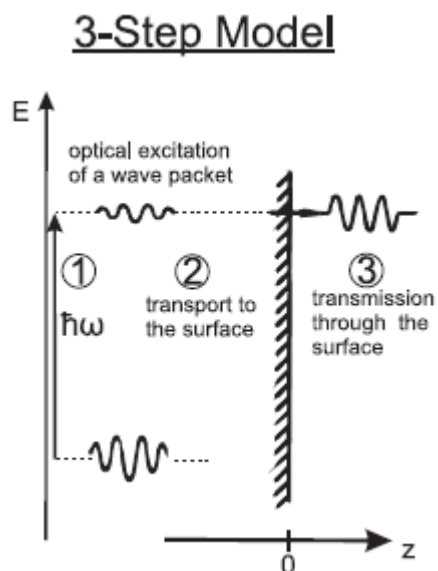


Figure 2.1- 3 Step model of photoemission, showing excitation, transport and transmission of a photoelectron.[88,96]

While the three step model is not quantum mechanically sound, it has proven adequate for analyzing and interpreting PES. The following section will briefly discuss the one step model, which is a more quantum mechanically rigorous and can describe surface photoemission.

2.1.2 One Step Model of Photoemission

While the three step model allows for a good qualitative understanding, it makes a number of assumptions and simplifications that cause it to fail under some circumstances. The three step model ignores the surface photoemission and the interference that can arise with the bulk photoemission. Also, it treats the transport of the photoelectron to the surface as a semi-classical process. The one-step model is a more rigorous description that solves these problems.[97,98]

At its core the one step model describes the dipole coupling of an electron occupying an initial Bloch wave inside the crystal with a final plane wave in the vacuum. The plane wave decays exponentially into the bulk due to scattering processes (lifetime effects) or because its penetration is evanescent. For this calculation, inverse Low Energy Electron Diffraction (LEED) states are used as the final states. In a LEED experiment a beam of monochromatic electrons is scattered from the surface potential of a crystal to generate a LEED pattern. The inverse LEED state is the outgoing scattered beam, which has the same properties as the emerging photoelectron final state. The one-step model calculates the dipole coupling between the initial Bloch and final LEED states to calculate the photoemission current. While this formalism is more accurate and produces better results, it also requires some assumptions to solve completely. [88]

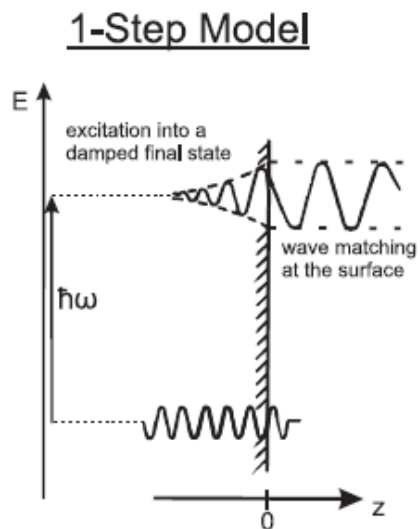


Figure 2.2- One step model of photoemission Reproduced from [88,96]

2.1.3 PES Considerations

Surface and Bulk sensitivity

PES experiments are complex in the fact that they are capable of probing both the surface and bulk electronic states of a system. The penetration of a photon into a solid de PES experiments are complex in the fact that they are capable of probing both the surface and bulk electronic states of a system. The penetration of a photon into a solid depends on the material properties. For metals typical optical skin depths are 10-20 nm, which usually exceeds the electron escape depth.[89] The finite escape depth of photoelectrons can be usually estimated from the “universal curve”.[99-101] The universal curve provides a guideline for the energy dependence of the electron scattering length in solids, which is for the purpose of qualitative discussion material independent. This curve exhibits a minimum escape depth at ~50eV from where it increases as the electron energy either increases or decreases. In my experiments on the bare and molecule covered TiO₂ surfaces with excitation photon energies below 6 eV, the photoelectron energies relative to the Fermi level fall in the 3.5-8 eV range, and therefore the characteristic probing depth is ~3-6 nm. This corresponds to approximately 10-20 TiO₂ octahedra deep. Consequently, the experiments are sensitive to both the surface and bulk states of the system. [99]pende on the material properties. For metals typical optical skin depths are 10-20 nm, which usually exceeds the electron escape depth.[89] The finite escape depth of photoelectrons can be usually estimated from the “universal curve”.[99-101] The universal curve provides a guideline for the energy dependence of the electron scattering length in solids, which is for the purpose of qualitative discussion material independent. This curve exhibits a minimum escape depth at ~50eV from where it increases as the electron energy either increases or decreases. In my experiments on the bare and molecule covered TiO₂ surfaces with excitation photon energies below 6 eV, the photoelectron energies relative to the Fermi level fall in the 3.5-8 eV range, and therefore the characteristic probing depth is ~3-6 nm. This corresponds to approximately 10-20 TiO₂ octahedra deep. Consequently, the experiments are sensitive to both the surface and bulk states of the system.[99]

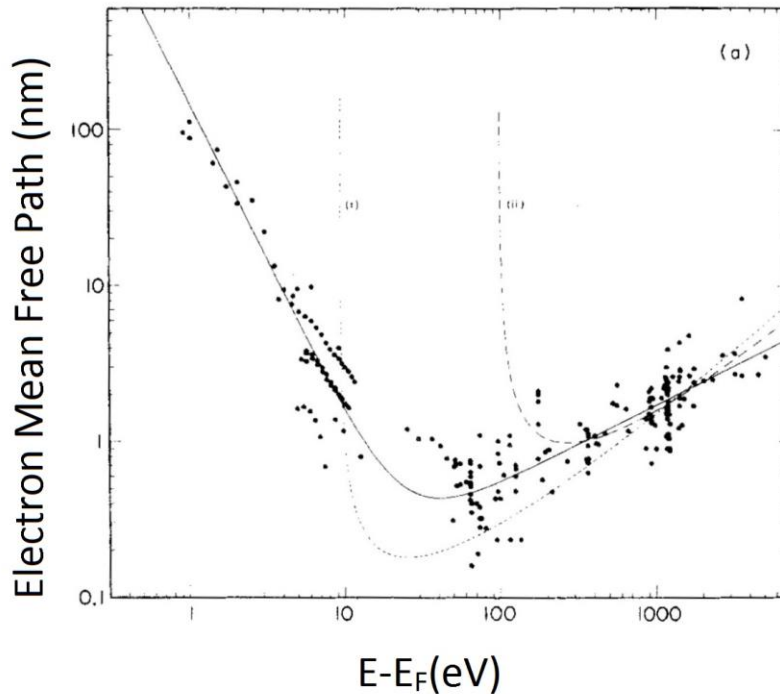


Figure 2.3- Universal curve of mean free path vs. electron energy relative to the Fermi level. This curve is compiled from a broad range of materials, and therefore it gives a broadly applicable guide for the probing depth of photoemission. [99]

2.2 Two Photon Photoemission

PES has been very successful in probing the occupied core and valance states of materials. While it allows us to obtain a wealth of information about static band structure, it lacks the ability to probe unoccupied states, or to investigate the non-equilibrium electron dynamics of a system. Two-photon photoemission spectroscopy (2PP) is a more recent development [102,103] that overcomes these limitations and allows us to look at both the unoccupied structure and dynamics to obtain a more complete understanding of both the clean and adsorbate covered materials. [104-110] Besides 2PP, an alternative method for studying unoccupied states is the inverse photoemission spectroscopy (IPES). This method uses monochromatic electrons to probe the sample and detects photon emission between the incident electron and unoccupied bands to which the incoming electron can decay by photon emission.[111] The electron energy can be fixed and the photon energy analyzed, or the detected photon energy is fixed and the electron energy is scanned. The later variant is preferred since the losses of collecting and resolving VUV photons are large. While this method is general and requires relatively

simple instrumentation, it suffers from low energy resolution and lower sensitivity than 2PP can provide. Most importantly, IPES has no direct way to probe the non-equilibrium dynamics of a system.

2PP is similar to conventional PES in that it uses a light source to photo excite electrons out of the sample. However instead of very ionizing photons, 2PP relies on high pulse intensities from ultrafast laser pulses to drive nonlinear two-photon absorption.[77,112] These higher intensities allow a photon to excite an electron below the Fermi level into an unoccupied state above the Fermi level, where a second photon will then excite the electron out of the intermediate state to an energy above the vacuum level so that it can be emitted into the vacuum and collected for analysis. The intermediate state can be a virtual state, but real states enhance the photoelectron yield. This two photon excitation is ideal for the use of pump-probe style measurements where two correlated ultrafast laser pulses are separated in time and varied to observe the momentum and energy relaxation of the unoccupied intermediate state.[95] This two step process gives rise to a number of possible excitation schemes that produce the final observed spectrum.

2.2.1 States

2PP can be considered as process where three states are coupled by dipole transitions. The first is E_i the initial energy state, which in principle can be any populated state below or within $2k_B T$ of the Fermi level. In general, the initial state belongs to a band, so the laser can excite multiple transitions for different initial state energies and momenta as determined by the resonance condition and the laser bandwidth. The second state is the intermediate state, which is generally the target of the experiment. Electrons excited from the initial states will populate an unoccupied intermediate state by resonant or non-resonant excitation. The probe pulse detects electrons excited to these intermediate states by exciting them further to above the vacuum level. The final state can be either a bulk band above the vacuum level or an inverse LEED state if no real final state is available in the bulk. Electrons can escape from the final state into the vacuum to be detected as in conventional photoemission spectroscopy. In theory these states should have a well defined energy, however in our experiments the large bandwidth of the laser as well as the broad initial states lead to a broadening of the detected states and the ability to directly detect the intermediate states even when off resonance. The use of 2PP to probe intermediate states has been used with increasing frequency in recent years as laser sources become more versatile and powerful with shorter pulses. Early studies were only possible on metal surfaces due to the comparatively high count rates compared to semi-conductors.[77,113] As techniques advanced,

probing of these states with time resolution was also possible and will be discussed in more detail below.[105] In more recent years the 2PP techniques have been expanded to include semi-conductors such as TiO_2 . [36,71,84]

2.2.2 Energy Spectrum

In order to measure the electrons emitted into the vacuum they must first be collected. Chapter 3 will be dedicated to describing the instrumentation in detail, but a brief description follows to understand how the energy spectrum is produced. Our hemispherical electron analyzer collects emitted electrons and separates them based on energy and momentum. These separated electrons then hit our detector where we then collect information on their kinetic energy, parallel momentum and the number of electrons. This data is transmitted to our software where it displays this information graphically as shown in figure 2.4.

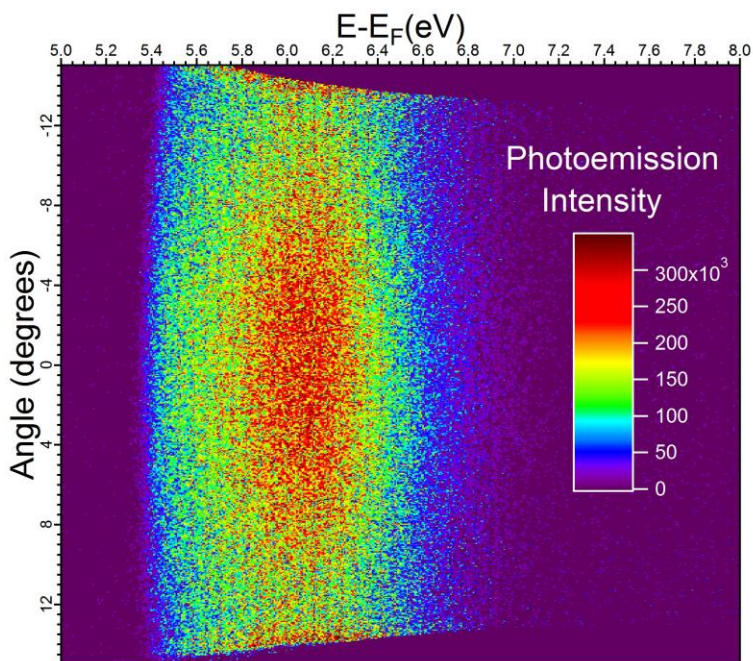


Figure 2.4- Typical data spectra acquired during experiments. The y-axis represents the angular distribution of the electrons while the x-axis gives their energy. The color scale represents the number of electrons emitted at a given point.

The emission angle on the left axis is directly related to the parallel momentum and can be converted using equation 2.4 along with the information in figure 2.4. The x-axis describes the electron energy in relation to the Fermi level (E_f), while the color scheme indicates the intensity of electrons emitted at a given point. From these three points of information, a great deal can be learned about the sample. The most common analysis done is to take a line profile along a specific parallel momentum range, giving a more easily understood representation of the energy and intensity information. Looking at figure 2.5, which is a line profile taken from figure 2.4 with a narrow momentum range around zero momentum; we can see that the recorded signal in a 2PP process ranges from the work function out to the two-photon Fermi edge. The two-photon Fermi edge is the highest energy a photoelectron can be excited to in a 2PP experiment. Higher order photoemission involving the absorption of more photons is possible so a signal can extend beyond the two-photon Fermi edge. Moreover, at finite temperatures Fermi-Dirac distributions have finite population above the Fermi edge. The electron distribution near the Fermi edge will be important in the discussion of the temperature dependence of 2PP spectra of TiO_2 . On the lower end, the onset of signal occurs at the work function edge. Electrons with energies below the work function of the sample cannot be emitted into the vacuum and are therefore not available to be collected by the detector.

Taking another look at figure 2.5 we can see that apart from the work function edge, and the Fermi edge, a clear peak is visible in the spectrum. A peak in the spectrum indicates that a large electron intensity was excited at this energy, due to a resonance with an excited state. This could be emission from a final state or multi-photon emission via an intermediate state. In the case of this example, the sample was excited with 380 nm (3.26 eV) light so one photon photoemission is not possible due to the high work function barrier of ~ 5.2 eV. Therefore only two or more photon processes will give a signal, and it can be reasonably assumed that this is a two photon photoemission process due to the peak appearing below the two photon Fermi edge.

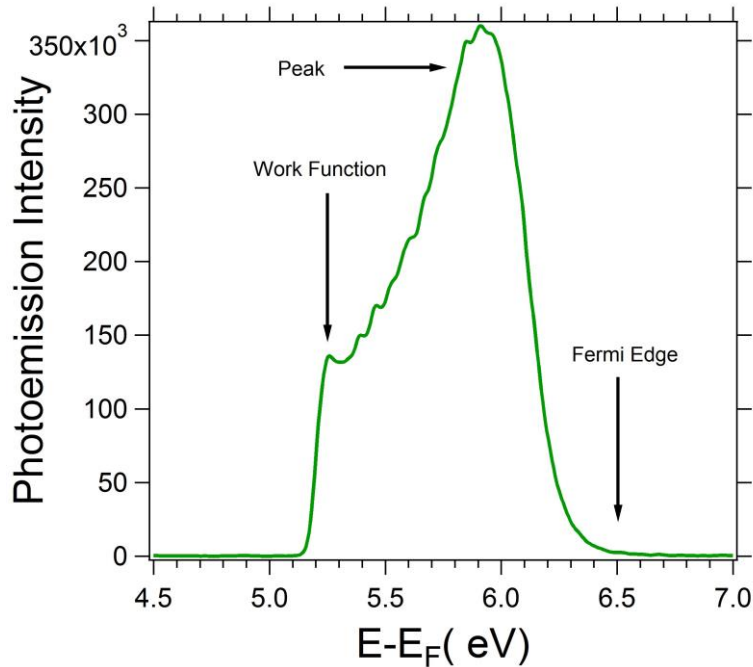


Figure 2.5- Representative line profile of 2PPE excitation showing intensity vs. energy. The onset of the signal represents the work function. The edge of the spectra at high energy represents the two photon Fermi edge, the highest energy excitation that is possible with two photons. Intermediate or final states and coherent excitations appear as peaks in the spectra.

As stated before, the photoelectron energy is measured in relation to the Fermi level, which makes analysis convenient. Since this is a two photon excitation all the electrons originate below the Fermi level, are excited above the Fermi level with one photon and then a second photon excites them into the vacuum where they have their energy recorded. This scheme is useful for quick analysis since the work function can be easily be read off the line profile without any additional considerations.

In order to determine the origin of a peak in the spectrum additional information is required. If the observed peak is due to an intermediate state excitation then tuning the photon energy will cause the peak to move in energy linearly, and with a slope of one in relation to the excitation wavelength. If this is the case, it implies that the first photon is exciting an electron to a fixed energy, i.e. an unoccupied state, while the second photon is exciting the electron from that state into the vacuum. Since the photon energy is increasing, the final energy of the excited electron will also increase in the same way. If the energy of the final electron moves with a slope of more than one, then the excitation could be from a number of different sources. First, it could be from higher order photoemission, such as a three photon process where one photon excites into an intermediate state and then two photons excite the

electron from that state into the vacuum. Alternatively, it could be from a coherent excitation from a final state directly excited by multiple photons into the vacuum. The different excitation processes will be discussed in more detail in the following section.

2.2.3 Excitation schemes

In order to accurately analyze a given spectrum it is important to understand the possible excitation pathways an excited electron can take. In our simple model we describe the excitation as between bands represented by straight lines, such as those in figure 2.6. In reality the bands on the solid are 3D with varying contours depending on the position and momentum of the electron. Looking at figure 2.6a, the first and most useful for our work is excitation via a resonant transition. The photon excites an electron from the initial state into the intermediate state E_i with $h\nu$ equal to the difference in energy between the initial state and E_i . Resonantly pumped transitions will in general have much higher intensities than non-resonant transitions due to the strong coupling and lack of intermediary steps that could reduce the signal. Due to the enhancement of the signal with a resonant transition even low intensity laser pulses are able to excite enough electrons to detect the transition. This is important when trying to detect a transition near the limit of your laser excitation wavelength. [113,114]

The second transition in figure 2.6b is from non-resonant excitation. In this scheme a photon excites an electron from the initial state, exciting an intermediate virtual state. This state decays on a time scale $\Delta\tau$ defined by the uncertainty relation with ΔE , where the ΔE is the difference in energy between the excited electron energy and the band the electron is decaying into. Typically this occurs on the fs time scale and is not easily detected due to the much lower signal compared to the resonant transition.

The third possible excitation pathway is via a virtual intermediate state. In this process a photon is absorbed by an electron exciting it to a virtual state, similar to the non-resonant transition case. However when no real state is nearby the electron can still be excited by a second photon into the vacuum. This can also be thought of as a photon excitation due to the strong laser field acting as the simultaneous excitation of the electron by two photons. This excitation will occur for all samples when the laser pulses are sufficiently intense, and gives a continuous distribution of signal out to the Fermi edge. For discrete states, this excitation will produce an additional peak that moves in energy with a slope of two when the peak energy is plotted in relation to the excitation energy. This allows the detection of occupied states, while the resonant excitation allows the detection of unoccupied states.

In the case of electrons are excited to a real intermediate state, they can relax in energy and momentum and be considered hot electrons. This distribution of hot electrons can only decay in energy via electron-electron and electron-phonon scattering so an additional reservoir of electrons in the conduction band can theoretically be detected on femtosecond time scales.

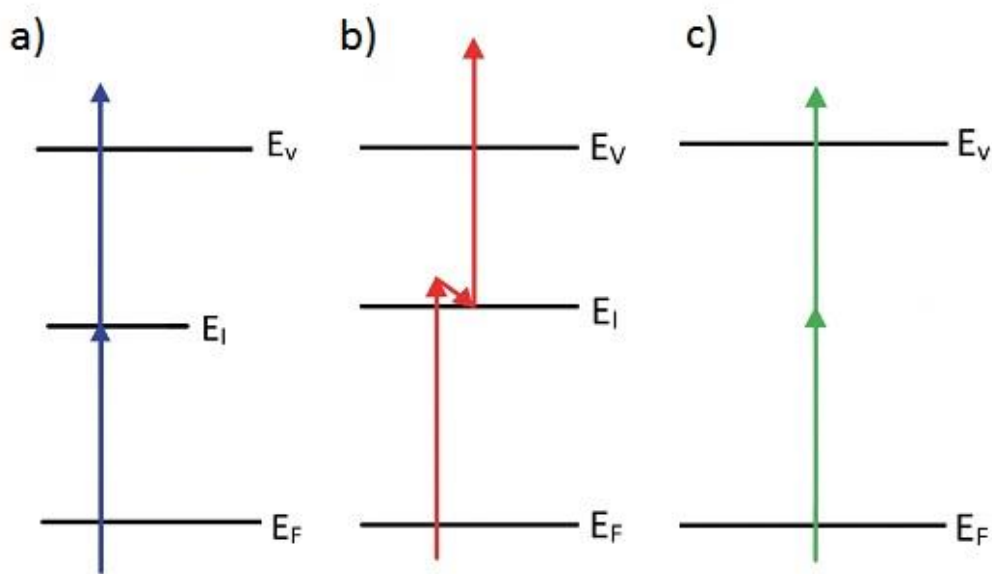


Figure 2.6- (a) Resonant two photon photoemission. (b) Non-resonant two photon photoemission. The electron is first excited and then relaxes to the intermediate state. (c) Virtual excitation, also called coherent excitation occurs even when no intermediate state is present.

By combining the energy and momentum spectra with the knowledge of the various excitation mechanisms we can accurately assign observed peaks and changes in signals to the appropriate origins and mechanisms. This makes 2PP a very powerful tool for quickly and easily detecting and assigning both occupied and unoccupied transitions on a surface. In addition to finding the energy and distribution of these states, it is important to learn of their dynamics as well. By modifying the separation between the pump and probe pulses we can obtain additional information as described in the following section.

2.3 Angle Resolved Photoemission

In addition to energy and intensity information of excited electrons, photoemission experiments also allow the collection of momentum data.[112,115] As mentioned previously, the parallel momentum of the emitted electrons is conserved. This allows us to measure this component of the momentum and get band dispersion information from the experiments along with the energy and intensity information. In order to understand what this momentum data is telling us and how to interpret it, first we need to understand how and why the momentum is conserved. Looking back at the band structure of TiO₂ in chapter one, we know that the bands are described by their energy and momentum. Electrons excited from one of the bands of TiO₂ have a given energy and momentum. This momentum can be summed up as in figure 2.7, which shows the components of electron momentum both inside and outside of a crystal. In the perpendicular direction the momentum must be sufficient to overcome the work function or the electron cannot be emitted into the vacuum.

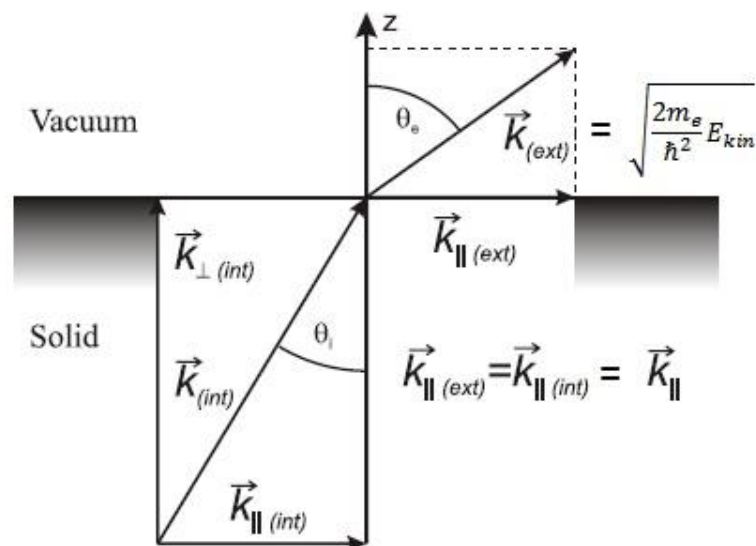


Figure 2.7- Momentum conservation of the photoemitted electron. The perpendicular momentum must be sufficient to overcome the sample work function. This specifies an emission cone of possible parallel momenta.[88,96]

The parallel momentum component, however, is unchanged upon crossing the interface as there is no potential step along that direction. This component of the momentum can be used to map the band structure of the material in question. Figure 2.8 shows typical 2D photoemission spectrum of

photoelectron counts plotted vs. energy and momentum for a clean TiO₂ surface exciting an unoccupied intermediate state. At increasing momentum the photoemission counts increase to higher energy, showing a typical dispersion relation. This dispersion can be used to find the effective mass of the electrons in the corresponding state as well as the structure of the band it originates from.

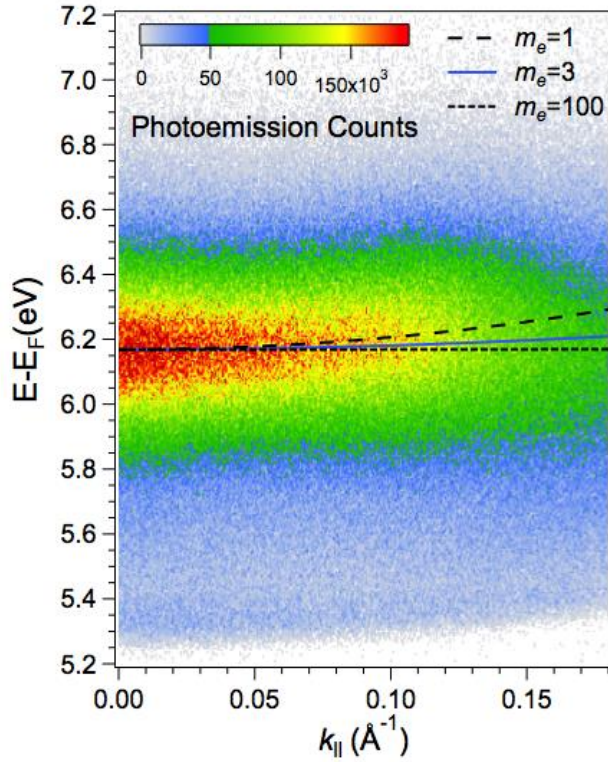


Figure 2.8- Energy vs. parallel momentum for the clean TiO₂ surface. The curvature in the work function reflects the electron escape cone. The dispersion of intermediate states can be used to determine the effective mass of an electron in an unoccupied intermediate state.[84]

This dispersion relation can be expressed by the following equation:

$$k_{\parallel}(\theta_e, E_{Kin}) = \sin \theta_e \sqrt{\frac{2m_e}{\hbar^2} E_{Kin}} \quad (2.3)$$

Using the energy and momentum information from figure 2.8 we can solve equation 2.3 for m_e to determine the effective electron mass of the excited band. Additionally we can see the onset of signal at

$E=5.2$ eV, corresponding to the work function, is consistent with the above discussion of the work function increasing in energy at higher parallel momentum values.

2.4 Time Resolved Photoemission

One final aspect of 2PP is the time resolution. The basic premise behind this experiment is that the pump and probe pulses are delayed with respect to one another in order to extract information on the lifetime of the populations being observed. The pump and probe pulse photon energy can either be the same or two different wavelength allowing for different states and energy levels to be probed depending on the system being studied.[116]

In a time resolved measurement an electron is excited from an occupied initial state below the Fermi level into either a real or virtual intermediate state. Without the presence of a second pulse the excited electrons then begin to relax. In the case of a resonant transition this can occur via two channels, electron-electron scattering and electron-phonon scattering. For the low energy electrons used in this work electron-electron scattering occurs on the femtosecond time scale, while electron-phonon scattering generally happens on the picoseconds time scale.[117-120] The dominant process for all experiments in this work is electron-electron scattering as measurements of the states lifetimes are on the order of tens of femtoseconds.[121]

In the case of non-resonant excitation, the excited electrons will decay on a time scale $\Delta\tau$ determined by the ΔE between the excited electron and the intermediate state. In a typical mpp experiment, ΔE is on the order of 0.1 eV giving a time uncertainty of ~ 5 fs. Since this is much shorter than the laser pulse duration it cannot be directly measured. On very short time scales this excitation does not conserve energy, so it will decay back to the initial state within the time scale given by ΔE . If a second pulse, often called the probe pulse, excites the sample before the electrons can relax, then the newly perturbed population distribution can be further excited into the vacuum. In the case of a non-resonant or virtual excitation the electrons will decay on the time scale of the laser pulse and no additional signal will be detected. However, if there is an intermediate state with a longer lifetime then the distribution of electrons will still be excited as the probe pulse excites the sample over longer time scales. These electrons will then be excited from the intermediate state and into the vacuum where they will generate a signal over longer timescales.[105,110] A schematic of this process is shown in figure 2.9, where the delay between the pulses is measured as Δt . This excitation can then be measured using the known

delay between the pulses to determine the lifetime of the intermediate state down to the laser pulse duration. [122,123]

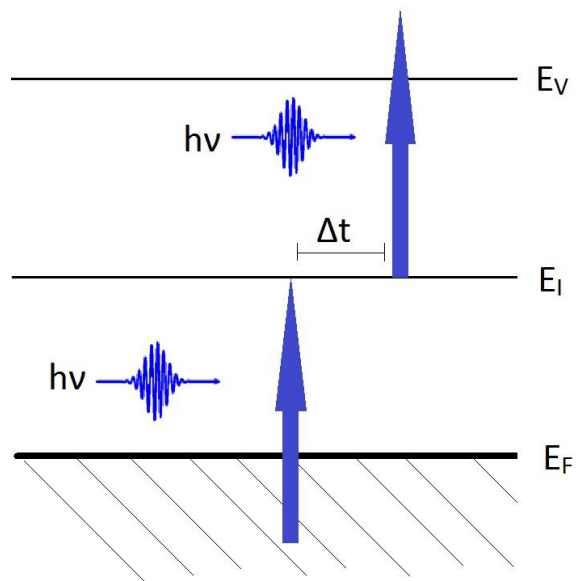


Figure 2.9- Time resolved photoemission experiment. The first pulse, called the pump pulse excites an electron into an intermediate state. The second pulse, called the probe pulse excites the electron from the intermediate state into the vacuum after a time delay t .

3. Chapter Three: Experimental Apparatus and Procedures

In this chapter the experimental apparatus and the procedure for performing the experiments will be described. The measurement of 2PP signal from semiconductors requires an advanced setup of carefully aligned equipment and instruments to prepare, characterize, excite, and measure the surface electronic properties. In figure 3.1 the set up is laid out in both the order it is used and the order it will be discussed below. Starting with the pump laser where the initial laser pulse is generated, all the way to the sample excitation and collection of data, the system must be aligned and tuned in order to accurately and efficiently measure the sample.

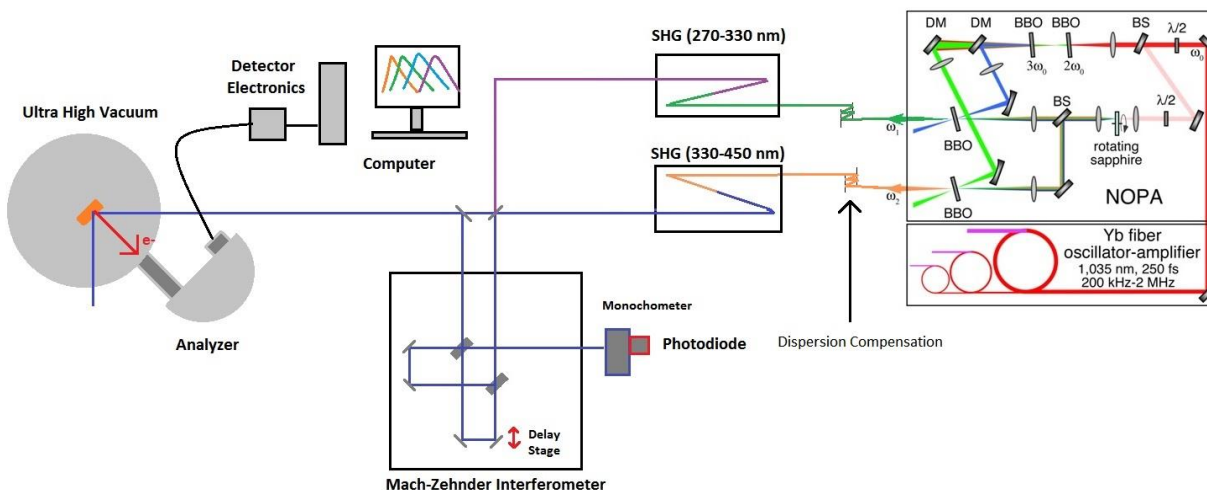


Figure 3.1- Experimental setup. NOPA system generates femtosecond pulses which are frequency doubled and sent either directly into the vacuum chamber for spectroscopy or first through an interferometer for time-resolved measurements. An analyzer collects emitted electrons and the energy and momentum information is sent on to the computer for analysis.

The following sections will describe each component of the system in detail for a better understanding of how the experiments are carried out and how the data is collected.

3.1 Non-Collinear Optical Parametric Amplifier (NOPA)

The Noncollinear Optical Parametric Amplifier (NOPA) in figure 3.1, is a broadly tunable (IR – UV) ultrafast excitation source for the experiments presented herein. During my graduate studies I built three NOPA systems, which have become the primary excitation sources for the ultrafast experiments in our laboratory. My first project after joining the lab was to design and build a NOPA system.[82,83,124] The goal of the NOPA was to provide a broadly tunable laser system with <20 fs pulses at a MHz repetition rate. The NOPA is pumped with an IMPULSE laser system from Clark-MXR Inc. This is a Yttrium doped fiber laser oscillator-amplifier system with an output wavelength of 1030 nm and a variable repetition rate of 0.2-2 MHz. The fiber laser produces ~250 fs pulses with the pulse energy fixed at 10 μ J/pulse over the range of repetition rates. The NOPA has two separate beam paths, which are pumped by the second and third harmonics of the IR fiber lasers beam. The second harmonic (515 nm) pumps one NOPA to generate tunable light 650-900 nm and the third harmonic (343 nm) pumps the second NOPA line that operates at 480-650 nm. The system is continuously tunable over these ranges and produces typically ~20 fs pulses at repetition rate defined by the pump laser. Additionally, the NOPA

output can be frequency doubled in order to obtain UV light. After doubling the outputs can reach 250-330 nm and 340-450 nm ranges.[125] The UV output is important for the study of TiO₂, because of its large band gap and work function. It is important to understand the mechanisms behind the operation of this NOPA system in order to maintain the system at optimum efficiency and maximum tunability.

Additionally, I wanted to have two separately tunable synchronous sources, which could be used for two color experiments together, or for standard time resolved experiments separately. The NOPA system has opened up new experimental capabilities because of its tunability, power, and two-color operation. The ability to finely tune the wavelength of the light allows us to tune into spectroscopic resonances of the materials under study. The high pulse energy, combined with the short pulse duration and the MHz repetition rate allows us to excite multi-photon photoemission, ranging from one up to nine photon processes. The same resonant transitions can be excited by one, two, or even three photon absorption. This incredible range, combined with the broad spectrum of light has significantly advanced our ability to study metal and semiconductor surfaces. As will be shown in the following sections, even seemingly simple experiments and previous results can be examined and new information gleaned by use of the NOPA laser system.

3.1.1 NOPA Theory

In order to generate a tunable output pulses, a pump and a seed beam must be combined inside a non-linear crystal, whereby a certain wavelength within the seed beam is amplified. In order to accomplish this, a process known as parametric down conversion is used. Parametric down conversion can be a spontaneous process that builds up from vacuum fluctuations of the electromagnetic field when focusing a coherent beam of high intensity into a non-linear crystal with a large χ value. χ is the electric susceptibility of a material that determines its polarizability. In a crystalline material the polarization of the material depends on the incident electric field. With anisotropic crystals that lack inversion symmetry, such as β -Barium-Borate (BBO), this polarization has a non-linearity that can be expanded to the second order as [126]

$$P = \sum_j \chi_j E_j(t) + \sum_{j,k} \chi_{j,k}^{(2)} E_{j,k}^2(t) \quad (3.1)$$

Where the value of $\chi^{(2)}$ is the second order non-linear optical susceptibility and a property of the material that produces a non-linear component to the polarization. Vacuum fluctuations in the crystal cause some of the pump photons to spontaneously split into two photons of different wavelengths.

These photons are confined to two overlapping cones, where the frequencies and k-vectors of the emerging beams are arranged to conserve both energy and momentum. The spontaneous parametric emission can be detected if the pump intensity is sufficiently high. The threshold for the parametric process can be greatly reduced and the process controlled to generate a specific wavelength by introducing the seed beam. This seed beam is amplified in the parametric conversion. To conserve energy and momentum an idler beam is also produced, but it not used in our experiments due to its generally lower photon energy.

In order to understand the NOPA better a more detailed look at each of the processes is required. First is the generation of a white light continuum that is used as a seed pulse for the NOPA process.[127] This white light is generated by focusing ~20 % of the IR pump beam into a 3 mm thick, c-cut sapphire crystal. The white light generation occurs via a combination of processes. The two most important of these are the optical Kerr effect and self-phase modulation.[128,129] The optical Kerr effect is an intensity dependent modification to the index of refraction as expressed in equation 3.2. $n(I)$ is the combined index of refraction, including the static frequency dependent n_0 and an intensity dependent contribution n_2 which defines the intensity $I(t)$ dependence:

$$n(I) = n_0 + n_2 * I(t) \quad . \quad (3.2)$$

Where there intensity, $I(t)$, is a Gaussian pulse of duration τ given as:

$$I(t) = I_0 e^{-\frac{t^2}{\tau^2}} \quad . \quad (3.3)$$

By focusing the white light generation beam into the sapphire plate an intensity on the order of 10^{16} W/m² is achieved. The pump pulse intensity changes the index of refraction nearly instantaneously as it passes through the sapphire plate. Self-phase modulation (equation 3.4) is the effect whereby the changing index of refraction causes the laser pulse to experience a time dependent phase shift.

$$\varphi(t) = \omega_0 t - \frac{2\pi}{\lambda_0} n(I)L \quad (3.4)$$

Since the index of refraction is intensity dependent, taking a time derivative of the phase gives the intensity dependent frequency shift in the spectrum as shown in equation 3.5.

$$\omega(t) = \omega_0 + \frac{4\pi n_2 I_0 L}{\lambda_0 \tau^2} t e^{-\frac{t^2}{\tau^2}} \quad (3.5)$$

At sufficiently high intensities the time dependent frequency translates into shifting and broadening of the spectrum from IR to blue-green light. This resulting spectrum with a maximum at 580 nm and half-width of ~100 nm is shown in Figure 3.2. This spectrum is relatively constant since there is a narrow range of power between the output for generating the continuum and the damage limit of the sapphire crystal. This white light continuum has a large up-chirp, which separates different frequency components in time; this is important for selection of the amplified wavelength.

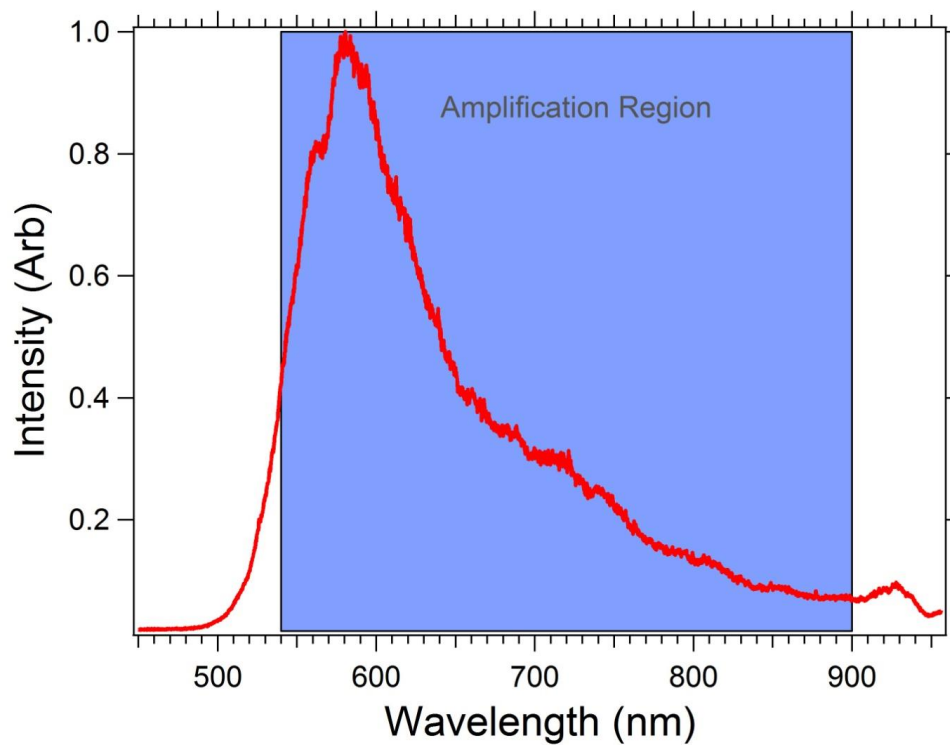


Figure 3.2- White light spectrum generated by the sapphire crystal. The blue shaded region represents the primary region of amplification by the NOPA system. Amplification at the spectral edges can be achieved by modifying the white light steering and focusing to obtain greater in the blue-green region while sacrificing the intensity in the shaded region .

To amplify the white light, either the second or third harmonics of the pump beam are necessary. The requisite harmonics are generated by frequency doubling of the pump beam and sum frequency of the second harmonic and the fundamental in separate BBO crystals. The pump harmonics are combined with the white light continuum in BBO crystals to generate the NOPA output. The noncollinear

parametric amplification occurs by focusing the pump and white light beams into the BBO[130,131] crystal. When the seed and pump beams are spatially and temporally overlapped inside the crystal a mixing occurs based on the Manley-Rowe equation [132,133] (Equation 3.6). The seed beam is amplified generating the signal beam according to equations 3.6-3.8.

$$\frac{1}{\omega_i} \frac{dI_i}{dz} = \frac{1}{\omega_s} \frac{dI_s}{dz} = \frac{1}{\omega_p} \frac{dI_p}{dz} \quad (3.6)$$

Where the intensity of the signal is given by:

$$I_s \approx \frac{1}{4} I_{s0} e^{2L\Gamma} \quad (3.7)$$

With

$$\Gamma^2 = \frac{8\pi^2 d^2 I_p}{n_i n_s n_p \lambda_i \lambda_p \epsilon_0 c_0} \quad (3.8)$$

The subscripts s, p, so, and i stand for the signal, the pump, the seed, and the idler beams. The equations indicate that the intensity of the output signal beam is linearly related to the seed beam power (I_{s0}), but exponentially dependent on the pump pulse power (I_p). Since both the pump and seed beam powers are split from the same initial pulse, it is important to have enough light to generate the white light spectrum, but also to have as much power as possible in the pump beam to optimize the signal beam power. The signal and the seed beams are collinear and emerge as the output of the NOPA. The Pump and the Idler beams are noncollinear with the signal, and therefore are both blocked after the amplification as they are no longer required. A more detailed derivation and explanation of the parametric amplification can be found in the work of Cerullo et al.[128]

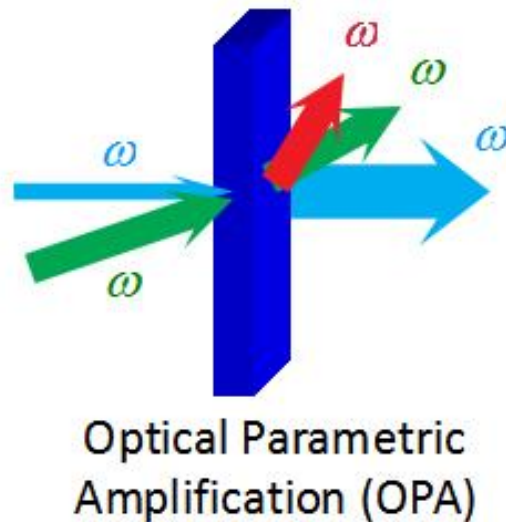


Figure 3.3- OPA schematic diagram showing the transfer of energy between beams. A seed beam of frequency ω_1 is amplified by a pump beam of frequency ω_3 . An idler beam of frequency ω_2 is generated in order to conserve momentum and energy.

The amplified wavelength is selected by several parameters. The most important parameter is the temporal overlap between the pump and seed beam, which as previously mentioned is affected by the significant up-chirp of the seed beam during the white light generation process. This enables us to choose the wavelength of light which is overlapped in time with the pump pulse in the BBO crystal just by changing the time delay of the pump beam. This “seeds” the parametric down conversion process at the desired wavelength. Additionally, the phase matching angle between the crystal, the seed, and the pump beams determines which wavelengths can be efficiently amplified. In a collinear setup this is difficult because the seed and pump beams are coincident, leading to a strong dependence of the phase matching angle on the wavelength. By separating the pump and seed beams by a small angle, α , the wavelength dependence of the phase matching angle is greatly diminished, allowing for easier amplification over a large wavelength range, as shown in figure 3.4 for a pump wavelength similar to the third harmonic of the NOPA. The difference in wavelength will cause a slight shift in the signal wavelength axis but is otherwise a good representation of both NOPA lines. This relative insensitivity to the crystal angle over a large wavelength range also enables amplification of broader spectra, and therefore shorter pulse generation, than can be achieved in a collinear arrangement. In my system the angle α is typically set to 3 degrees to allow for maximum tuning potential.

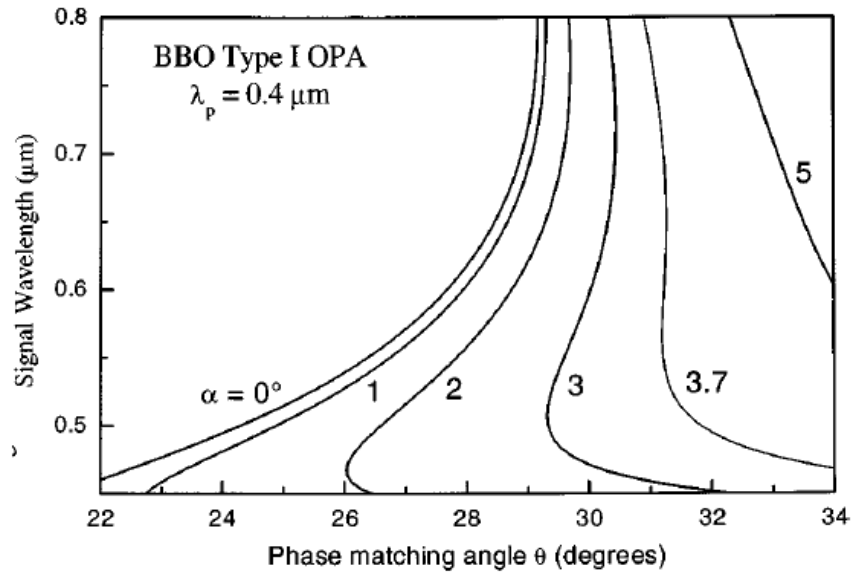


Figure 3.4- Signal wavelength vs. phase matching angle for Type I BBO for various non-collinear angles. Increasing the angle between the crystal and the incoming beam decreases the wavelength dependence of the phase matching angle allowing for a wider amplification range and bandwidth. [128]

The final important parameter is called the pulse splitting length and is related to the mixing of the pump and seed beams inside the crystal. Due to the differing wavelengths of the pump, seed, and signal pulses the amplification process only occurs while the beams are overlapped in space and time. The overlap can be achieved over a distance L , as given in equation 3.9 below, and is determined by the group velocity mismatch, δ_{sp} , and pulse duration τ . Figure 3.5 shows how δ_{sp} varies with the signal wavelength being amplified for different crystal cuts. In my system the BBO crystal is cut in a Type I configuration as shown by the middle curve in figure 3.5. Additionally since the beams are non-collinear the distance must be further adjusted to account for the slight angle between the beams. For distances greater than L the pulses separate inside the BBO crystal and amplification no longer occurs.

$$L = \frac{\tau}{\delta_{sp}} \quad (3.9)$$

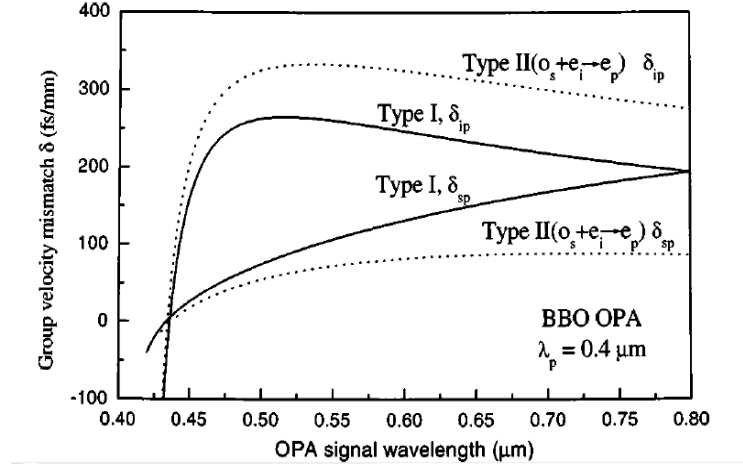


Figure 3.5- group velocity mismatch vs. OPA signal wavelength. The curve for δ_{sp} is shown for determining the pulse splitting length where the amplification of the signal stops for two overlapped beams in a BBO crystal.[128]

The multiple theoretical aspects of the NOPA operation need careful consideration in the optical design. By considering different aspects of the NOPA operation we can see that in order to maximize the NOPA output power a few things are required. First the output power scales exponentially with the pump power. This means the pump line should receive as much power as possible. However, the seed line must also have enough power to generate the white light continuum through the sapphire plate. This requires careful balance of splitting the power between the two lines to maintain maximum efficiency. In order to split the power a half waveplate is used to change the polarization of the beam and then split the beam using a polarizing beam splitter cube. This allows me to send the minimum power required for stable white light to the white light line while sending the remaining power to the pump beam. Next, the pump wavelength must be chosen to amplify a specific wavelength range that is generated by the white light spectrum, while still satisfying the energy and momentum conservation rules. Since parametric down conversion is required, the signal and the idler beam photon energies must sum up to the pump beam photon energy. With the two pump beams, energy and momentum conservation can be satisfied over the full range of our white light spectrum. Combining these important aspects leads us to the actual set-up of the NOPA system and its operation.

3.1.2 The NOPA Optical Setup

Combining all these different aspects of the parametric generation guides the final layout of the NOPA system, as shown in figure 3.6. This layout enables us to operate NOPA with the second and third harmonic pumping to produce simultaneously two independently tunable output beams. Because both beams generated by the same seed pulse they are coherent and time correlated, and therefore can be used for two color coherent, time resolved experiments. [82,83,124]

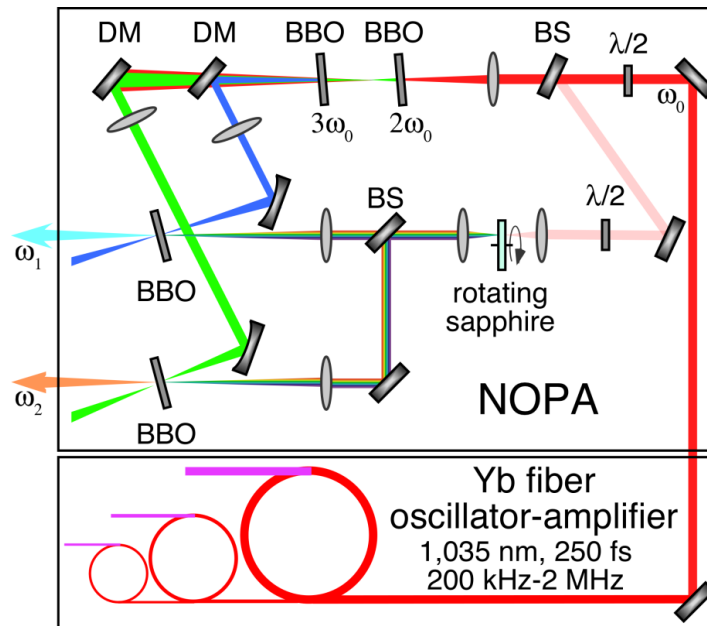


Figure 3.6- Schematic diagram of the NOPA system

The NOPA system can be tuned over the visible spectrum from 480-900 nm. The second and third harmonic pumping cover the ranges from 650-900 and 480-650 nm, respectively. The white light seed spectrum is split between the second and third harmonic paths with a dichroic beamsplitter with a 650 nm cutoff wavelength, which makes the 640-660 nm range unavailable, but this gap can be shifted by using a different dichroic optic or by replacing it with a 50/50 beamsplitter. Additionally, the output of both NOPA lines can be frequency doubled using a self-built SHG arrangement. This extends the NOPA output to the 240-450 nm range, with a gap from 320-330 nm once again due to the dichroic mirror. Figure 3.7 shows a series of sample spectra for the various wavelength ranges demonstrating the tunability and bandwidth of the NOPA output.

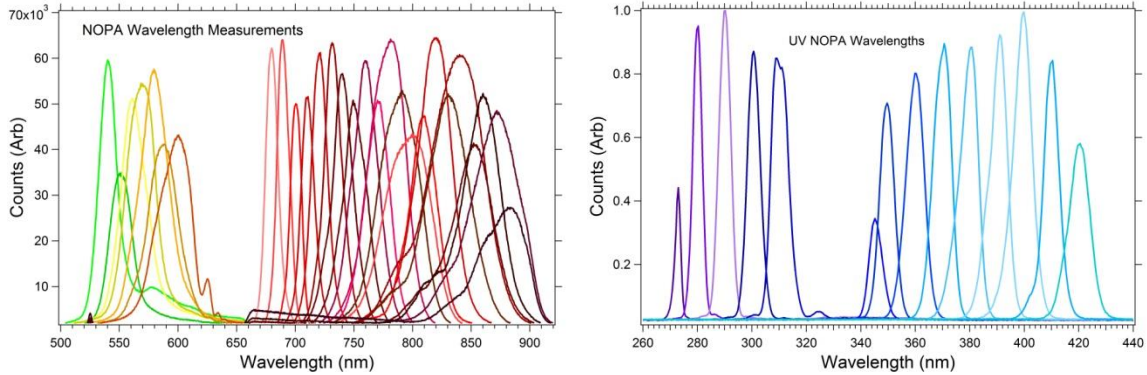


Figure 3.7- Representative spectra of the NOPA output for the fundamental NOPA output as well as the second harmonic UV spectra.

In order to achieve the broad tunability and bandwidth, careful alignment of the pump, white light, and BBO crystal angles must be considered. The angles between the pump and the white light beams and the BBO crystal relative to them are used to achieve a broad amplified spectrum. By aligning the BBO crystal axis 3-5 degrees from the signal beam, as suggested by the phase matching curves in figure 3.4, the wavelength dependence of the phase matching angle is greatly reduced to achieve a spectrally broad amplification. The output pulses can generally be compressed to ~ 20 fs.

The NOPA output pulses emerge with a large upchirp, and therefore need to be compressed before using them for second harmonic generation or experiments. In order to achieve the minimum possible pulse durations, negative dispersion mirrors are used to compensate for the dispersion introduced throughout the pulse generation process. This is performed with broadband dielectric mirrors with high reflectivity and predetermined wavelength chirp profile. The negative dispersion mirrors function by allowing the longer wavelengths to travel deeper into the dielectric stack, which increases their optical pathlength as compared with the shorter wavelengths. The coatings are designed to compensate for the second and third order dispersions of fused silica. Our application calls for a very wide compensation range and significant compression, so specific mirrors were required. I use model number DCM9 mirrors from Vteon Corporation with 30x20 mm reflective area. The large area enables multiple reflections from a mirror pair for optimized compensation. Typically the NOPA uses 8-16 pairs of bounces for minimum pulse durations. The exact number varies depending on the experiment and wavelength in use and should be adjusted accordingly. Figure 3.8 gives the calculated compensation curves of the mirrors.

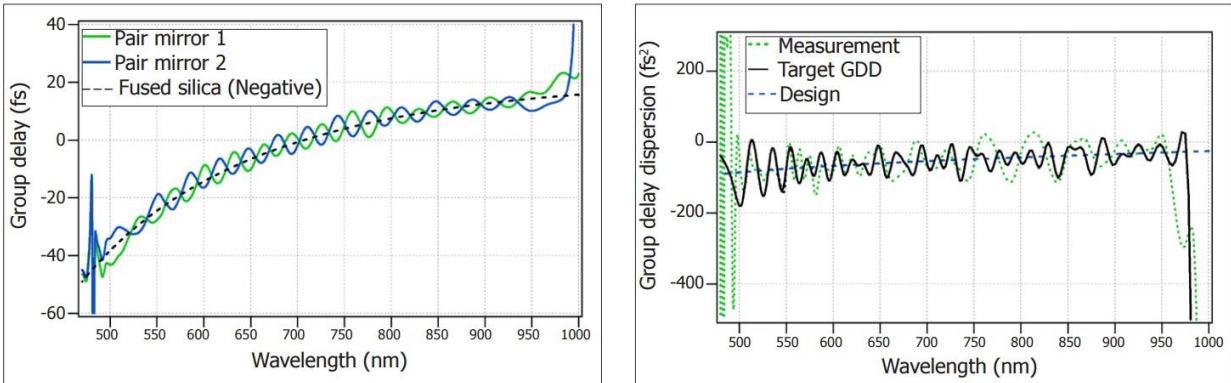


Figure 3.8- DCM9 negative dispersion compensation mirrors. These mirrors provide second and third order compensation from 500 nm to 900 nm

After leaving the NOPA the optimized pulses can be sent to a pair of second harmonic generators for UV light generation. There is a separate SHG for each output of the NOPA to allow for optimal generation. The 650-900 nm line is fed into a SHG using 15 cm focal length concave mirrors and focused onto a 0.08 mm thick BBO crystal which is cut for 750 nm light. By turning the BBO crystal angle the frequency that is doubled can be changed over the entire range of the NOPA. The mirrors after the BBO crystal are dielectric coated mirrors for 320-450 nm and allow >80% transmission of the fundamental wavelength. The second SHG is similar to the first but uses only 10 cm mirrors to allow for tighter focusing due to the lower average powers of the 480-650 nm line. The BBO crystal is cut for 550 nm light and is the same thickness as the first. The dielectric mirrors are coated for reflection of 270-330 nm and also allow for transmission of the fundamental wavelengths.

After generating the UV light, a second set of chirped mirrors is used to compress the pulses again to ensure the shortest pulse duration at the sample in the UHV chamber. In order to measure the duration of the pulses, an interferometric autocorrelation is performed using a Mach-Zehnder interferometer to scan the pump-probe delay and a polycrystalline molybdenum sample holder as the source of the nonlinear two-photon photoemission signal. I take this approach because the UV output is beyond the frequency doubling range of BBO, which can be used for conventional autocorrelation measurements. I assume that the response of the Mo sample holder is instantaneous. Additional details on the interferometer and corresponding measurements can be found below in the interferometer section. By measuring the photoemission signal while scanning the interferometer I can determine the pulse

duration of the laser to be ~25 fs for the UV pulses and ~20 fs for the visible pulses as shown in figure 3.9. [125,134]

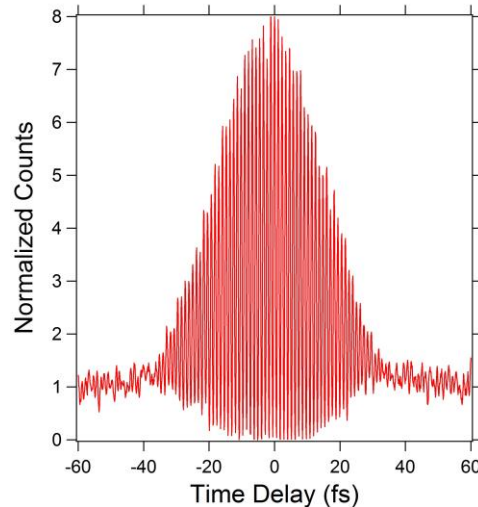


Figure 3.9- 2PP interferogram for the NOPA output at 340 nm for a ~25 fs pulse tested on a polycrystalline Mo sample holder to determine the pulse duration of the laser. For a Gaussian pulse the FWHM of the envelope divided by the Gaussian factor of $\sqrt{2}$ gives an estimate of the pulse duration for an unchirped pulse.

3.1.3 Operational Considerations

The NOPA system allows for a very broad range of tuning and various repetition rates making it the ideal source for multi-photon photoemission experiments. However this versatility comes with a number of challenges in operation. What follows is a brief description of these challenges and the strategies used to overcome them.

The Impulse laser system is essentially a black box, which should run the NOPA system continuously and without problems. However, it occasionally needs adjustment, which requires a basic knowledge of its operation. The Impulse laser is seeded by a small oscillator that generates the initial light. This oscillator is contained in a small silver box inside the Impulse. From there the beam is modelocked to generate pulses using 4 waveplates that can be externally monitored. The modelock is monitored by reading out the pulse shape on a spectrometer via an external fiber port. If the modelock is lost these waveplates can be adjusted to regain it. After modelocking the pulse is introduced into Ytterbium doped pre-amplifiers which then feed into the stretcher for shaping of the pulse. Next the pulse is fed to the final amplifier, which is a coiled fiber that amplifies the signal using a powerful diode. The pulse then exits the

fiber and is fed into a grating based compressor that compresses their duration before exiting the Impulse.

The first challenge relates to the stability of the Impulse laser system. Due to the highly non-linear nature of the NOPA, stability is key. Any slight fluctuations in the Impulse output beam will lead to much larger changes further down the line, i.e. in the NOPA generation, subsequent SHG, and finally in the multiphoton photoemission process. In order to reduce these fluctuations, a number of different techniques can be employed. First all mirrors in the NOPA system are dielectric. The high reflection and low absorption of dielectric mirrors reduces the thermal load on the mirrors, which leads to higher beam pointing stability. Additionally, the mirrors have a higher damage threshold. The IR output from the Impulse imposes between 10-20 W of power onto the NOPA mirrors, with a relatively small beam size, which would damage silver mirrors. Secondly the entire NOPA system should be enclosed to eliminate any air currents as even small changes in the air can lead to wild fluctuations of the output beam power in the NOPA. Finally, humidity control is also important for long term stability. High humidity or variations in humidity will lead to instability of the Impulse oscillator. The best approach is to carefully control the humidity of the lab, however if that is not possible, a small positive pressure of nitrogen into the Impulse enclosure can help stabilize the humidity and temperature of the system and reduce instabilities. Due to the sensitive nature of the system, it is advised to warm it up for 3 hours before use to allow all the components to reach thermal equilibrium for the most sensitive measurements.

The next consideration is that of white light generation. The white light spectrum is key to determining what range of wavelengths can be amplified and how efficiently. The systems in our lab currently use a thin sapphire plate for the generation of the white light. This produces a broad spectrum that extends throughout the visible range. Other materials can be used if the spectral needs differ. A discussion of a few of these materials can be found in the literature [127,135]. Because generation of the white light continuum requires very high power densities, damage to the crystal is a problem. However, by mounting the sapphire plate onto a rotation stage I can rotate the crystal by a few tens of micrometers every few hours to avoid the accumulated damage. If excessive power is focused into the crystal it will burn on the order of a few minutes. In order to optimize the NOPA output power and reduce damage to the crystal, only the minimum amount of pump light as possible should be diverted to the white light seed generation. For our IMPULSE system about 2 μJ per pulse with ~ 250 fs pulse duration is used to generate the continuum. Another consideration concerning the white light is that of pump light for the

NOPA amplification. Due to energy and momentum conservation only a limited bandwidth can be amplified for a given pump pulse wavelength. Both the second and third harmonics of our IR beam can be used to amplify the seed pulse, allowing us to generate a wider range of wavelengths. By having these lines separated the NOPA can be used for two color experiments by splitting the white light continuum. This can be done in two different ways, either using a 50/50 beam splitter, or a dichroic beam splitter. The advantage of the 50/50 beam splitter is that there is no spectral gap, allowing full use of the NOPA range, but that is achieved at the expense of reducing the white light power by 50%, consequently resulting in lower NOPA output power. However, a dichroic beam splitter can be used to split the spectrum by wavelength, resulting in optimal output power for both lines at the expense of a spectral gap at the cutoff point, which is mentioned above. Both of these solutions come with the problem of bandwidth over which the reflection/transmission can be made. For the extreme edges of the spectrum an alternate beam splitter can be used, or only one line can be used at a time.

The final major consideration for using the NOPA is pulse compensation. Due to the wide spectrum, broad tunability, and varying pulse widths, properly compensating the pulses can be a challenge. The one solution is to use a prism compensator, which allows variable adjustment of the compensation. However this has disadvantages that it takes up space and introduces third order dispersion. The prism compensation achieves negative dispersion by increasing the distance between two dispersing prisms, and thus requires significant space on the optical table. Moreover, this arrangement only compensates the second order dispersion, and introduces third order dispersion from the optical path within the prisms. In order to reduce space and compensate for third order dispersion, the chirped mirrors described above are used. However, since they operate by using a discrete number of “bounces” off the mirrors, the control over the exact amount of compensation is limited to the compensation per bounce. Additionally the prisms only effectively transmit about 95% of the incident light, leading to a 20% overall decrease in the output from the NOPA. The chirped mirrors however have a reflection of 99.99% leading to a significant gain in output power. I found both methods to ultimately give similar pulse durations, but with a significant space and power savings by using the compensation mirrors.

3.2 Mach-Zehnder Interferometer

Measuring the lifetime of the various states observed is an important part of understanding the dynamics of a surface. In order to accurately obtain this information a Mach-Zehnder interferometer (MZI) was built and incorporated into the experiment. A MZI operates by taking a single laser pulse, splitting it into two identical separate pulses and recombining them via a set of beam splitters (BS) and delaying one of those pulses in time by mechanical motion of a delay line. This allows two pulse correlation measurements to be performed and thereby introduces time resolution into the multi-photon photoemission experiments. Two identical custom (Layertec) beam splitters are used to split and recombine the pulses. These beam splitters are selected based on the wavelength range in question. For my experiments the primary set of beam splitters has a bandwidth of 250-450 nm, an additional set of visible light beam splitters (500-900 nm) are also available. The mirrors used must also be selected based on wavelength of which 3 ranges are available. The visible light wavelengths match well with the beam splitters at 500-900 nm, but the UV range mirrors cannot be manufactured to give high enough reflection over the same range as the beam splitters. This means that separate dielectric mirrors are required for the 270-330 nm and 330-450 nm range. Since the beam splitter does not need to be replaced, simply swapping the mirrors will allow for use of the interferometer over both ranges without extensive realignment.

The interferometer itself has two arms, which establish the pump-probe delay. One arm is adjusted with a micrometer to establish the 0 delay point, and the other has retroreflecting mirrors on a custom piezo actuated stage, which is digitally controlled by an input voltage to scan over a specified delay range. One output of the MZI goes to the sample, while the second one goes to a monochromator. The monochromator monitors the interference signal between the pump and probe pulses at the center frequency of the pulse as the delay is scanned. A photodiode monitors acquires the signal, which is sent to an oscilloscope for monitoring and computer for digitization and storing. This oscilloscope signal is used to align the interferometer for the highest fringe visibility. The digitized signal is used to calibrate the time axis for each scan. By applying a voltage to the piezo, I scan the delay for ~ 200 fs; each scan takes approximately 60 s, during which I acquire time resolved data. By repetitive scanning for ~ 100 times I can integrate the photoemission signal while using the interference signal from the monochromator to calibrate and align the time axis for all scans.

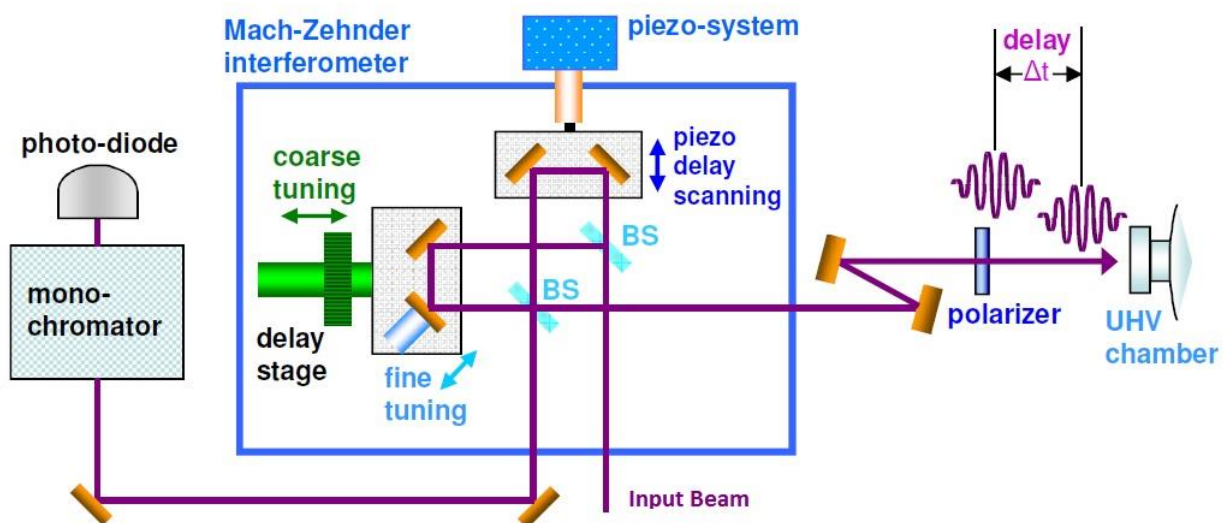


Figure 3.10- Schematic drawing of the interferometer setup with purple lines indicating beam path.[37]

In addition to performing time resolved experiments, the MZI is also used to measure the pulse duration of the laser by means of interferometric autocorrelation, as shown in figure 3.9. This is helpful in minimizing the overall dispersion in the optical path using the previously described dispersion compensation methods. By sending the pulse through the MZI and then into a non-linear crystal for frequency doubling it is possible to determine the length of the pulse.[136-138] When the one arm of the MZI is varied the pulses pass through each other in time leading to interference. At time 0 the pulses have complete constructive interference and thus have 2x the electric field, or 4x the intensity. After passing through the non-linear crystal this is multiplied to 16x the intensity. When the pulses are far apart the intensity is just 2x that of an individual pulse. This leads to a peak to base ratio of 8 to 1 for the interference pattern when properly aligned and unchirped.[139,140] For UV wavelengths the pulse cannot be frequency doubled so an alternate means of determining the pulse duration is required. In this case the MZI signal is fed into the UHV chamber where an amorphous sample holder is excited via two photon photoemission. The emitted electrons are then collected based on the scan delay of the MZI and recorded. This yields a second-order nonlinear signal similar to frequency doubling and can be analyzed in a similar way to give the duration of the pulse. In order to optimize the pulses the number of bounces on the negative dispersion compensation mirrors is varied and the envelope width is minimized

while aiming to attain the correct 8-1 ratio and keeping a flat baseline. As shown previously in figure 3.9, the UV pulses can be reduced down to ~ 25 fs using this method.

3.3 UHV Chamber

3.3.1 Manipulator

The experimental TiO_2 sample is mounted to a 5-axis manipulator within the UHV system. The manipulator gives control over the sample xyz-position, orthogonal-to-the-optical-plane and azimuthal rotation, temperature, and electrical potential with respect to the electron energy analyzer. The azimuthal rotation enables to align the sample along its high-symmetry crystalline directions. This extra axis of control is important for anisotropic samples such as TiO_2 , because optical transitions can depend on the alignment of the in-plane optical field with respect to the crystalline axes. Without this control the sample would have to be prealigned along a certain direction, and a change in azimuth would require taking it out of the chamber for manual reorientation. This would make it very difficult to make precise azimuth dependent measurements. A picture of the sample holder on the manipulator with the important elements labeled is provided in figure 3.11.

In addition to the position control, there is also an electron bombardment heater behind the sample, allowing heating up to >1000 K. A tungsten filament behind the sample holder plate is heated by passing high current (up to 2 A) through it to induce thermionic emission. A potential of 1000 V is applied with respect to the sample plate to accelerate them to high energies.

In addition to the sample heating, the sample can be cooled by either liquid nitrogen or liquid helium. Due to the thin diameter of the tubing for liquid helium applications, the use of liquid nitrogen requires a vacuum pump to pull the liquid through the manipulator. This also allows better cooling efficiency due to evaporative cooling with the nitrogen. Sample temperatures of 31 and 80 K are possible with liquid helium and liquid nitrogen cooling. Both methods rely on a continuous flow via tubing wrapped around the bottom of the manipulator, as no Dewar is used.

In order to accurately measure the temperature of the sample, two separate sensors are attached to the manipulator. On the sample holder itself is a thermocouple, which allows accurate measurement for the full range of temperatures. Due to the highly variable temperature range, as well as the need to avoid magnetic or insulating materials near the sample, a nonmagnetic type N thermocouple is used. In

addition to the thermocouple, a silicon diode is placed higher up on the manipulator near the cooling tube for low temperature. This allows monitoring of the temperature of the liquid/gas being used to cool the system. In order to accurately measure low temperatures (<50 K) with the thermocouple in the μV range, a high precision temperature controller is required. This is accomplished with a Eurotherm 2208e temperature controller, which has an accuracy of better than 1 μV . The low temperature silicon diode used with a Lakeshore model 211 temperature controller has an accuracy of better than 0.01 K. The sample is electrically isolated from the manipulator by a sapphire plate, located behind the sample holder/rotation plate, which provides good thermal conductivity at low temperatures.

Due to the sensitive nature of the photoelectron signal, care must be taken so that the manipulator does not perturb the energy and momentum of the emitted electrons. As previously mentioned this can occur via magnetic fields or charging of insulating materials. Therefore, no magnetic materials are used in the construction of the manipulator head. All screws are made of either titanium or molybdenum, while all other parts are copper. Insulating materials are kept to a minimum, and where used are shielded with molybdenum foil. If insulating materials begin to collect electrons, the effect is immediately obvious as the photoemission signal begins to move to higher energy as the charging increasingly repels the electrons.

Manipulator design is a vitally important part of the experimental procedure since there are many controls, which must be contained in a very small space while also maintaining strict operational parameters and repeatability. By having the ability to control these aspects of the sample precisely the advanced design of the manipulator lets us probe aspects of the electronic structure of the sample that were previously inaccessible. In the course of my experiments I found that due to the precise nature of the manipulator and the stress of thermal expansion and contraction over multiple cycles, the azimuthal rotation is prone to failure. The rotating part of the sample holder is held to the manipulator by a series of screws that connect it to rotation. Over time these screws can come loose and the assembly fail. Additionally there are a number of springs and bearings that allow the sample holder to stay in contact with the manipulator but still rotate. These are degraded by continual thermal cycles and need to be replaced after extended operation.

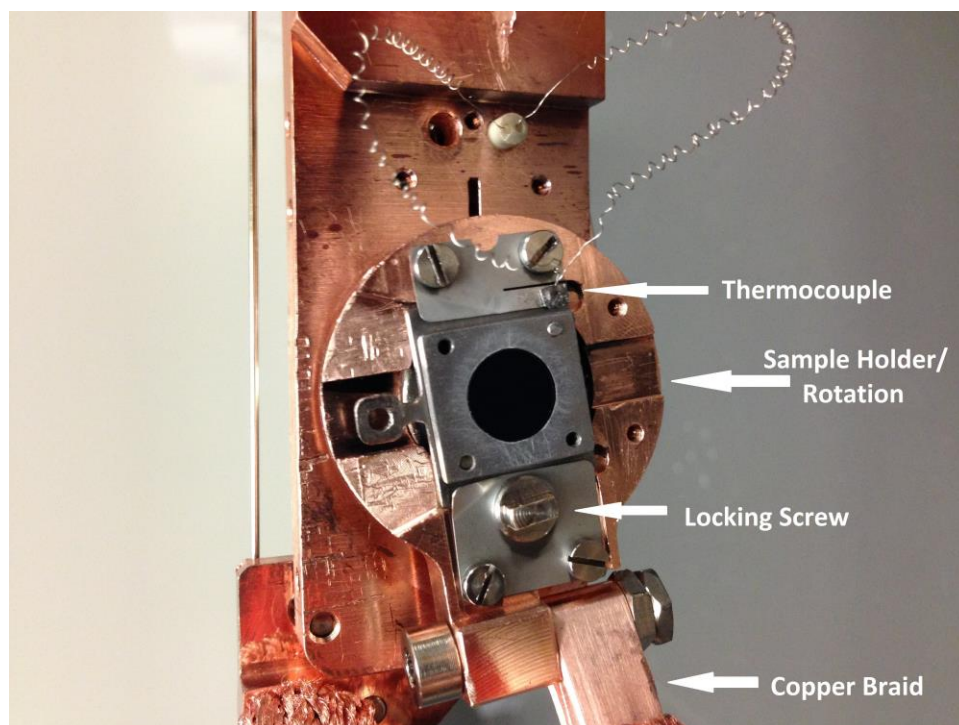


Figure 3.11- Picture of sample manipulator head. The sample is seated in a holder that can be removed for sample transfer. The plate is locked to a rotating holder, which defines the azimuthal angle. A thermocouple is affixed to the sample holder slot to measure the sample temperature as close to the sample as possible. A copper braid connects the sample holder with liquid He cooling block for cooling the sample; it is electrically floating with respect to the grounded manipulator.

3.3.2 Electron Analyzer

Next I will describe the main instrument for the data collection, the hemispherical electron energy analyzer. I will start with an overview of the analyzer itself and its operation, then go into the specifics of my experiments and how the analyzer is used. The primary experimental measurement performed in the conduct of my research is the analysis of electron energy and momentum following a multiphoton photoexcitation process leading to photoelectron emission. The photoelectron energy and momentum analysis is performed with a SPECS Phoibos 100 Hemispherical Electron Analyzer. The analyzer itself is made up of a few elements with specific functions as shown in figure 3.12 below. First, an electron lens assembly collects electrons emitted from the sample within an angular cone that captures a range of emission angles for the analysis of photoelectron parallel momenta. The lens focuses the captured electrons onto a slit at the entrance to the energy filter. An entrance slit, of selectable width, transmits a certain fraction of electrons. The slit width serves as a 1D filter along the energy axis that determines

both the electron transmission as well as the analyzer resolution; a smaller slit allows fewer electrons but gives a higher energy resolution. The electrons then enter the hemispherical region where a voltage is applied between the hemispheres to filter the electrons based on their kinetic energy. The applied voltage selected by the user causes electrons in a selected energy range to curve around the hemispheres and be transmitted, as shown in figure 3.12. The transmitted electrons are dispersed along one axis based on the radius of path they take due to the applied field. This energy spectrum is detected along one axis of an imaging detector. Figure 3.12 shows a cut away schematic of the analyzer with the electron path indicated in red.

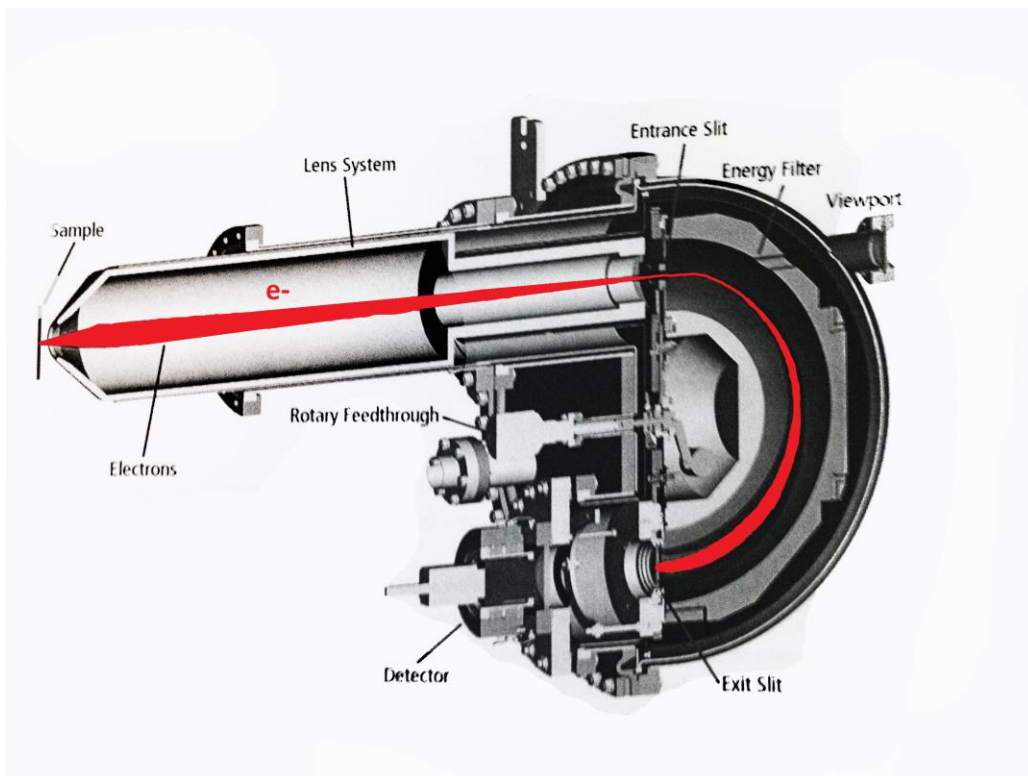
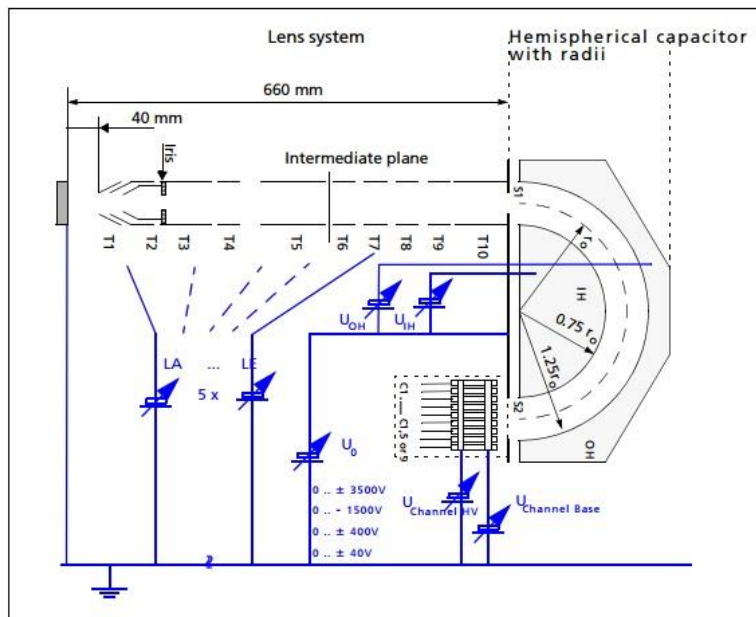


Figure 3.12- SPECS hemispherical analyzer[141]

In order for the analyzer to function correctly the electron lenses must be properly adjusted and have the correct voltages applied. The optimal sample distance from the entrance of the lens system is 40 mm as pictured in figure 3.13. The lens is not movable, so the sample and the laser excitation spot must be aligned to the lens by visual examination using a viewport, which is coaxial with the lens axis. Additionally an iris is also included between the sample and the entrance slit, labeled by a viewport in the figure, to ensure the sample is properly centered. The lens assembly itself, as pictured in figure 3.13

consists of ten separate transfer lenses, each of which is held at a potential to ensure proper guiding of electrons. A number of different preset lens modes with predefined lens potentials are provided by SPECS to allow for different imaging modes under computer control. The experiments carried out in this work exclusively use the wide angle lens mode which allows collection of electrons with a broad range of momenta. This enables the maximum range of photoelectron momenta to be recorded orthogonal to the energy axis by the 2D detector.



Analyzer main components and voltage principle

U_0	main retardation voltage numerically equal to - kinetic energy (E_{kin}) + pass energy (E_p) + workfunction (WF)
$U_{Channel HV / Base}$	anode / cathode potential for the channeltrons
$U_{HV} - U_{Base}$	detector voltage
$U_{ChannelBase} - U_0$	conversion voltage
LA..LE	lens potentials
IH, OH	inner / outer hemisphere
T1 to T10:	electrodes of the multi mode transfer lens
S1:	hemispherical capacitor entrance slit
S2:	hemispherical capacitor exit plane
IH:	inner hemisphere
OH:	outer hemisphere
r_0 :	nominal capacitor radius (100 or 150 mm)
C1 to C9:	discrete collection, single / multichannel detector (1, 5 or 9 channels) single channel detection (SCD), multi channel detection (MCD)

Figure 3.13- Lens system diagram for analyzer. A sample distance of 40 mm is required to ensure proper electron focusing via the 10 different lens elements before entering the energy filter.[141]

The specific function of the energy filter is as follows. The filter has a 100 mm center radius with the inner and outer metallic hemispheres of 75 and 125 mm surface radii, respectively. The entrance and exit slits, marked S1 and S2 on figure 3.13 mark the start and end of the hemispherical path. In order for an electron to pass without hitting the inner or outer hemispheres it must have a kinetic energy given by the pass energy (E_p) of the filter:

$$E_p = -q * k * \Delta V \quad (3.10)$$

where q is the charge of the particle, k is a calibration constant and ΔV is the potential difference between the hemispheres. The calibration constant is determined by the inner and outer hemisphere radii as defined by the following equation.

$$k = \frac{R_{inner} * R_{outer}}{2R_{center}(R_{outer} - R_{inner})} = 0.9375 \quad (3.11)$$

If the impinging electron satisfies these conditions it passes through the hemisphere and then through the exit slit. The exit slit in our case is just a fully open hole with no actual slit, allowing all electrons to pass. After exiting the slit, electrons emerge from the dispersive region and impinge on a microchannel plate (MCP). The purpose of the MCP is to amplify the incoming single electrons into electron pulses with a high spatial resolution. These secondary electron pulses represent single electron events, which are recorded by the detector to be discussed below.

Next, I introduce some of the corrections and considerations involved when operating the detector in order to obtain clean and well corrected data. The trajectory of the electrons is very sensitive to external fields. In order to reduce the effects of these fields two different methods are used. The first is to use Mu-metal shielding. Mu-metal is an alloy of nickel and iron with a very high permeability, resulting in low frequency or static magnetic fields being guided by the shielding instead of penetrating it. This reduces the deflection of electrons by stray magnetic fields, giving higher resolution and less error in measurement. The second method of reduction is via a trim coil around the outer hemisphere of the analyzer. This wire coil can have a current applied to it with the appropriate magnitude to cancel the external field. For electrons with a kinetic energy E_{kin} in a magnetic field B , the radius of gyration, G is given as

$$R_G [m] = 3.37 \frac{\sqrt{E_{Kin}[eV]}}{B[\mu T]} \quad (3.12)$$

For a coil of wire with n turns, current I, and radius R can be used to produce a counter magnetic field to cancel the external field as given by

$$B = \mu_0 \frac{nI}{2R} \quad (3.13)$$

For the Phoibos 100 this field is then given as

$$B[\mu T] = 0.026 * I[mA] \quad (3.14)$$

The current loop is wrapped around the radius of the hemisphere and primarily is used to cancel out the earth's magnetic field. In order to find the optimal value of the trim coil current the trim coil current is adjusted to maximize the analyzer signal for pass energies of <10 eV. When the external field is reduced in the analyzer to its minimum value the maximum number of electrons will pass through the analyzer.

A final consideration of the analyzer is the difference in work functions between the sample and the detector. They are connected electrically, ensuring that the Fermi levels are aligned. However, the vacuum levels vary at different points along the electron trajectory from the sample to the detector. In order to accurately measure the kinetic energy (E_{kin}) of the electron emitted from the sample the detector work function needs to be calibrated and accounted for. As shown in figure 3.14, the electron kinetic energy at the sample and in the spectrometer (detector) differ by the difference between the sample and spectrometer work functions.:

$$E_{Kin} + WF_{Sample} = E'_{Kin} + WF_{Detector} \quad (3.15)$$

As long as the detector work function is calibrated the emitted electron kinetic energy can be determined. The value for the detector work function is set via the software and can be calibrated using a known sample and following the instructions in the SPECS manual.

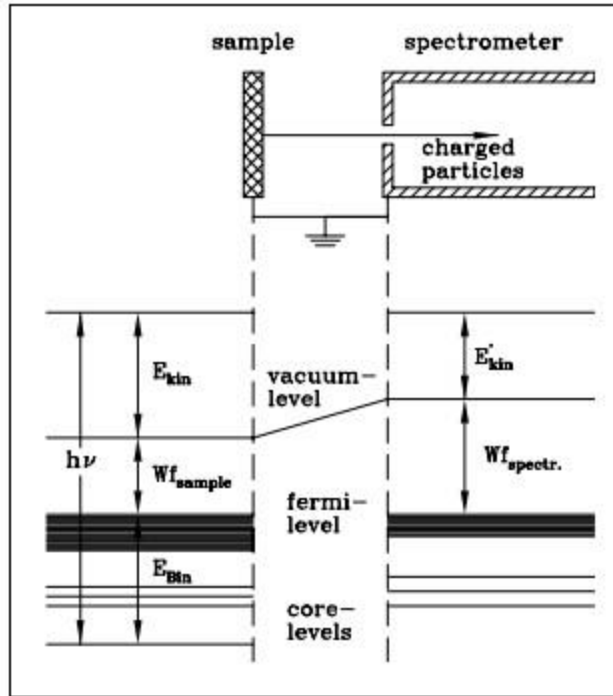


Figure 3.14- Sample and Analyzer relative energy levels [141]

3.3.3 Delay Line Detector (DLD)

After the photoelectrons exit the analyzer they are amplified by the MCP and collected by the detector. The analyzer uses a Delay Line Detector (DLD), which measures the x- and y-coordinates on the detector for each detected electron. The basic principle behind the detector is an overlapping “grid of wires”. The coordinates of an impinging electron are measured by recording the time difference it takes the signal to travel in the horizontal and vertical directions along the wire grid. The detector counting electronics have a 4 MHz collection rate with individual detection sites having a 10-20 ns dead time between signals. Due to the advanced design and precision electronics, the dark count rate of the detector is <100 counts/s over the entire detector leading to very accurate signals over even long periods of time. The detector has a limited lifetime in terms of electron counts. Reaching this lifetime can take years or seconds. The detector count rate should never exceed 4 MHz limitation of the electronics, because excess counts above this limit will only decrease the lifetime of the detector. Specifically, extreme caution is necessary not to turn on the detector when a large number of electrons are present in the chamber such as during e-beam heating or sputtering of the sample. Exceeding the maximum count rate of the detector can lead to inaccurate intensities, or **fatal damage** to the MCP.

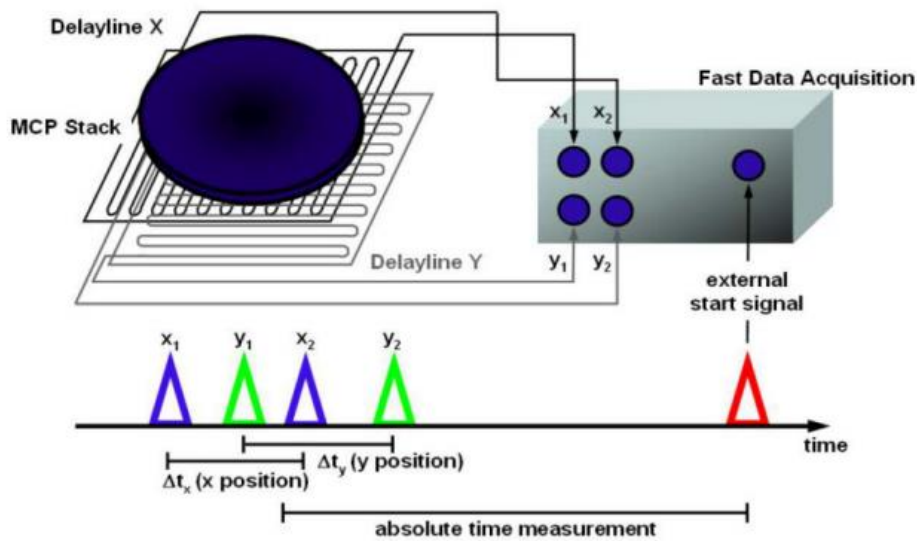


Figure 3.15- DLD schematic diagram. An electron impinges on the MCP, which amplifies the signal and creates current pulses on the delay lines. The current pulses travel to both ends of the "wire" and the time difference of their arrival gives the x and y coordinates of the signal pulse.[142]

In order to accurately acquire data the analog electron pulses traveling the DLD must be converted to the digital form to be readable by the computer. Directly attached to the detector is an Amplifier-Constant-Fraction-Discriminator-Unit (ACU), which is used for amplifying and discriminating the signal from single electron pulses that propagate on the wire detectors of the DLD. The x and y position signals supplied by the DLD need to be converted from an analog signal to digital values. The ACU performs this conversion in real time with no measurable time delay. This digital signal is passed to the Time-to-Digital-Converter (TDC), which serves as a stop watch for the incoming pulses. When data acquisition is started by the computer, the data is sent continuously and is accumulated for a time interval set by the computer using only the USB connection as indicated in figure 3.16. Alternatively a separate external trigger pulse can be used to trigger the data acquisition. The x and y position data as well as the start and stop triggers, if applicable, are then fed to the computer where the SPECS software converts the digital signal to a 2D map of the energy and momentum data from the sample for a specified integration time. Figure 3.16 shows the layout and connections between the DLD and the computer in order to acquire the final signal. The start input, ext start acquisition and acquisition finished ports on the TDC are only used during time resolved measurements and are otherwise disconnected. The rest of the connections are always used for every mode of acquisition. If count rates exceed the 4 MHz count rate of the ACU, or there are multiple hits on the detector within a single laser pulse, then accurate signal

counts cannot be obtained. Having multiple electrons hit the detector means the signal pulses cannot be interpreted by the ACU since it has no way of associating the x and y values with a particular electron. Since signals from crystalline samples have sharp features such as a work function edge and other resonant features, it is likely that local intensities on the detector will exceed the limits of the detection system. This will result in distortion of signals and unnecessary burning of the detector.

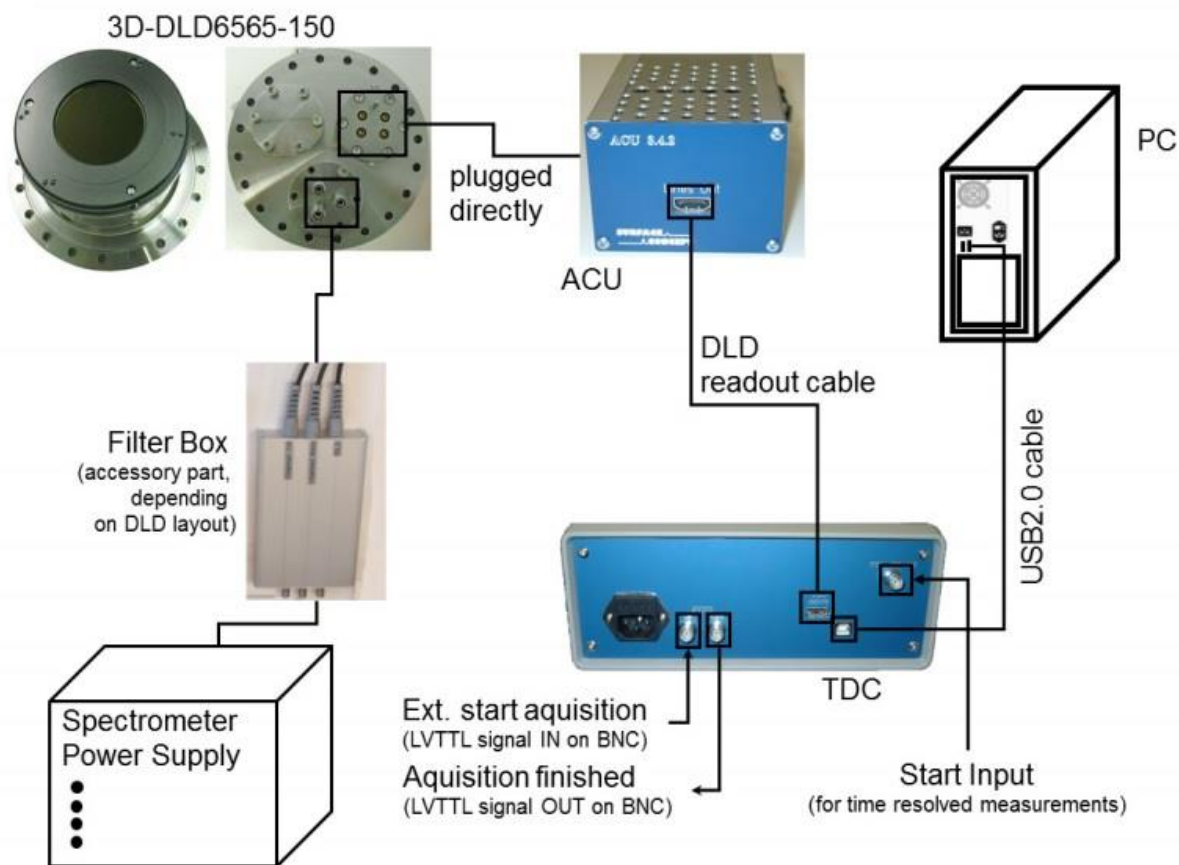


Figure 3.16- Connections between the DLD and the computer which collects the data. The signal is converted to digital by the ACU and then passed on to the TDC to process the pulses and then finally converted to a 2D signal on the computer.[142]

3.3.4 Low Energy Electron Diffraction (LEED)

In order to properly assess the sample quality as well as sample orientation, low energy electron diffraction (LEED) is used. LEED is a standard diagnostic technique for determining surface structure and crystal alignment of crystalline materials. [143]

LEED measurements require sample to have a flat, clean, homogeneous surface over the entire area of the electron beam. Typically the beam is 1 mm in diameter and contains monochromatic electrons. The electrons are backscattered onto a fluorescent screen, forming the diffraction pattern. Inelastically scattered electrons need to be blocked, typically by using various grids at different retarding potentials to deflect the inelastically scattered electrons.

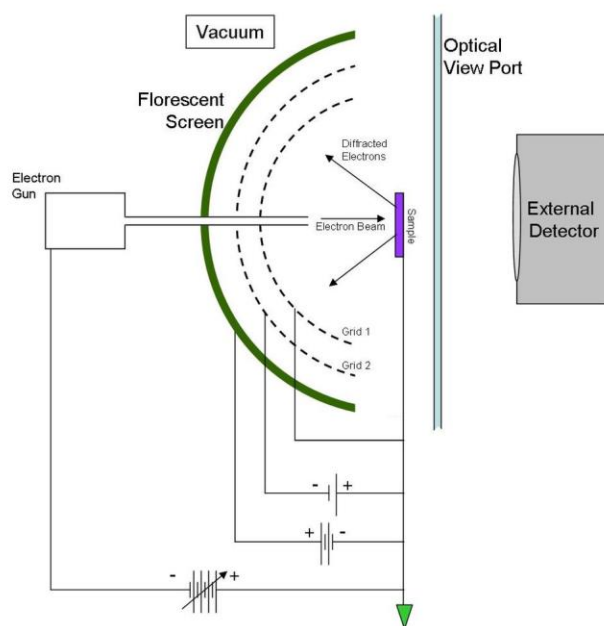


Figure 3.17- Diagram of LEED operation[144]

Figure 3.23 below shows the LEED pattern for a clean rutile TiO_2 surface with the crystalline axes labeled after the sample has been prepared for experiments. For low temperature ($<1,100$ K) preparation, the sample has a 1×1 surface structure; heating above 1100 K produces the 1×2 reconstruction.[145-147] The sample is checked weekly to ensure that the surface remains well-ordered and clean. As the sample ages the LEED pattern intensity and sharpness diminish. When the sharp diffraction cannot be restored even after multiple cleaning cycles, the sample is replaced to ensure consistent results.

3.3.5 UHV Chamber/Pumps

Due to the sensitive nature of the equipment and the high reactivity of the sample surfaces, maintaining a very high level of vacuum is very important for successful photoemission experiments. For instance, the analyzer and detector will only function in a $<10^{-7}$ mbar environment, and a clean TiO_2 sample can only be maintained at $<10^{-9}$ mbar pressures. The better the vacuum conditions, the longer the sample surface can remain uncontaminated. In order to accommodate these conditions, a number of methods are used to keep the vacuum in the $<10^{-10}$ mbar range. At these pressures I can keep the sample in pristine condition and allow the collection of very sensitive data.

The first consideration is the chamber itself. The vacuum chamber is split into two separate parts with a valve separating them. The smaller of these chambers is the load lock chamber. This chamber maintains a pressure of $\sim 10^{-7}$ mbar and is used for loading and unloading samples, as well as transferring them to the measurement chamber. A sample tray holds up to six different samples, which can be kept in this chamber to prevent the surface from degrading over long periods of time. By keeping the samples out of atmosphere the time needed to re-prepare the sample is drastically reduced, making the experiments on multiple samples much more efficient. Additionally this chamber can be opened while maintaining UHV conditions in the main chamber, keeping the vacuum intact. The main chamber is connected by a long thin tube with a shut off valve, which is capable of maintaining the vacuum level even when one side is at atmospheric pressure. Samples can be moved from the load lock chamber into the main chamber via a transfer rod, which can grab, hold, and release the samples. When the valve separating the chambers is opened, the transfer rod can deliver the sample to the sample manipulator in the main chamber. Due to the long and thin construction of the transfer tube, the gas transport between the two chambers is low, allowing for minimal contamination of the main chamber even when the valve is open.

In order to maintain the pressure of the main chamber, a variety of pumping mechanisms are employed. These include a roughing scroll pump, multiple turbomolecular pumps, an ion pump and a cryopump. Each of these will be briefly discussed with information on their operating ranges and method.

The scroll pump reduces the pressure in the chamber and corresponding pipes to $\sim 10^{-2}$ mbar. This level of vacuum is required to allow the other pumps to function correctly. A scroll pump operates by having two “scrolls” (pictured in figure 3.18), essentially Archimedean spirals where one is fixed and the other is rotated around it. This rotation forces a pocket of air through the spiral, trapping it, and eventually venting it out to atmosphere. This rotation continues at high speed, quickly reducing the pressure of the intake side. Scroll pumps have an advantage over older oil based pumps in two main aspects. First they

use no oil, so that there is no danger of oil vapor contaminating the vacuum chamber, and second, they have few moving parts, making them very reliable. The only maintenance they require is to be cleaned and the tip seal to be replaced every other year. The tip seal keeps the two spirals connected as they rotate around each other and over time develops wear and must be replaced. This kit is commercially available and is easy to replace by following the provided instructions. You will notice an increase in base pressure from a low value of 2.0×10^{-2} mbar over time as the seal wears out.

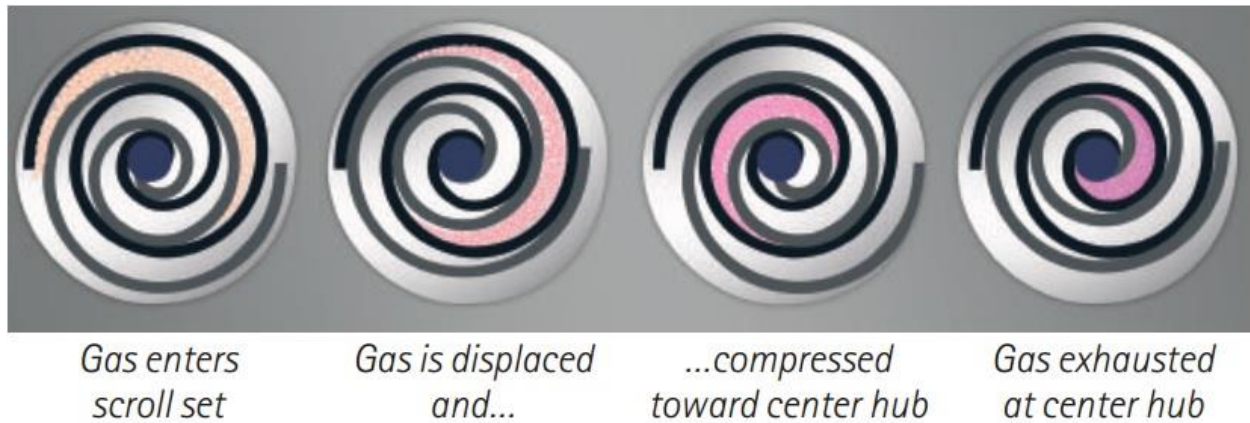


Figure 3.18- Basic operation of a scroll pump[148]

The next set of pumps are turbomolecular pumps. These pumps are the backbone of the vacuum system reducing the pressure from 10^{-2} mbar down to 10^{-9} mbar. In my vacuum system there are three separate pumps; one for the load lock, one for creating a better back pressure behind the main pump, allowing it to operate more efficiently, and one for maintaining the pressure of the main chamber. The principle governing the operation of these pumps relies on a number of different mechanisms. The pumps are made up of alternating rows of high speed rotors and stationary stator blades. Both the rotors and the stationary blades are angled at nearly 45 degrees. As the rotors spin they impart a high kinetic energy to any gas molecules that they hit. Since they are angled down this preferentially pushes the molecules to a lower level. The stationary blades help keep the gas trapped, where it is then caught by the next set of rotors. This process continues, with each compartment for the gas getting smaller and smaller, thus compressing the captured gas until it exits the bottom of the pump where it can be pumped out by the roughing pump. In order for this pump to correctly function it must be in a molecular flow regime. In a laminar flow situation the gas molecules will bounce off each other before reaching the next layer of rotors, causing the pump to stall. Once the mean free path of the molecules is greater than the distance

between the rotor layers this no longer happens, allowing for normal operation. This is one of the main reasons a roughing pump is used to reduce the pressure into the molecular flow regime.

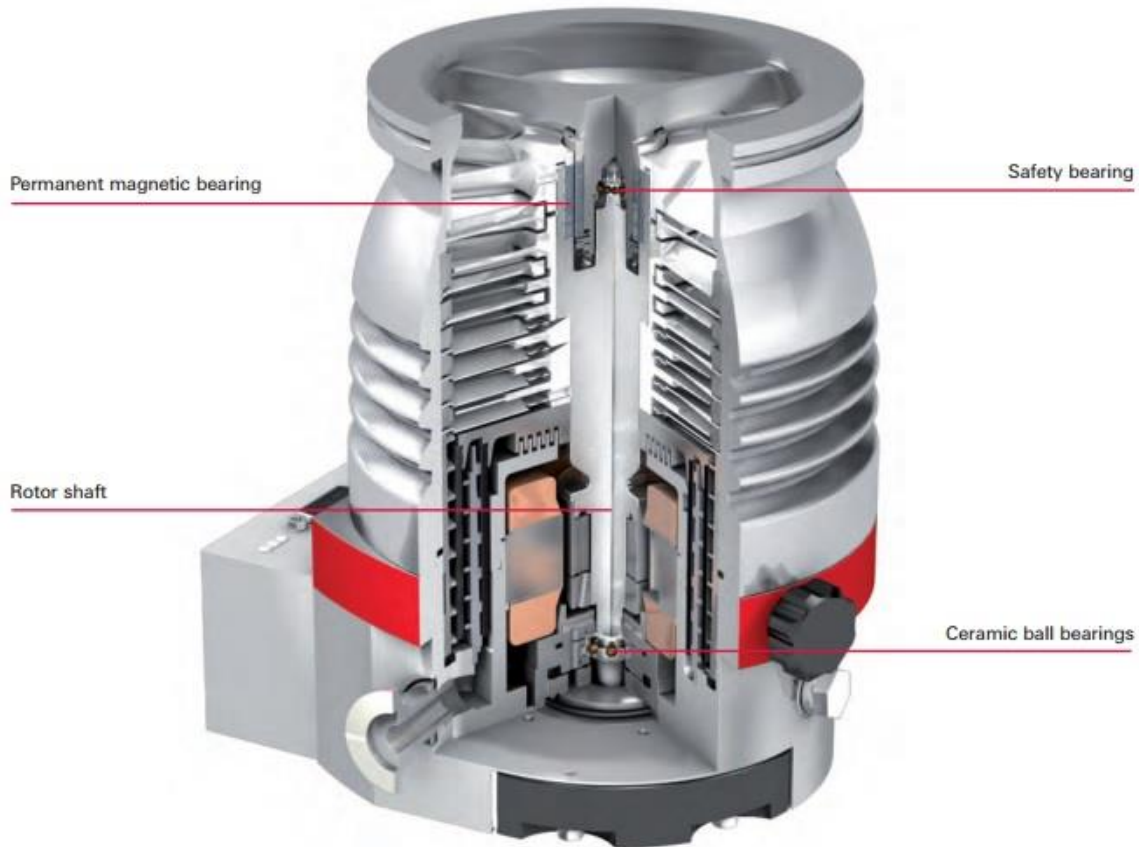


Figure 3.19- Cut away view of one of our smaller turbomolecular pumps[149]

The final pump employed in our chamber is a combination ion and cryo pump. An ion pump allows the chamber to reach pressures down to $1 \cdot 10^{-10}$ mbar, while the cryopump will push that pressure down even further into the 10^{-11} mbar region. An ion pump operates by using a high voltage anode made up of stainless steel tubes, generally kept at a potential of 3000-7000 V. These tubes are placed between a set of titanium cathodes kept at ground. Outside of these cathodes are a set of large ferrite magnets surrounded by a magnetic stainless steel, which keeps the strong magnetic field confined and pointing between the anode and the cathode. This strong field and high voltage traps free electrons in the system, causing them to rotate at high velocities around the positively charged stainless steel anode tubes. When these electrons strike gas molecules they ionize them, whereby the generated positively charged ions are accelerated from the anode and to the cathode. Due to the high voltage, the ion is

accelerated to a very high speed so that when it strikes the cathode titanium is sputtered from the cathode. This does two separate things; first the ion is captured by the cathode and immobilized by chemical reaction on the highly reactive titanium. The titanium atoms that are sputtered off the cathode coat the nearby surfaces, trapping additional atoms and molecules by chemical means. The cryopump is incorporated within the ion pump. Cooling the exposed surfaces of the by ion pump by liquid nitrogen freezes out some of the background gases. This greatly increases the efficiency of the ion pump, causing a rapid drop in pressure down to a minimum pressure of $6 \cdot 10^{-11}$ mbar while the pump is cold. In situations where the sample itself is cooled to low temperatures this additional pumping is unhelpful as the sample surface also adsorbs background gases more easily at low temperatures.

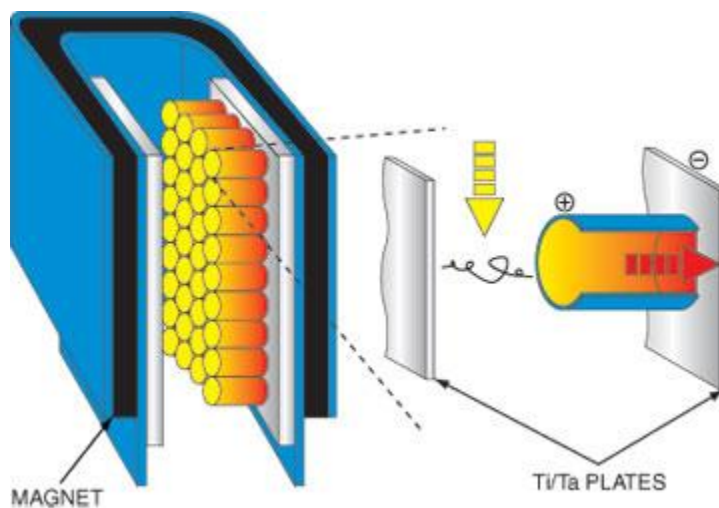


Figure 3.20- Basic schematic of ion pump[150]

3.4 Sample Preparation

The TiO_2 samples used in my experiments are single crystal rutile $\text{TiO}_2(110)$ purchased from Princeton Scientific Corp.; the sample comes in disks of 2 mm thickness and 10 mm diameter. As purchased the crystals start out transparent with a yellowish tint, but as they are reduced in UHV conditions by heating the samples turn light blue. After extensive use the samples become dark blue as they become highly reduced. This reduction of the sample is necessary to obtain a clean surface free of contaminants, and it also improves the sample conductivity.

A single crystal sample affords many benefits over amorphous or powdered samples. An ordered crystalline structure with a well known lattice allows for much easier analysis of the data obtained from the sample. Additionally, photoemission experiments are most easily performed on single crystals, which give a much greater bank of previous research to draw on. Additionally the use of single crystals allows the probing of the band dispersions, as well as the optical anisotropy of TiO_2 . In order to use the samples in the UHV chamber, they must be mounted in a way that allows the laser to excite the surface while still allowing for manipulation of the surface in various ways. The sample is mounted on a molybdenum plate, with a molybdenum cover screwed over it with molybdenum screws (figure 3.21). Molybdenum is used because it is nonmagnetic and has a high melting point. The sample mounting also enhances the thermal contact of sample heating, and allows rotation of the sample without changing the position of the laser focus on the sample.

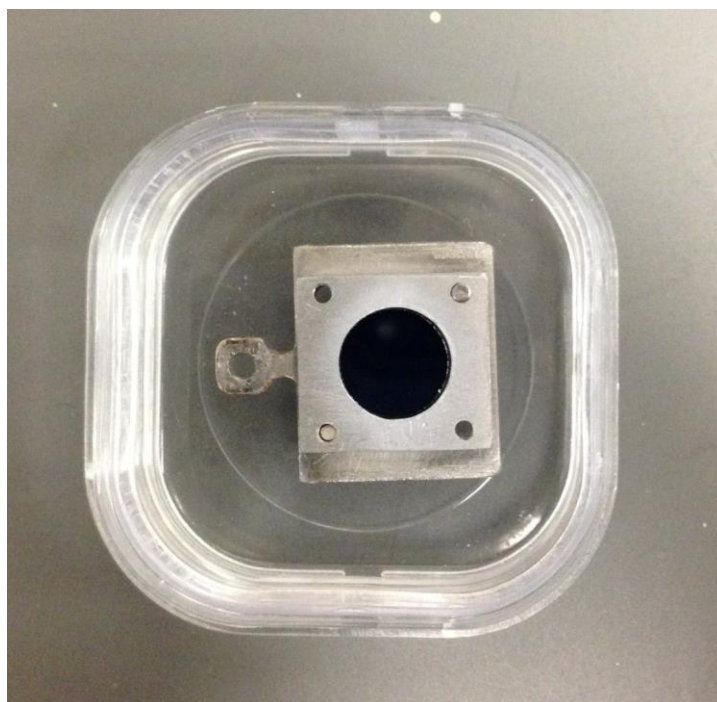


Figure 3.21- TiO_2 sample in a molybdenum sample holder after preparation. The sample has a dark blue color after repeated sputtering and annealing cycles.

The $\text{TiO}_2(110)$ sample surface is very reactive with the background gases present in UHV and must be regularly cleaned in order to obtain a “perfect” surface. When a sample is brought into the chamber from atmosphere, 10-15 cleaning cycles are performed to obtain a flat clean surface. Every 24 hours after that an additional 2 cycles are performed to maintain the surface. A cleaning cycle consists of the

following steps. First, the sample is sputtered using an Ar background pressure of 3×10^{-6} mbar at 2 kV potential for 10 minutes. Next, the sample is annealed in vacuum for 10 minutes at 1000 K. Care must be taken to make sure the sample temperature does not exceed 1000 K for long durations or the surface may reconstruct to the 1×2 structure.[145-147] This is repeated until the final cycle where the sample is then annealed in a 1×10^{-8} mbar oxygen atmosphere provided by backfilling the UHV chamber to heal some oxygen vacancies that are created by sputtering and annealing.[36,84] This step can be bypassed if a more reduced surface is desired.

As TiO_2 is an anisotropic material there are two distinct crystalline directions on the exposed surface. These are labeled by their Miller indices, the $[001]$ and $[\bar{1}\bar{1}0]$ directions. Aligning the crystal along these directions is important because the electrical and optical properties in the surface plane are anisotropic. The sample orientation is determined and oriented by LEED [151], as required for experiments. The sample quality is ascertained from the LEED pattern analysis, and two photon photoemission (2PP) work function edge. A perfect surface exhibits a work function of ~ 5.4 eV while a reduced surface with many oxygen vacancies has a work function of ~ 5.0 eV and increased photoemission intensity.[17,36] Figure 3.22 shows 2PP spectra of a clean TiO_2 surface excited with 400 nm (3.1 eV) light for various preparation methods, while Figure 3.23 shows the LEED pattern of a clean surface.

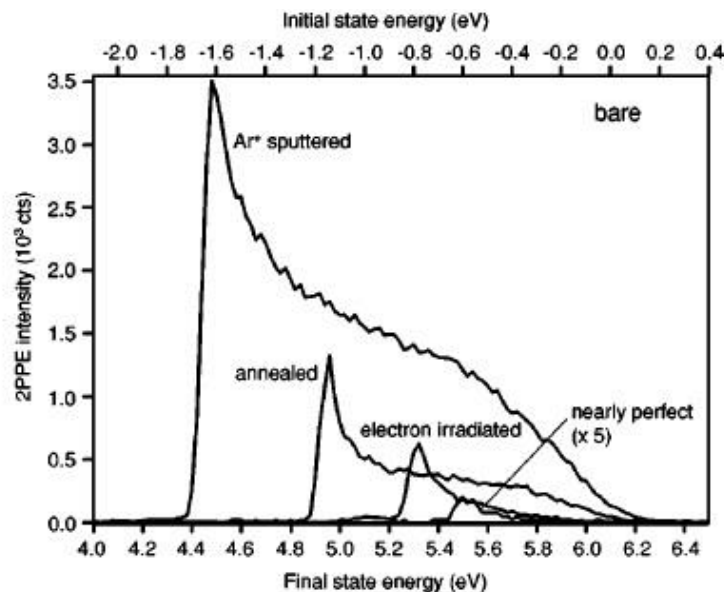


Figure 3.22- TiO_2 sample work function under various surface preparation methods, showing the change in work function and photoemission intensity with the method of preparation [36]

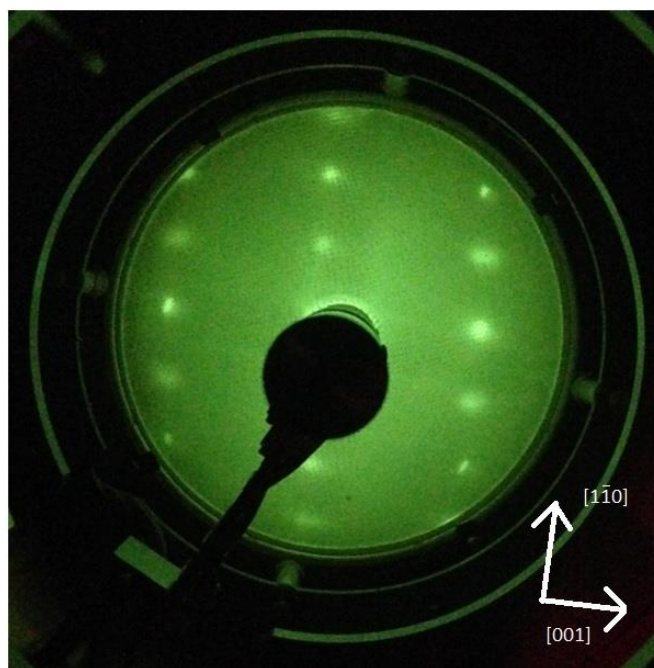


Figure 3.23- LEED pattern for a clean $\text{TiO}_2(110)$ 1×1 surface. The presence of a visible pattern of diffraction spots indicates a clean surface with minimal contamination from surface adsorbents.

Over a span of several hours, the TiO_2 sample becomes contaminated from background gases in the UHV. Typical contaminants are OH and H_2O on the surface, which will be discussed in greater detail in the experimental sections. The contamination decreases the work function, down to ~ 4.8 eV over the period of ~ 12 -24 hours. The time it takes for contamination to accrue is directly related to the vacuum pressure of the chamber. The TiO_2 sample is highly reactive, with a large sticking coefficient for many gasses. For a material with a sticking coefficient of 1, every atom that hits the surface will adsorb. The exposure to surface adsorbates is measured in Langmuirs ($1\text{L} = 10^{-6}$ torr*s), which is roughly equivalent to one monolayer of coverage for 1 L for highly reactive gases such as H_2O on TiO_2 [71,72]. Therefore at a pressure of 10^{-9} torr, it would only take ~ 1000 s for the sample to be completely covered by adsorbates. By reducing the chamber pressure to $\sim 10^{-11}$ torr, I can maintain a clean sample surface for much longer periods of time. Even with a very low chamber pressure, and good cleaning techniques the sample quality will degrade during measurement as adsorbates continue to deposit on the surface. This must be accounted for during measurement. At high temperatures the sample is always very clean as most adsorbents desorb above 400K. At room temperature the sample degrades over 3-4 hours of measurement, but generally reaches an equilibrium point after which the work function decrease will stop. At low temperature the sample will quickly degrade, generally being covered in adsorbents by the

time the sample is cooled. This can be reversed by flash heating the sample while keeping the rest of the manipulator cold. As the sample rapidly heats the adsorbed molecules desorb from the sample and quickly adsorb onto the still cold manipulator. This improves the vacuum level further and prevents the sample from becoming contaminated when it is recooled. Once the sample is clean and cold the surface will remain so for an additional 3-4 hours.

3.5 Sample Dosing

My experiment requires various gasses to be introduced into the UHV chamber in the process of sample preparation. Ar gas background pressure must be introduced for sputtering, and an oxygen background pressure must be provided for annealing of the sample to reduce O atom vacancy defects. After the clean TiO₂ surface has been prepared, it can be modified by adsorption of various gasses such as CO₂, methanol, water, etc. In order to facilitate the controlled introduction of gases, homemade dosers were constructed from thin stainless steel piping for the delivery of gases, translation stages for approaching the doser to the sample, and high sensitivity leak valves for controlling the gas flow. The leak valves are mounted to the translation stages and welded to the thin steel piping. The long pipe length ensures the gas that comes out of the doser is emitted directly onto the sample so as to minimize the contamination of the UHV chamber. The translation stages allow us to control the distance from the sample so that I can dose directly from a few centimeters from the sample and then retract the doser for measurements.

An important part of the dosing procedure is knowing how much gas is being introduced onto the sample. Since the partial pressure coming out of the doser is much higher than the background pressure in the chamber, one must calculate the actual exposure rate of the surface to the gas. The pumping speed of the ion pump for a given background pressure is known, and it can be assumed that the gas exits the doser effusively as an expanding sphere of gas. Using this information, combined with the distance of the sample from the doser one can calculate the exposure to the gas that is received by the sample. Typical dosing values used for the TiO₂ experiments are from ~0.1 to 5 L. Specific dosing values and procedures will be discussed in their corresponding experimental sections.

Due to the sensitivity of the TiO₂ surface, the presence of dosing gases in the chamber must be monitored over time. After repeated dosing the chamber pressure will begin to deteriorate, preventing the sample surface from staying clean during experiments. Typically after dosing molecules onto the surface more than a dozen times, the chamber must be baked to remove the retained molecules in the chamber. This is especially true for H₂O, which is exceptionally difficult to evacuate from the chamber.

Even small doses of H₂O can compromise the UHV conditions. In order to ensure the highest quality data and sample quality, the chamber is baked out when the base pressure of the system rises above 2×10^{-10} mbar. This also ensures a constant dosing rate since a higher background pressure means a lower dosing pressure for the same leak valve position.

The temperature of the sample also plays a large role in the dosing process. At lower temperatures more molecules are capable of adsorbing onto the surface, meaning higher coverage is possible. At higher temperatures many molecules dissociate on the surface, leading to different coverage and conditions. These specific examples will be discussed in the experimental section that follows. At a given temperature there is a maximum coverage that is achievable, and dosing beyond that amount will lead to little or no change on the surface. This is important in maintaining the quality of the vacuum by not overdosing the sample.

3.6 Quadrupole Mass Spectrometer

In order to assess the purity of the vacuum, the quality of the gases I am dosing onto the sample, and to detect leaks an Extrel (Max-LT 500 MS) quadrupole mass spectrometer is used. The mass spectrometer allows continuous scanning over a broad range of molecular masses and provides real time data on the partial pressure of the gases present in the chamber. Due to its high sensitivity, the mass spectrometer can be used to observe which gases desorb from the sample surface, which gases are being introduced into the chamber, or which background gases make up the chamber pressure. Additionally it can be used to leak check the system using helium, being capable of detecting a leak even at 5×10^{-10} mbar. This has proved invaluable to decreasing the chamber pressure and providing the best UHV conditions possible for the highly reactive TiO₂ surface. Due to having a heated filament for electron bombardment generation of ions, the mass spectrometer should be allowed to equilibrate for at least 4 hours, allowing enough time for the mass spectrometer temperature to desorb any residual gases on the walls of the chamber or on the mass spectrometer itself. Once this is done an accurate measurement of the residual gases in the chamber can be measured as shown in figure 3.24 below. As you can see when the chamber is leak free and adequately baked there is almost no detectable gas in the chamber, allowing a clean surface to be obtained and maintained over long periods of time. The primary gas leftover after degassing is mass 28 (CO). The CO diffuses through the chamber walls out of the steel and slowly decreases over long times (years). This peak is very small and only noticeable at the most sensitive settings of the mass spectrometer. The presence of a mass 28 peak could also signal the presence of

nitrogen due to a leak, but this will always be accompanied by an additional peak of mass 32 for oxygen. However, if the chamber pressure is below 10^{-9} mbar the primary source of mass 28 is almost always CO. Due to the distance of the QMS from the sample measurement position it can be run during measurements, contributing only a small increase in background signal to the detector.

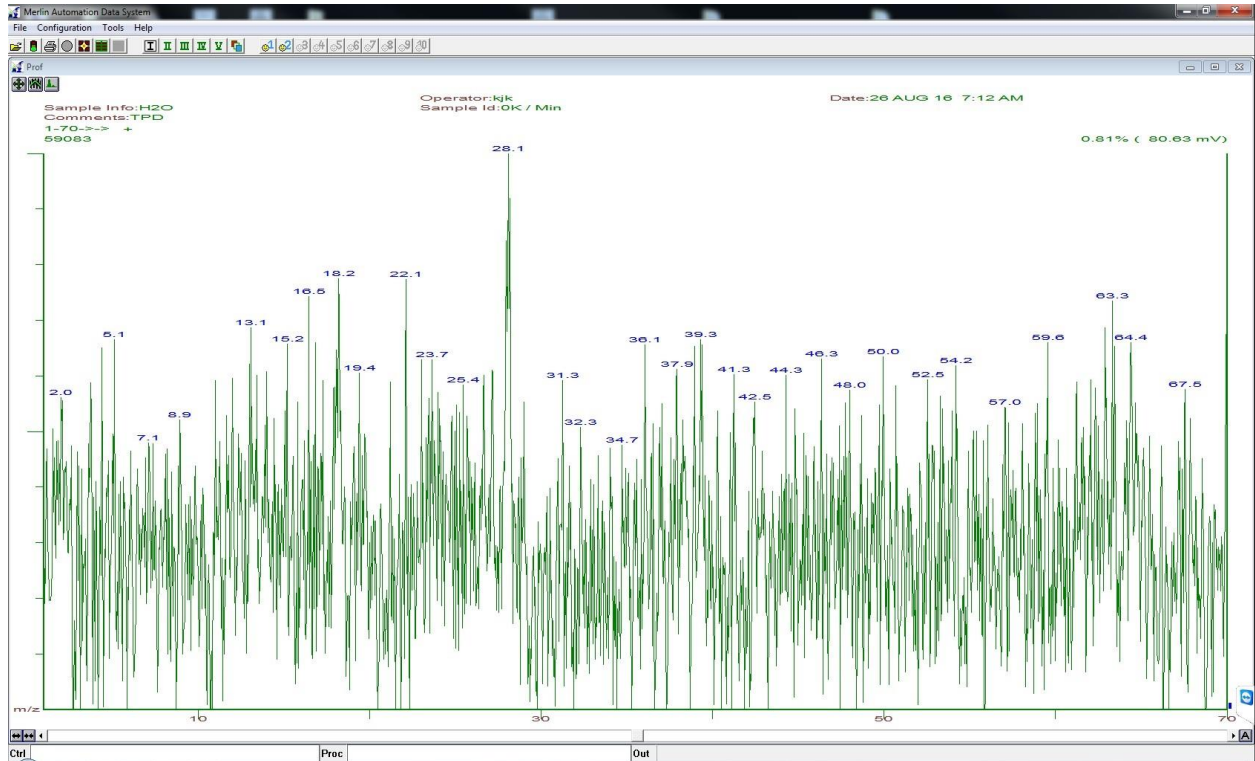


Figure 3.24 - Mass spectrometer readout for a clean chamber. Even the high sensitivity of the mass spec should have a very low signal when the chamber is well baked and leak free. At the standard operating pressure noise dominates the spectrum with only a slight peak at mass 28, corresponding to CO.

4. Chapter Four: Resonant d-d-band Transitions in TiO₂(110) via Multi-Photon Photoemission

4.1 Introduction and Motivation

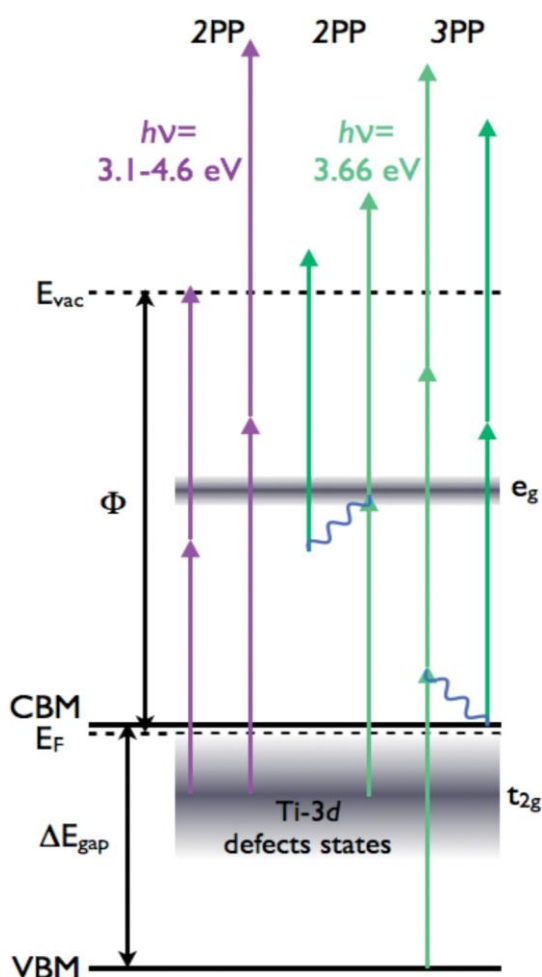


Figure 4.1-mPP excitation diagram for the clean, reduced rutile TiO₂(110) surface. With $h\nu = 2.9\text{--}4.6$ eV (purple arrows), 2PP processes are excited from the Ti-3d defect states. Resonant 2PP excitation from the t_{2g} symmetry defect states to the nearly degenerate e_g bands occurs with $h\nu = 3.66$ eV. Under high-density excitation there is concomitant 3PP excitation from the VBM. These processes can be coherent (light green) or sequential (dark green), where hot electron relaxation (squiggly blue lines) can occur within the CB. Black arrows designate the work function ϕ and the band gap, ΔE_{gap} .

The photocatalytic and photovoltaic activity of a semiconductor depends on the carrier excitation and relaxation processes in the near-surface region [152,153]. The photoexcited electron dynamics in TiO₂, primarily for colloidal rutile and anatase polymorph samples, have been studied by optical methods over a broad frequency range from the THz to ultraviolet (UV) spectral regions [154-164]. In optical experiments UV light excites carriers across the band gap and various color light absorption or emission processes report on the ultrafast carrier energy and momentum evolution. It is difficult, however, to assign spectral features to the specific carrier type and its chemical potential, within a temporally and spatially evolving carrier distribution based on all optical measurements. Such information is essential for establishing the potential of photoexcited carriers to catalyze chemical reactions, or to drive current within photoelectrochemical cells.

Time-resolved multiphoton photoemission (TR-mPP) spectroscopy has significant advantage in being able to probe the time-dependent electron populations at specific energy and momentum in the near-surface region of a solid [105,110]. TR-2PP has been applied to the spectroscopy and dynamics of single-crystal rutile TiO₂(110) surfaces under ultrahigh vacuum (UHV) conditions in the contexts of both photocatalysis and dye-sensitized solar cells [36,70-72,81,165-169]. Selected excitation pathways for 2PP and

3PP excitation in TiO₂ with UV light of relevance to my studies is illustrated by the energy diagram in figure 4.1,

In previous studies, interferometric pump-probe TR-2PP measurements with ~1 nJ, 10 fs, 3.1 eV laser pulses were used to probe the electron dynamics upon excitation of the Ti-3d defect band [71]. These measurements could not resolve the hot electron lifetimes in the 1.5–3.1 eV energy range above E_F either because the lifetimes were too short, or the intermediate states in the 2PP process were virtual. The latter possibility was consistent with an apparent lack of distinct spectroscopic features in the 2PP spectra due to unoccupied intermediate surface or bulk states of TiO₂ [36,71]. The experimental results were also consistent with theoretical predictions of fast hot electron relaxation in TiO₂ by electron-electron (e-e) and electron-phonon (e-p) scattering [170,171]. Because of the fixed excitation wavelength, TR-2PP measurements on TiO₂ could not address the properties of the photocatalytically relevant CBM carriers as has been done for ZnO [172,173].

Other TR-2PP measurements by Matsumoto, and Willig and coworkers addressed the charge injection from chemisorbed dye molecules into the conduction-band (CB) of single-crystal rutile TiO₂(110) surfaces [81,167-169]. The charge injection rates were found to depend on the functional group anchoring the dye molecules to the TiO₂ surface. In the case of the TR-2PP measurements on a catechol-covered TiO₂ surface, the time scale for the primary injection into the semiconductor was judged to be instantaneous, whereas the subsequent population decay occurred in a biexponential manner with ~100 fs and ~1 ps components, without significant energy relaxation [168]. The decay was thus attributed to charge transport from the TiO₂ surface into the bulk. Such long hot electron lifetimes were difficult to reconcile with the substantially faster dynamics at comparable energies on clean and protic molecule-covered TiO₂ surfaces [70,71,174] as well as the more recent measurements of hot electron relaxation in the CB of ZnO [172,173].

In this chapter I report on the electronic structure and femtosecond time scale photoexcitation dynamics within the CB of TiO₂ by TR-mPP spectroscopy using tunable UV femtosecond laser excitation to excite the 2PP and 3PP processes. A thorough understanding of the surface and bulk excitation and relaxation pathways is necessary for the interpretation of mPP spectra and electron dynamics of molecule-covered TiO₂ surfaces. Using a wavelength tunable femtosecond laser excitation source, I extend the spectroscopy and dynamics at rutile TiO₂(110) surface to a broad energy range below and above band-gap excitation. Excitation wavelength, polarization, and crystal azimuthal orientation dependent measurements reveal a pair of nearly degenerate unoccupied states located at 2.73 ± 0.05

and 2.85 ± 0.05 eV above the E_F , which resonantly enhance the 2PP process at ~ 3.66 eV from the occupied Ti-3d defect states. Based on the calculated electronic structure of rutile TiO_2 and other spectroscopic evidence, I assign this resonance to the e_g component of the crystal-field split Ti-3d conduction band. TR-2PP measurements reveal unusual photoexcitation dynamics associated with saturation of the 2PP process via the resonant t_{2g} - e_g transition, which occurs simultaneously and in competition with the 3PP process from the valance-band maximum (VBM). The dynamics of such intra-d-band excitations are of significant interest for their potential impact on photocatalysis and because in correlated metal oxide materials they can optically trigger electronic and structural phase transitions [175-177]. The new information expands our understanding of the spectroscopy and electron dynamics of TiO_2 and related metal oxides under high excitation density, nonlinear conditions.

4.2 Experimental Details

Previous 2PP studies of a $\text{TiO}_2(110)$ surface with 3.1 eV excitation showed broad, featureless spectra,

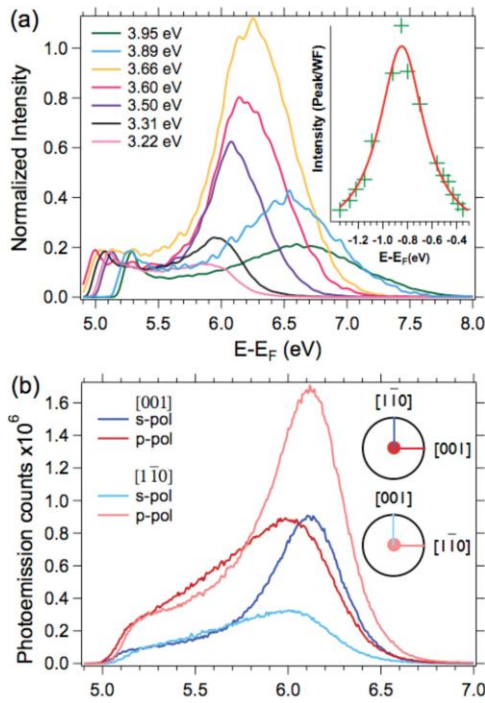


Figure 4.2- (a) Excitation-dependent 2PP spectra of the clean $\text{TiO}_2(110)$ surface showing the emergence of a peak for $h\nu \geq 3.2$ eV (380 nm). The spectra are normalized to the work function edge. Inset: Distribution of the peak 2PP intensity relative to the work function intensity, which is attributed to the defect density of states below the Fermi level. (b) 2PP spectra excited with p - and s -polarized light for 3.26 eV photon energy with the [001] or [110]

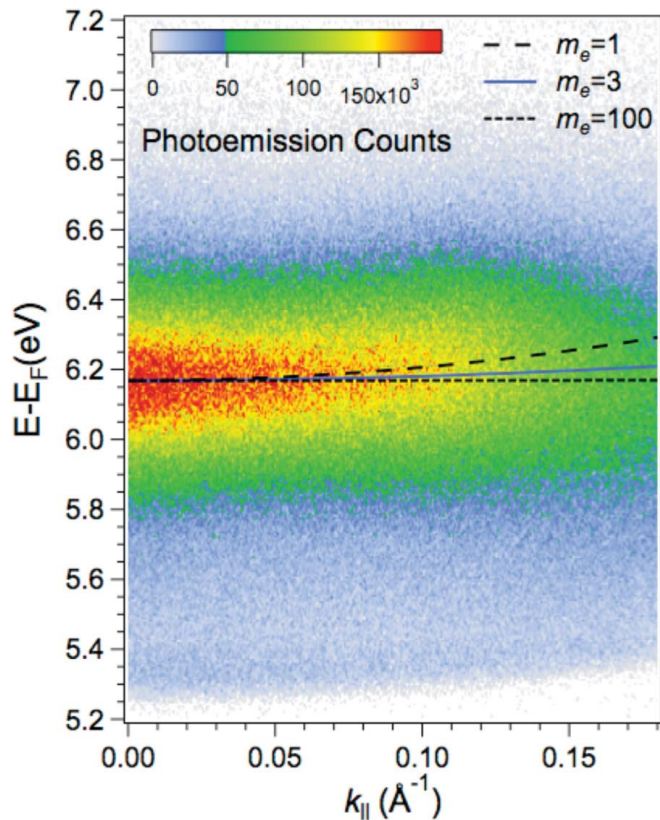


Figure 4.3- Energy vs. momentum plot of 2PP intensity with 3.60 eV excitation showing the weak dispersion of the e_g state. Due to a limited momentum range of the measurement and the broad width of the resonance the effective mass of $m_e = 3$ has a high uncertainty bracketed by the dashed lines for $m_e = 1$ and 100.

with photoelectron count rate and work function onset that depended on the surface preparation protocols[36]. Reducing the surface populated the Ti-3d defect states. Consequently, the 2PP spectra had low work functions and high count rates from the Ti-3d defect states. By contrast, nearly stoichiometric surfaces had high work functions and small count rates [36].

The high pulse energy and tunability of the NOPA system, compared with the previously used Ti:sapphire laser, allow us to probe the TiO₂(110) surface with higher sensitivity and greater discrimination of the optical excitation pathways. The energy diagram in figure 4.1 shows the possible excitation pathways available for the range of photon energies used in our experiments as well as the electron relaxation pathways. As in the previous experiments, the primary excitation is from the Ti-3d defect band [36]. The Fermi level of reduced TiO₂ is typically reported to be 0.1 – 0.3 eV below the CBM [178]. Because I cannot determine this quantity, in the following discussion I assume a value of 0.2 eV for the CBM–E_F energy difference. The indirect optical band gap of TiO₂ rutile of 3.0 eV [17] is within the employed photoexcitation energy range, but the band-gap excitation does not contribute to the 2PP signal unless the two-photon energy is sufficient to excite electrons from the VBM to above the vacuum level, E_{vac}, as already explained. The band-gap excitation can contribute to a 3PP process, however, if the first photon excites across the band gap and subsequent two photons excite CB electrons to above the E_{vac}. Rutile TiO₂ becomes strongly absorbing at the onset of the direct band gap at 3.6 eV, with the absorption maximum occurring at 4.0 eV [17,179].

The 2PP spectra of a clean TiO₂(110) surface excited with p-polarized light in the 315–385 nm (3.22–3.95 eV) range are shown in figure 4.2(a). With 3.22 eV NOPA excitation, the 2PP spectra resemble the previously reported ones with 3.10 eV excitation by the second harmonic of a Ti:sapphire oscillator [36,71]. Tuning the excitation to higher photon energies, however, reveals a new feature. As the photon energy is increased from 3.22 eV, there is rising 2PP intensity at the E_F edge (the high-energy edge of the spectra), which emerges into a clear resonance for 3.66 eV excitation. An angle-resolved spectrum measured with 3.66 eV excitation in figure 4.3 shows weak band dispersion corresponding to an effective mass of >3m_e (m_e is the free-electron mass). This mass is shown in the e_g state of figure 4.3, however it can also be affected by the initial t_{2g} state, because the spectrum shows the resonance between them. This is the lower bound on the electron mass because of the weak dispersion, narrow momentum measurement range, and broad resonance width.

To gain further information on the newly found resonance, I also measure 2PP spectra for a series of photon energies with both s- and p-polarized light and the TiO₂ crystal oriented with either its [001] or

$[1\bar{1}0]$ crystalline axis in the optical plane. The 2PP spectra depend on the crystal orientation because of the anisotropy of the rutile crystal, and consequently its band structure [17].

Typical 2PP spectra of the anisotropic response with 3.26 eV excitation are shown in figure 4.2(b). The resonance peak appears in 2PP spectra excited with both polarizations and crystal orientations, but its line shape varies and peak energy shifts. The background emission near the work function edge is much weaker for s-polarization, as observed previously [71].

As expected, the anisotropy of the rutile TiO_2 results in strong dependence of 2PP spectra on the azimuthal orientation of the sample and the light polarization with respect to the optical plane. The resonance can have either a sharp and intense, or a broad and weak character depending on the direction of the excitation field \vec{E} with respect to the crystalline axis. The sharp/intense character is observed when a component of \vec{E} points in the $[1\bar{1}0]$ direction, whereas the broad/weak character occurs when a component of \vec{E} points along the $[001]$ direction. Moreover, the resonance shifts from 2.85 to 2.73 eV between the two characteristic spectra.

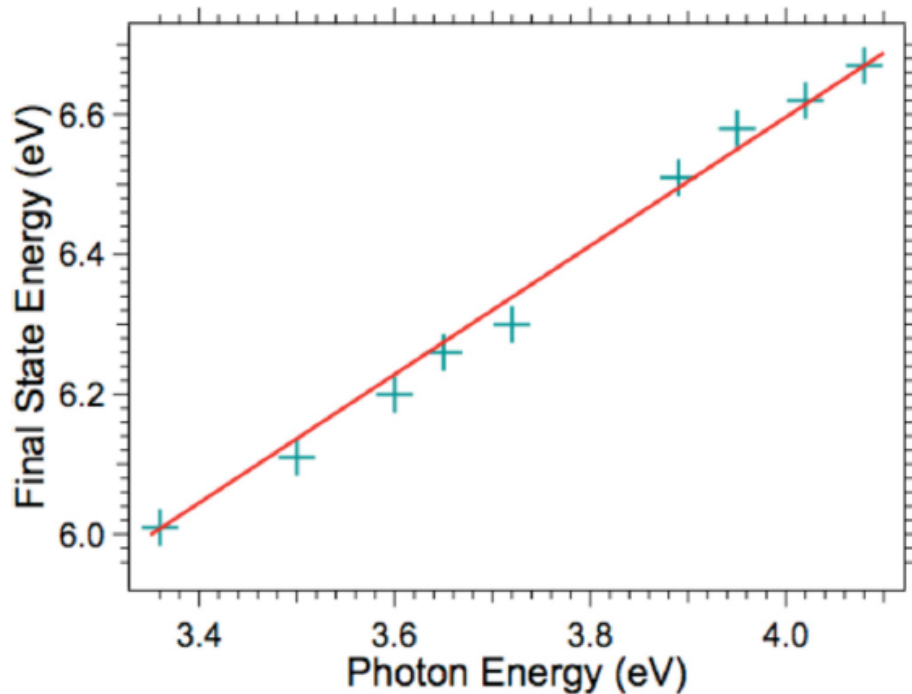


Figure 4.4- Final state energy vs. photon energy for the e_g peak. The slope of ~ 1 confirms the e_g band to be an intermediate state in the 2PP process.

Measurements of 2PP intensity maximum vs. the excitation photon energy for p-polarized \vec{E} and the crystal oriented with the [001] axis in the optical plane (figure 4.4) reveal the new resonance to be due to an unoccupied state 2.8 eV above E_F , which serves as a resonant intermediate in the 2PP process from the occupied Ti-3d defect states. The inset in figure 4.2(a) shows the intensity of the observed peak relative to the intensity of the work function edge for the various excitation wavelengths. The 2PP intensity maximum of the resonance peak occurs for 3.66 eV excitation. This analysis locates the maximum of the initial defect state density at 0.85 eV below E_F [inset of figure 4.2(a)], which is consistent with the defect state density maximum found in conventional photoemission spectra [6,180]. The magnitude of the resonance enhancement for excitation from the defect states depends on the defect density, but its energy distribution remains constant.

4.3 Theoretical Discussion and Assignment

Because the 2.8 eV state has not been reported in the previous optical or 2PP experiments on TiO_2 , I consider its assignment. The only resonances observed in 2PP measurements on TiO_2 have been with the extrinsic wet electron states on H_2O and CH_3OH -covered $\text{TiO}_2(110)$ surfaces [71,72,165,181]. Although at 1 ML coverage of H_2O or CH_3OH the wet electron states are at 2.3–2.4 eV above E_F , at lower coverages they have been reported to shift to higher energy, because fewer solvating OH or CH bonds are available for their stabilization [71]. The assignment of the observed resonance to the wet electron states produced by molecular chemisorption from the residual gas in a UHV chamber can be excluded, however, because that requires time, whereas the 2.8 eV resonance exists immediately after the sample annealing at 600 K. Surface OH formed by dissociation of H_2O can be excluded as a potential carrier of the spectrum, because it desorbs at 490 K, whereas the resonance is present in 2PP spectra at 600 K just as at 293 and 100 K [56].

Because the CB of TiO_2 is derived from the Ti-3d states, the most obvious assignment of the 2.8 eV resonance is to t_{2g} - e_g transitions between the crystal-field split 3d conduction bands. To see that this is reasonable, one does not need to look any further than a Ti:sapphire laser, which derives its lasing properties from the t_{2g} - e_g absorption (and consequently, stimulated emission) of Ti^{3+} ions within the crystal field of Al_2O_3 ; the absorption peak for this transition is at 500 nm (2.48 eV) [78]. Moreover this assignment is consistent with the band structure calculations of TiO_2 . [17]

The assignment to the t_{2g} - e_g transition is further corroborated by other experimental evidence. Weak optical d-d transitions have also been reported at 2.30 and 2.92 eV in reduced rutile samples [182]. In x-

ray absorption (XAS), x-ray photoemission (XPS), inverse photoemission (IPS), and electron-energy loss spectroscopy (EELS) measurements features corresponding to the t_{2g} - e_g band splitting in a range of 2.1–3.0 eV have been reported [22,24,183,184]. Thus, our measured peak at 2.8 eV above E_F and its assignment to the e_g band are fully consistent with the DFT calculations and other spectroscopic evidence.

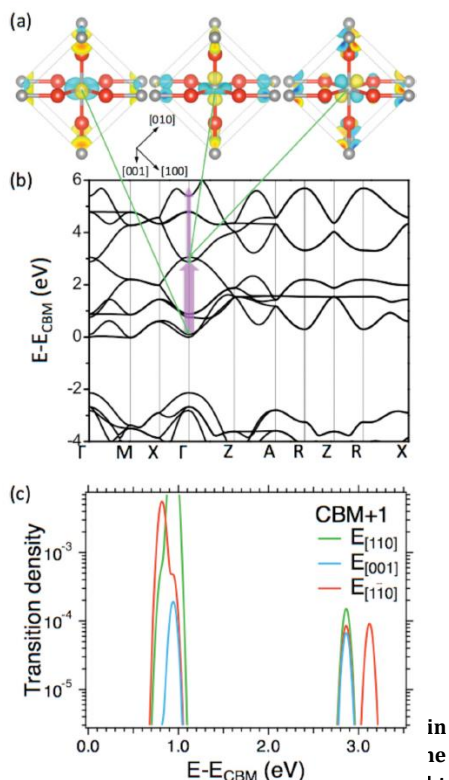
The assignment of the 2.8 eV resonance to t_{2g} - e_g transitions is supported by the recent many-body perturbation theory calculations of TiO_2 band structure [17,185,186]. To confirm, Zhao and coworkers calculated the t_{2g} - e_g optical transition density within the DFT. The calculation at this level of theory is sufficient for determining the transition energies because errors in calculating the quasiparticle band gap within DFT cancel when considering transitions between the unoccupied bands [17,187].

Zhao and coworkers performed the calculations with the SIESTA code [188] using the generalized gradient approximation for the exchange correlation density functional (PBE) [189]. With a double-zeta polarized (DZP) numerical basis set a good agreement is reached with results obtained with a plane-wave basis. The geometries are fully relaxed until the force on each atom is less than 0.04 eV/Å. The lattice constants used are $a = 4.59$ and $c = 2.95$ Å. The rutile TiO_2 bulk is calculated using (1×1) unit cell and a Monkhorst-Pack grid of $(6 \times 6 \times 9)$ k points. The transition dipole moment is defined as

$$T_{n',n}^i(k) = \langle \psi_{n',k} | \vec{r}_i \cdot \vec{E} | \psi_{n,k} \rangle \quad (4.1)$$

and the transition density is calculated from $T_{n',n}^{i*}(k)T_{n',n}^i(k)$ at the Γ point. To obtain the transition density, the CB is occupied with one excess electron. Furthermore, I consider transitions from both the CBM and CBM+1 bands, which are separated by only 0.12 eV at the Γ point and have predominantly $d_{xy} + d_{xz}$ and d_{xy} orbital character. Figure 4.5 and Supplemental Material, of reference [190] show the calculated spatial distributions of orbitals involved in the optical transitions at ~ 3 eV from the CBM, the band structure of rutile TiO_2 , and the calculated transition densities. The calculations predict that two transitions to e_g bands with the d_{z^2} and $d_{xz} + d_{yz}$ orbital character at 2.87 and 3.12 eV can contribute to the 2PP spectra.

The measured azimuthal orientation and polarization dependent 2PP spectra in Fig. 4.2(b) are consistent with the calculated transition densities in Fig. 4.5(c) in that \vec{E} pointing in the $[1\bar{1}0]$ direction corresponds to the highest transition density and shift of the resonance to higher energy, as compared to when \vec{E}



the orbitals correspond to the CBM+1, 2.85, and 3.11 eV bands. (b) The band structure of TiO₂ rutile from DFT calculations. The fat arrow indicates the t_{2g} - e_g resonance at the Γ point. The thin arrow represents photoemission from the transiently excited e_g state. (c) The calculated transition density for d - d transitions from the CBM+1 excited by for E pointing in the [001], [110], and [110] directions. The energy origin is the CBM.

points in the [001] direction. If the initial state has the symmetry of CBM, when \vec{E} points in the $[1\bar{1}0]$ direction the transition density is much smaller than when it points in the [001] direction, in contradiction with the experiment (Supplemental Material, of reference [190]). Although the observed behavior is consistent with transitions from defect states of the CBM+1 symmetry, it does not exclude some contribution from states with the CBM symmetry. This assignment is consistent with an isotropic component along the $[1\bar{1}0]$ direction that is present in all measurements along with an additional anisotropic component oriented along the [001] direction.

Despite firm grounding of this assignment in experiment and theory, two groups challenged it and attributed the resonance to different origins. Wang et al. reported similar 2PP spectra of reduced TiO₂ surfaces, claiming the assignment to a single d - d transition of OH terminated TiO₂ at a lower energy than in our original report (Wang, Z.; Wen, B.; Hao, Q.; Liu, L.-M.; Zhou, C.; Mao, X.; Lang, X.; Yin, W.-J.; Dai, D.; Selloni, A.; Yang, X., *J. Am. Chem. Soc.* **2015**, *137*, 9146-9152.).[191] In another study, Zhang et al. attributed the resonance to wet electron states of low density surface OH, rather than the bulk d - d transitions and additionally claimed that coherent and sequential excitation

pathways involving a single intermediate state were the cause of the differing peaks (Zhang, Y.; Payne, D. T.; Pang, C. L.; Fielding, H. H.; Thornton, G., *J. Phys. Chem. Lett.* **2015**, 3391-3395.).[192] Both groups also made bold claims that this UV resonance of reduced TiO₂ could confer photocatalytic activity in the visible region below the fundamental band gap at 3.0 eV. In order to confirm the initial assessment additional experiments were performed to discount these alternative assignments.

Whether or not wet electron states are the carrier of the resonant 2PP spectra can be answered by performing additional temperature dependent measurements. It is well established that surface OH desorbs at ~ 490 K,[73] and therefore, how the 2PP spectra change with temperature through the range that spans the desorption temperature should be a rigorous diagnostic for whether or not the surface

OH is their carrier. Figure 4.6 shows 2PP spectra of a freshly prepared TiO₂ surface as the sample is cooled from 600 to 300 K. The spectra show a distinct resonance, which appears within a final state range between 6.1-6.3 eV, and narrows and shifts to lower energy as the sample cools. The resonance is observed at 600 K, i.e., well above the OH desorption temperature, and it changes continuously as the sample is cooled to below 490 K, where the surface OH, if it had any role in the observed spectra, would be stable. The continuous change of the spectra shows that the observed resonance is due to a species that exists under conditions where surface OH would be unstable with respect to desorption from TiO₂.

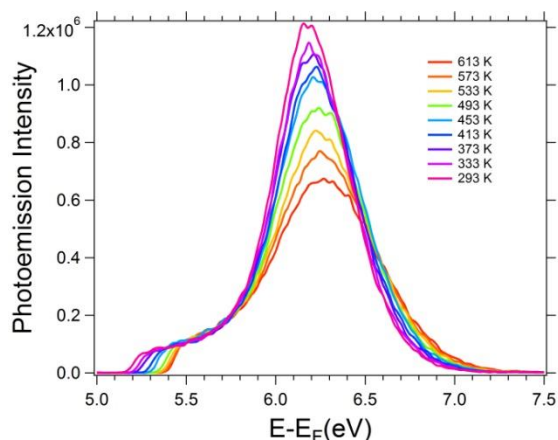


Figure 4.6-2PP spectra of the $t_{2g}-e_g$ transition with s-polarized 360 nm (3.44 eV) light with the [001] crystalline axis aligned to the optical plane for a range of temperatures upon cooling the sample from 600 to 300 K. This data set shows a continuous change of 2PP spectra for the d-d transition through the desorption temperature of OH at ~490 K, which eliminates the assignment to the wet electron state of OH as the dominant carrier of the spectrum.

This is consistent with the assignment of 2PP to the resonant $t_{2g}-e_g$ excitation. This d-d transition exists throughout the temperature range of the measurements for reduced TiO₂ surfaces; the temperature dependent changes in the resonance energy and width is consistent with a polaron description of the Ti-3d defect state electrons on TiO₂, as will be elaborated in Chapter 5, as well as more generally the thermal broadening and shrinking of optical band gaps of solids.[193] There is no evidence for abrupt changes in 2PP spectra with temperature that could portend changes in surface composition. The 2PP spectra on cooling are consistent with those on heating. Zhang et al. reported similar 2PP spectra, but a gap in their

measurements between 373 and 536 K gave a false impression of a discontinuous change that might occur upon OH desorption. Their temperature dependent 2PP spectra show conclusively that the resonance enhancement exists even above 490 K, although thermal broadening effects diminish its intensity, as in figure 4.5.

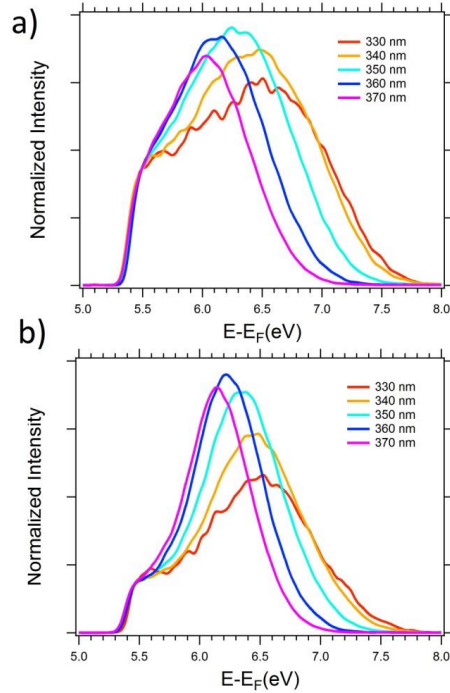


Figure 4.7-2PP spectra taken with several excitation wavelengths between 330 and 370 nm (3.76-3.35 eV) at 600 K with the crystal axis oriented so that the [001] direction is in the optical plane for a) s-polarized and b) p-polarized excitation. The data are normalized at the work function edge to better show the resonance behavior. The s- and p-polarized spectra have different lineshapes because the former has only the isotropic contribution, whereas the latter also includes the anisotropic contribution to the d-d transitions.

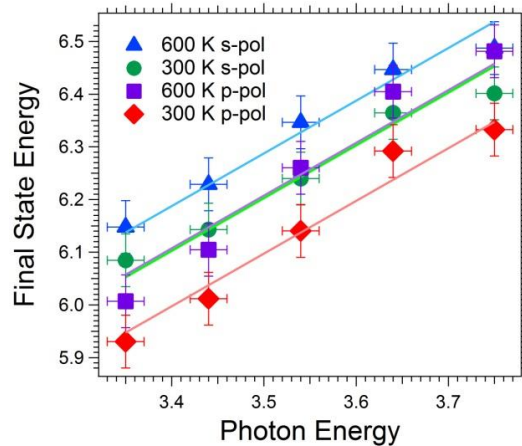


Figure 4.8- The plot of final state energy of the d-d resonance vs. photon energy for the p- and s-polarized excitation at 300 and 600 K. The approximate slope of 1 for both the high energy (s-polarized) and low energy (p-polarized) peaks is expected for two photon transitions through real intermediate states.

Further measurements are performed above OH desorption temperature as a function of wavelength. Figure 4.7a and 4.7b shows representative spectra at 600 K for several excitation wavelengths with s- and p-polarized light. Both intermediate states are clearly present at 600 K, and as shown in figure 4.7,

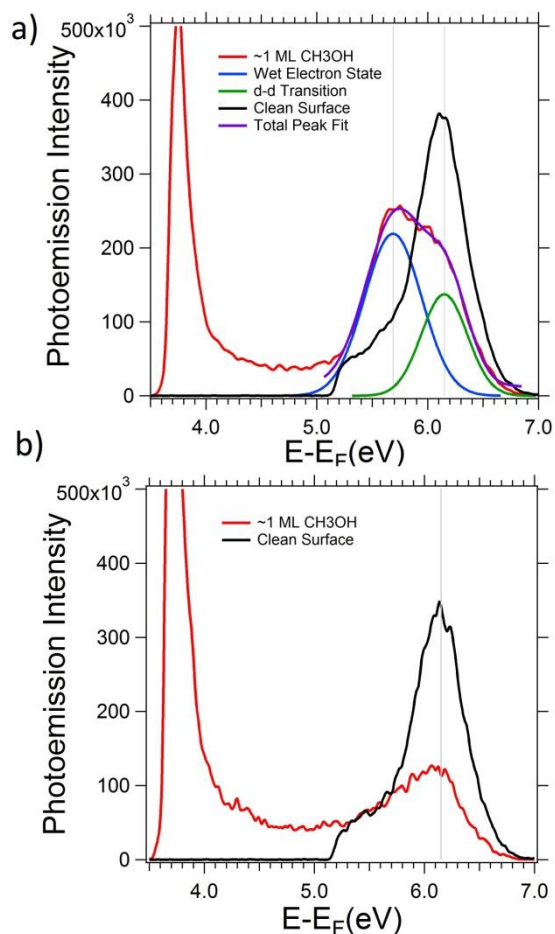


Figure 4.9- Clean and CH₃OH covered surfaces for a) p-polarized and b) s-polarized excitation with 360 nm ($h\nu=3.44$ eV; 100 K) light. The p-polarized data are fit with two Gaussian profiles for the wet electron and d-d transitions to locate their energies at 2.25 and 2.71 eV above E_F . The dotted vertical lines indicate the resonance energies. The strong photoemission signal for CH₃OH covered surfaces near the vacuum edge is due to contribution of one-photon photoemission.

independent of the substrate azimuth,[71] whereas for the $t_{2g}-e_g$ transition, the isotropic component can be excited with any polarization, but the anisotropic component must have the electric field aligned with the $[1\bar{1}0]$ direction.[84] To incisively determine the differences between wet electron and d-d excitations, I align the sample such that the $[1\bar{1}0]$ direction is inclined by 45° relative to the optical axis. In this configuration the d-d transition is excited equally with either p- and s-polarized light whereas the

the photoemission energy is linearly dependent on $h\nu$ as expected for 2PP processes via real intermediate states. The spectra in figure 4.7 and their analysis in figure 4.8 are consistent with enhancement of the 2PP process by two real intermediate states separated by 0.13 eV with polarization dependent matrix elements, rather than the coherent and sequential excitation pathways involving a single intermediate state, as claimed by Zhang et al. [192]. The two resonances can simply be identified and spectrally analyzed by taking advantage of the vectorial nature of their transition moments, as was done in Figure 4.2.[84]

Next I address the claim that the $t_{2g}-e_g$ transition is really a wet electron state of OH but shifted up in energy from the previously reported values [71,194]

due to lack of energy stabilization by coadsorbed water, as claimed by Zhang et al.[192] To distinguish between the wet electron state and e_g mediated 2PP, I consider differences between the transition moments for the two processes. The wet electron state can only be excited with p-polarized light

wet electron state is only excited with p-polarized light.[71] Figure 4.9 shows the results of this experiment for both the clean surface and after adsorption of ~ 1 ML of CH_3OH . I investigate CH_3OH rather than H_2O because its wet electron state at 2.3 eV is 0.1 eV lower than that for H_2O so the overlap with the d-d transition is reduced.[71,72] For the clean surface, the 2PP spectra in figure 4.9a and 4.9b are identical for the p- and s-polarized excitation, as expected, and the d-d transition is marked by a vertical line. After adsorption of the CH_3OH a clear difference between the p- and s-polarized spectra appears. Whereas the s-polarized spectrum still shows the d-d transition at the same energy but with attenuated intensity, the p-polarized spectrum shows an additional peak, at the expected energy for the wet electron state.[72] The resonances in the p-polarized 2PP spectrum can be fit with two Gaussians corresponding to intermediate wet electron and e_g states at 2.25 and 2.71 eV. For both polarizations the adsorption of methanol partially attenuates the d-d transition, but it remains a parallel process for p-polarized excitation with approximately the same intensity as the wet electron state.

These measurements definitively show that the wet electron and d-d transitions coexist on methanol covered reduced TiO_2 surfaces, and the d-d transition cannot be interpreted as a low CH_3OH or H_2O coverage counterpart of the wet electron states. As previously calculated,[71,181] at low density, *i.e.*, when a wet electron state is supported by single bridging OH, its energy is substantially higher than for a full protic solvent monolayer coverage; most likely, its resonance width is significantly broader than for a monolayer coverage due to stronger coupling with the conduction band of TiO_2 , or the free electron continuum in the vacuum.[70,71,181] Therefore, contrary to the assignment by Zhang et al., the wet electron state of single OH has not been observed by 2PP spectroscopy.

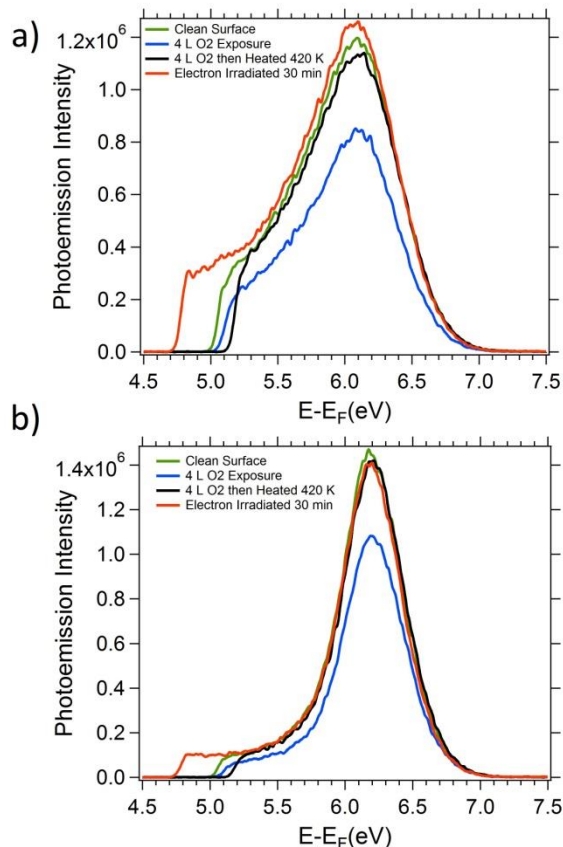


Figure 4.10- 2PP spectra of TiO₂ surface for various surface preparations with 360 nm excitation ($h\nu=3.44$ eV; 300 K). The green line shows a reduced surface prepared via standard method as explained in the text. The blue line shows spectra after the reduced surface is exposed to 4 L of O₂. The black line shows the spectra after heating the O₂ exposed surface to ~ 420 K to remove O_t from the Ti_{5c} sites and subsequent cooling to 300 K. Red line shows spectra after irradiating the standard surface with 500 eV electrons and beam current of 50 nA for 30 minutes to create O_b vacancy defects.

Whether the bridging OH species is present on the TiO₂(110) surface, as required for the assignment of Zhang et al., depends on the surface preparation procedure and the quality of vacuum. I therefore investigate 2PP spectra of TiO₂ for various surface preparations. Surface OH can be introduced with controlled density by exposing reduced surfaces to H₂O. Reduced TiO₂(110) surfaces have typically 10% bridging O_b atom vacancy defects where H₂O undergoes thermally activated dissociation.[195] The dissociation of each H₂O molecule produces two bridging OH species, which can subsequently diffuse along the bridging O atom rows.[195-198] These surface OH are the putative carriers of 2PP spectra in Zhang et al's work.

Just as O_b vacancies control the density of surface OH, the chemisorption of O₂ can be used to remove surface OH to produce nearly perfect bridging O atom rows.[29] Exposing the surface to ~ 4 L of O₂ was shown to remove most of the OH from the surface and concomitantly heal the O_b atom vacancy defects,

which prevents re-adsorption of OH. The dissociation of O_2 at room temperature at the surface O_b atom defects produces terminal O atoms (O_t) on five coordinate Ti sites (Ti_{5c}). Annealing the surface to >410 K removes the O_t species either by recombination to form O_2 , which desorbs, or by reaction with interstitial Ti atoms in the subsurface region.[29,199-202] Figure 4.10 shows 2PP spectra of TiO_2 for various surface preparations. I measure the baseline spectra at room temperature corresponding to our standard preparation. Exposing this surface to 4 L of O_2 is expected to heal the majority of surface O_b vacancies and remove the OH that might have formed on the bridging O atom rows. This procedure reduces the d-d transition intensity by $\sim 25\%$ with respect to the baseline spectrum and increases the work function by 0.1 eV, as expected for a more oxidized surface.[36] If the surface OH were responsible for the observed resonance then removing most of OH from the surface should effectively extinguish the transition intensity. Instead the decrease in intensity is consistent with healing of the surface O_b atom vacancy defects, which mainly decreases the surface, but not the subsurface (second and third layers below the surface) or bulk, Ti-3d defect state density.[29] Thus, the incomplete quenching of the d-d transition with O_2 exposure suggests that the dominant contribution to the d-d transition is associated with the *bulk* interstitial Ti defects (including the subsurface region).

After exposing the surface to O_2 , I remove the O_t species by annealing the surface to 420 K, and then rapidly re-cool it to room temperature to remeasure the 2PP spectra. The annealing temperature is well below the desorption temperature of OH and O_2 from the O_b rows, but it coincides with the onset of diffusion of subsurface Ti interstitial atom defects.[29,203] This surface, which should now be free of OH, shows identical intensity as our standard reduced surface. This strongly implies the carrier of the spectrum of the d-d transition is not a surface species but is predominantly related to the interstitial Ti defects, whose density is hardly affected by the oxidation/annealing procedure.

To reinforce the conclusion that the bulk defects make the dominant contribution to the 2PP spectra, the sample is then irradiated for 30 minutes with 500 eV electrons, which is also expected to remove surface OH and increase O_b vacancy defects.[204] The only effect of the energetic electron irradiation of the surface is to decrease the work function, which is consistent with an increase of O_b vacancy defects. The t_{2g} - e_g transition intensity, however, remains the same reinforcing our conclusion that the interstitial Ti atom density primarily defines the intensity of the observed 2PP spectra.

Wendt *et al.* and Yim *et al.* addressed the origin of the Ti-3d defect density in UPS spectra by augmenting the spectroscopic measurements with STM based surface characterization.[29,34,35,205] In agreement with our study, Wendt *et al.* concluded that resonant photoemission with 47.5 eV light predominantly probes the subsurface and bulk Ti interstitial defect density.[29] By contrast, using a He I light source, Yim *et al.* attributed the UPS spectra to the surface O_b atom vacancy defects.[34] As noted already, Ti-3d electrons introduced from either source exist as small polarons with a spectral signature that is independent of the particular donor impurity.[206] The contradicting interpretations can probably be attributed in part to light source dependent sensitivities to the surface and bulk defects. I expect that 2PP measurements with UV light should be most sensitive to the bulk defects, because based on the universal inelastic mean free path curve,[207] the probing depth of 6 eV electrons is ~ 4 nm as compared with ~ 1 nm for the UPS measurements. Moreover, the 2PP measurements depend on the resonant d-d transition, which is sensitive to the local environment of the defect charge density, and therefore may have different transition moments for the surface and bulk excitations.

Finally I address whether the d-d transitions are important for extending the photocatalytic activity of TiO_2 into the visible spectral region, as suggested by Thornton and Yang and coworkers.[192,208] Because the e_g bands are ~ 2.7 eV above E_F one might argue that they could be excited by visible light from E_F . Our wavelength dependent 2PP spectra, however, indicate that the density of occupied states near E_F of TiO_2 is very small and therefore the efficiency of exciting the e_g states with visible light is correspondingly small.[84] 2PP spectra of TiO_2 with 3.0 eV and lower energy excitation show no sign of the d-d resonance enhancement, and therefore most likely are excited through a nonresonant two-photon absorption process, as proposed previously.[36,71]

4.4 mPP Photoexcitation Dynamics

The $t_{2g}-e_g$ transition exhibits additional features, which illuminate the photoexcitation dynamics in TiO_2 . The most notable is the variation of the mPP spectral width of the e_g peak with increasing photon energy, which can be seen in Fig. 4.2(a). I attribute this characteristic to a combination of effects, including (i) the variation in pulse duration of the laser with the wavelength; (ii) the broad distribution of defect states, which have a sharp cutoff at E_F ; and (iii) the increasing contribution of the 3PP component in the predominantly 2PP spectra, which sets in as the photon energy is tuned into the direct band gap of TiO_2 .

A related feature to the peak broadening is an apparent shift of the e_g peak in mPP spectra to higher energy as the laser intensity is increased (Fig. 4.11). This is not an artifact of space-charge distortion of the photoelectron distribution, because the photoelectron yield from TiO_2 is much less than for metal surfaces under conditions where such distortions are not observed, and more directly, because the work function edge does not experience a shift. I will show that the shift occurs because the defect state density is low, and can be depleted at high laser fluences, leading to saturation of the transition. The low density of defect states makes it easier to saturate the transition relative to bulk interband transitions. Simultaneously, the band-gap excitation of TiO_2 can populate the CB, so that that the 3PP photoelectron yield from the valence band (VB; see figure 4.1) can overwhelm that of 2PP from the defect states. The 3PP excitation can occur via a coherent three-photon absorption, or via a sequential process where electrons excited to CB relax before absorbing an additional two photons (figure 4.1).

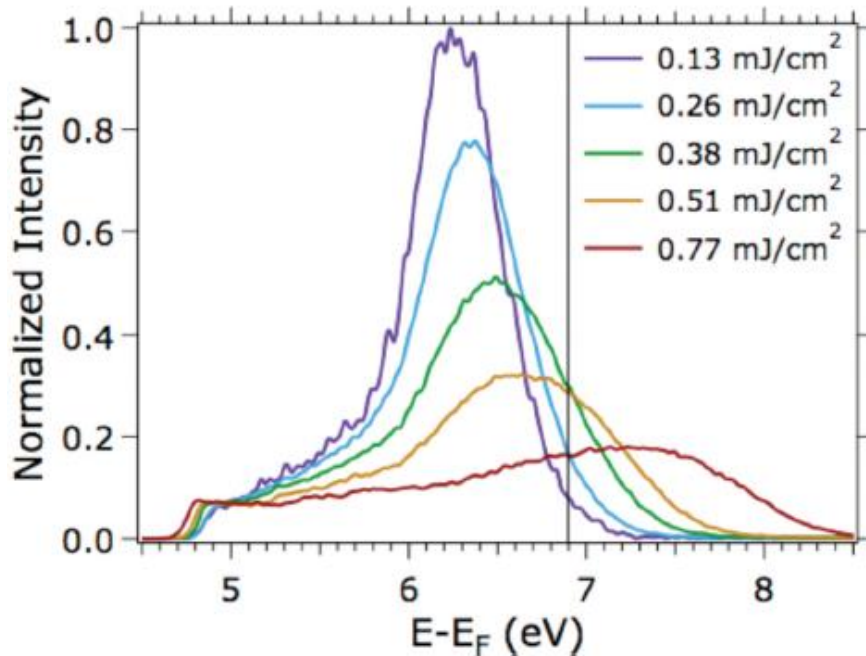


Figure 4.11- mPP spectra for various laser fluences for excitation at 3.50 eV (354 nm) showing the saturation of the $t_{2g}-e_g$ transition and the onset of 3PP above the 2PP Fermi level edge (black line). The spectra are normalized at the work function edge.

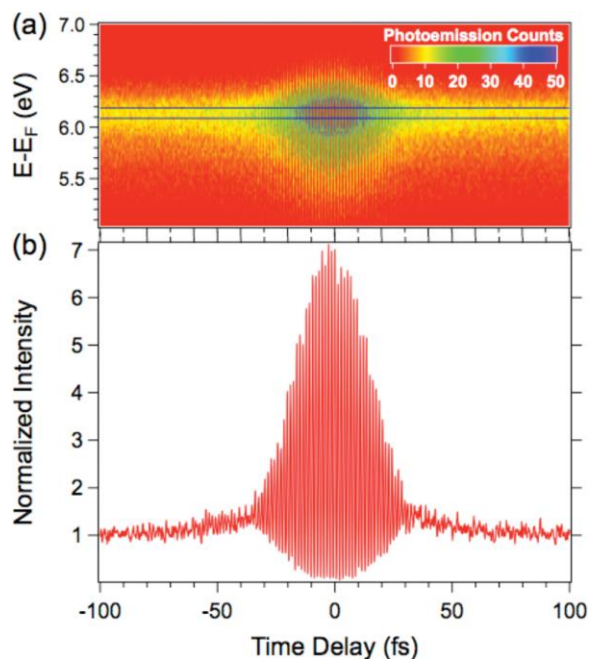


Figure 4.12- (a) Interferometric two-pulse correlation measurement for ± 100 fs delay taken with $h\nu = 3.27$ eV for the TiO_2 sample. (b) Line profile of the data for the energy range shown by the black lines in (a). The interferogram corresponds to pulse duration of ~ 22 fs; its nearly 8 to 1 intensity ratio is expected for a two-photon process.

The saturation of the $t_{2g}-e_g$ transition and the competition between 2PP and 3PP is clearly evident in figure 4.11. The fluence-dependent spectra are normalized at the work function edge, where the saturation effect is minimal and the 2PP process does not appear to be enhanced by an intermediate state resonance. The Fermi edge for the 2PP process is marked with a vertical line for reference. Even at lowest laser intensity there is some signal above the Fermi level edge due to the bandwidth of the laser, and thermal broadening of the Fermi distribution. The photoemission signal above the 2PP Fermi edge can also have contributions from 3PP and higher-order processes [209]. At higher fluences, the relative intensity of the e_g peak decreases and the 3PP intensity above the E_F limit increases. I confirmed that this effect is dependent on the peak and not the average power of the laser by varying its repetition rate and the pulse energy so as to keep the average power constant. This excludes the possibility that the 3PP process involves a buildup of carriers in the CB on the time scale between the laser excitation cycles or that the sample charging influences the spectra. Although under some circumstances the carrier lifetimes in TiO_2 can extend to the millisecond time scale [210], the slow carrier recombination does not appear to affect the mPP signal from the single-crystal TiO_2 surface in vacuum at MHz repetition rates. It is possible that the carrier recombination in the absence of molecular electron or hole traps is sufficiently fast to remove CB carriers between each cycle of excitation, or that the upward band

bending near the surface sweeps electrons into the bulk of the crystal where they are not detected [211].

The photoelectron energy distributions in figure 4.11 reflect the nature of the 3PP process. In metals under perturbative light-surface interaction, higher-order mPP processes usually involve above-threshold photoemission, where absorption of an additional photon by electrons excited above E_{vac}

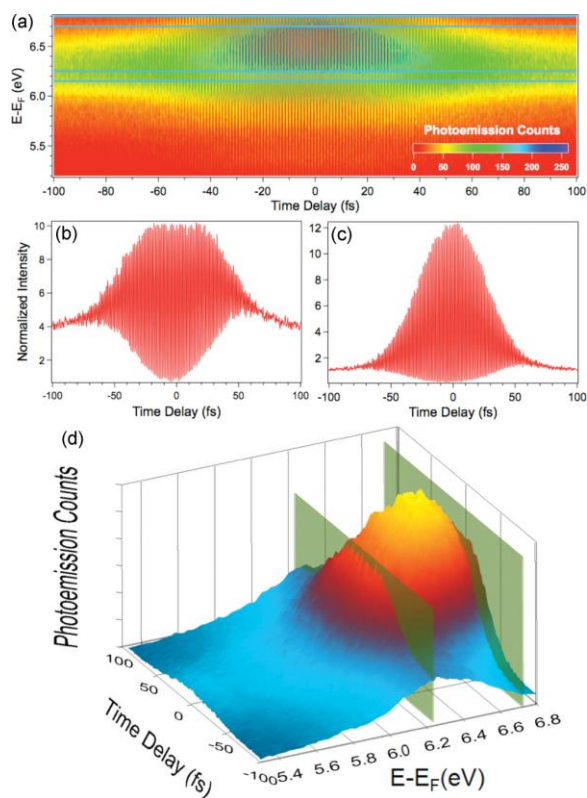


Figure 4.13- (a) Interferometric two-pulse correlation measurement taken with $h\nu = 3.40$ eV for the TiO_2 sample under saturation fluence. (b) Line profile taken at 6.20 eV, corresponding to the photoelectron energy where the e_g peak energy would be observed at low laser fluence or long delay times (e.g., ± 100 fs). (c) Line profile taken at 6.75 eV, corresponding to the peak in the photoelectron signal under saturation fluence at 0 fs delay. The peak-to-background ratios show evidence of the 2PP saturation (b) and contribution from 3PP (c) at high laser fluences. (b) and (c) are plotted on the same relative intensity scale. (d) A quasi-3D plot of the in-phase contribution of the ITR-2PC signal in (a) showing the photoemission energy distributions at different delay times with the energies for the cross sections in (b) and (c) designated by the intersecting planes.

thereby to flatten the surface bands. Such surface photovoltage effect has been claimed in 2PP spectra

creates a replica of the spectrum excited by the lower-order process [209]. This clearly is not happening in TiO_2 . The higher-order 3PP signal is initiated from the more deeply bound occupied states in the VB rather than replicating the 2PP spectrum from the defect states. Therefore, one might expect the maximum photoelectron energy via the 3PP process to correspond to emission from or below the VBM. From the spectra in figure 4.11 it is difficult to identify a clear VBM cutoff, which should occur at 7.7 eV for excitation of bulk rutile TiO_2 with three 3.5 eV photons. Contrary to this expectation the observed spectrum extends beyond 8 eV, which might be attributed to excitation of initial states above the VBM. The most plausible explanation for this excess photoelectron energy is an upward surface band bending, which is ~ 0.4 eV for TiO_2 surfaces annealed in O_2 atmosphere [211]. Because the photoelectron escape depth is much less than the surface accumulation region, the 3PP spectra can be strongly affected by the surface band bending. By contrast, the defect density distribution is pinned at the same Fermi level for the surface and in the bulk.

Under high-density excitation of a semiconductor surface it is possible to screen the surface fields, and

of ZnO [172], though the same features can be explained by the formation of a surface exciton [173]. Flattening of the surface band bending should cause the CBM to shift with respect to E_F . In the present measurements, the CBM of $\text{TiO}_2(110)$ is not observed; therefore, the effect of surface photovoltage in the mPP spectra is difficult to identify among other nonlinear processes.

In addition to the mPP spectra, I also measure Interferometric Time Resolved Two-Pulse Correlation (ITR-2PC) scans to gain information on the ultrafast electron photodynamics. Figure 4.12 shows an ITR-2PC scan obtained with identical 3.26 eV photon energy pump-probe pulses; figure 4.12 also shows a cross section through the 3D data corresponding to 2PP intensity vs. the final state energy and delay time for the surface normal emission [85]. The interferogram in Fig. 4.12(b) is a line profile through the data for the final state energy of 6.2 eV, corresponding to the e_g resonance. The interferogram is indistinguishable from the pulse autocorrelation measured by 2PP on the Mo sample holder. Its appearance, i.e., the nearly 8:1 ratio of the fringe-to-background signal and duration of the interference, are consistent with a 2PP process excited with ~ 22 fs laser pulse. As in the previous TR-2PP measurements [71], I am not able to resolve the electron phase and population relaxation dynamics at 2-3 eV above the CBM of $\text{TiO}_2(110)$.

When ITR-2PC is measured at 3.40 eV using a high laser fluence [figure 4.13(a)] the interferograms obtained from line profiles at different energies [figures 13(b) and 13(c)] show evidence for more complex photodynamics than in figure 4.12. In figure 4.13(b), the interferogram at the 6.20 eV final state energy for the 2PP excitation from the Ti-3d defect states through the e_g resonance shows clear evidence for the saturation of the optical transition in the clipping of the amplitude of the interference fringes at short delays and the small ratio of the fringe-to-background emission amplitudes. By contrast, the mPP signal near the E_F edge (6.75 eV), i.e., for the region where 3PP from the VBM contributes to the photoemission signal, the line profile with a ratio of $>8:1$ is consistent with contributions from both 2PP and 3PP processes. This ratio becomes even larger for higher final state energies as the contribution from 3PP increases relative to 2PP. The saturation behavior is also observable in figure 4.13(d), which shows the amplitude of the mPP signal in figure 4.13(a) when the pump-probe delay is in phase for the carrier wave of the excitation pulses. Near the zero delay, when the pump and probe excitation fields interact coherently, the peak in the mPP signal shifts to higher energy; this corresponds to the high intensity excitation in figure 4.11, where the $t_{2g}-e_g$ transition is saturated and the 3PP process dominates.

When the delay is increased beyond the range of pump and probe interferences, the signal maximum shifts to 6.2 eV, where it is expected from the low fluence measurement in figure 4.11. This is consistent with pump and probe pulses individually exciting the 2PP process from the Ti-3d defect states via the e_g intermediate state without a significant correlated contribution from transient changes in the electron and hole populations. If the carrier energy relaxation were to occur on the time scale comparable to the pump-probe delay, one would expect the pump pulse to deplete the defect states, and the probe emission to be diminished (2PP). Similarly, if the pump pulse would populate the CB of TiO_2 , the delayed probe pulse induced emission would be enhanced (incoherent 3PP) [123,212]. Such dynamics have been reported in two-color 2PP measurements on ZnO, where high photon energy UV probe pulses excite single photon emission from near the E_F [172,173], instead of the one-color experiments performed here, where the hot-carrier distributions can only be interrogated by two-photon absorption. The fact that the population relaxation is not evident in ITR-2PC measurements is consistent with the 2PP and 3PP processes reported herein being dominated by the coherent interactions involving the intermediate and possibly final state resonances. It appears that incoherent, hot electron mediated pathways, such as described by the dark green arrows in figure 4.1, make negligible contributions. It is also possible that carrier relaxation by e-p and e-e scattering in TiO_2 is much faster than our pulse duration, which would be consistent with the calculated hot electron lifetimes [170,171]. The hot-carrier dynamics in TiO_2 are likely to be more easily resolved in two-color experiments near the CBM, as has been done for ZnO [172,173].

4.5 Conclusion

Multiphoton photoemission is carried out on a $\text{TiO}_2(110)$ surface using 2.95–4.59 eV photon energy light with ~ 20 fs pulse duration. For excitation with 3.2 eV and higher photon energy I find a distinct pair of nearly degenerate unoccupied bulk states of TiO_2 at 2.73 ± 0.05 and 2.85 ± 0.05 eV above the Fermi level. These states are excited from the O-atom vacancy defect states and are consistent with transitions between the Ti-3d band of t_{2g} - and e_g -symmetry, which are split by the crystal field. Polarization and crystal orientation dependent measurements of the t_{2g} - e_g transition reflect the anisotropy of the TiO_2 rutile crystalline lattice. In particular, the t_{2g} - e_g transition from the defect states dominates the 2PP spectra when the electric field of the excitation laser points in the $[1\bar{1}0]$ crystalline direction; this implicates transitions from defect states with the same symmetry as the CBM+1 band. The spectroscopic assignment of this resonance is supported by DFT calculations, which confirm the anisotropic nature of the excitation process. I have performed various tests that exclude surface OH as

the possible carrier of the spectrum, as assigned by Zhang et al.[192] Furthermore, O₂ adsorption and electron irradiation of the surface suggest that the bulk defect states dominate the 2PP spectra.

Time-resolved measurements are performed to probe the e_g state lifetime, as well as those of the hot carriers near the Fermi level. In both cases, the lifetimes appear to be <20 fs, though the preference for coherent pathways in the mPP measurements may make contributions of hot-carrier populations difficult to observe [123,212]. The ultrafast decay of the e_g state most likely makes it inactive in TiO₂ photocatalysis, though it may be useful for optical probing of the charge-carrier dynamics within the VB and CB of TiO₂. The lack of observable electron relaxation processes even from the e_g resonance is consistent with the previous measurements on clean TiO₂ surfaces [71], and confirm that the long electron lifetimes for the catechol covered TiO₂ surface [168] do not represent the intrinsic hot electron dynamics of TiO₂. Additionally, the saturation effect at high laser fluences leads to a shift and broadening of the e_g peak due to the depletion of the defect carrier density. 3D time-resolved photoemission measurements show evidence for the competition between the 2PP and 3PP processes at the onset of the direct band-gap excitation of TiO₂.

The optical transitions between the t_{2g} and e_g bands may be important for optical spectra of photoexcited TiO₂. If the CB is populated by band-gap excitation of TiO₂, the photoexcited carriers could be detected via the t_{2g}-e_g transition in transient absorption experiments. Absorption features in the blue-green region of the optical spectrum have been assigned to trapped holes [160,182]. Our results, however, clearly show that the CB electrons also absorb in the same energy region. Therefore, the t_{2g}-e_g transition may be beneficial for studying the CBM dynamics of photoexcited carriers, especially by mPP spectroscopy where the electron and hole levels are unambiguously distinguished.

Finally, since it is unlikely that a weak photoexcitation of these short-lived bulk states with visible light could have any practical impact on TiO₂ photocatalysis, I instead make a more penetrating claim that the t_{2g}-e_g transition provides a window on the nature of trapped carriers in TiO₂ and their interactions with adsorbates at the photocatalytic interface. Moreover, the 2PP measurements provide a valuable spectroscopic probe of the Ti-3d density that imparts emergent electronic properties in a large class of quantum materials that are currently under intense scrutiny.[206,213-215] Finally, d-d transitions occur in most metal oxide materials and thus the ability to probe them in 2PP experiments extends the ultrafast spectroscopic tools to study their electronic properties in catalysis and interactions of spin, orbital, and lattice degrees of freedom in correlated materials.[216-219]

5. Chapter Five: Multi-Photon Photoemission Spectroscopy of Polarons on TiO₂(110)

5.1: Introduction

In the previous chapter I considered the electronic structure and photoexcitation dynamics of clean, reduced TiO₂ surface using the Ti-3d defect states as initial states in mPP processes. In order to understand the photocatalytic properties of TiO₂ such as the reactivity of H₂O and CO₂ on the surface, I also need to examine the nature of the band edge carriers, including the defect states, which could be involved in reduction of adsorbed molecules.[1,3] Recent experiments and theoretical calculations have addressed the polaronic character of electrons in the CB of TiO₂ and its impact on the photocatalytic properties.[220-226] The interaction of excess charge introduced into the CB of TiO₂ surface with the ionic lattice determines its localization and transport properties. The experimental and theoretical descriptions of this interaction and its consequences are of significant topical interest.[156,227-231] The character of electron-lattice interaction is likely to impact charge transport in various electronic and photoconversion applications of TiO₂. The polaronic character of Ti-3d electrons in an ionic lattice is broad interest because in related transition metal oxides, a transition from an insulator to a semiconductor, and finally a metal occurs with changing doping and temperature due to these interactions.[232] In this chapter I will discuss the polaronic character of the CB carriers of TiO₂ by performing 2PP spectroscopy on the clean rutile TiO₂ surface as a function of the sample temperature. In the previous chapter I noted that the t_{2g} - e_g transition is strongly temperature dependent in the 300-600 K range. Here I extend the measurements to 30-600 K range and discuss the energy, linewidth, and intensity dependences in terms of electron-phonon interaction including the formation of a polaronic state.

In crystal lattices of conductors such as good metals the lattice is taken to be formed of lattice ions that are frozen in place. Due to the high mobility and strong delocalization, electrons move through the lattice unimpeded except for scattering with phonons. At low temperatures when phonon excitation is minimized, the influence of the lattice (phonon absorption) on electron transport can be frozen out. However, in ionic systems such as semiconductors and polar crystals this approximation fails because

screening is weaker, and therefore the effect of Coulomb interaction between conduction electrons and the crystal lattice is much stronger.[233] The interaction of electrons and phonons plays an important role in determining charge transport, and electrical and thermal conductivity of a material; characterizing the effects of electron-phonon interaction is important for photovoltaic or photocatalytic applications. In an ionic crystal such as TiO_2 the interaction of the excess electrons with the lattice causes the lattice to distort as shown in figure 5.1. This distortion of positive and negative ions around the electron can be described as a cloud of virtual phonons. The net interaction is attractive and causes the electron to be localized by the lattice distortion as a quasiparticle called polaron.

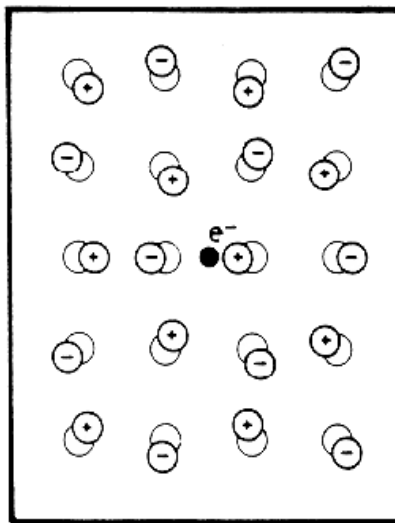


Figure 5.1- An excess electron in an ionic crystal causes the lattice to distort around it, forming a quasiparticle called a polaron.[234]

The concept of a polaron was first introduced by Landau in 1933 and has since garnered significant attention and elaboration.[235] In general a polaron is described as either large or small depending on the size of its interaction in relation to the lattice constant of the material. Both large and small polarons are caused by interaction primarily with the longitudinal optical (LO) phonons, which can be taken as having a fixed frequency. A large polaron involves lattice distortion that extends over many unit cells; this makes it possible to describe it with a continuum approximation for the lattice. Additionally it is assumed that the electrons have parabolic dispersion and that spin and relativistic effects can be ignored.[234] With these assumptions one can describe the interactions between an electron and virtual phonons in terms of a coupling constant α developed by Fröhlich and defined in equation 6.1.[236]

$$\alpha = \frac{e^2}{\hbar c} \sqrt{\frac{m_b c^2}{2\hbar\omega_{LO}}} \left(\frac{1}{\epsilon_\infty} - \frac{1}{\epsilon_0} \right) \quad (5.1)$$

where m_b is the bare band mass of the electron, ω_{LO} is the LO phonon frequency, ϵ_∞ is the high-frequency electronic dielectric constant and ϵ_0 is the static dielectric constant. As the coupling constant grows the strength of polaronic effects grow as well. Experimentally it is difficult to measure the bare band mass of an electron due to the renormalization by the polaronic effect. This is due to the fact that the electron drags the lattice distortion with it as it moves through the crystal. In a large polaron this mobility is band like, but with an increased effective mass arising from the interaction. As the lattice is heated the mobility of a large polaron is limited by scattering by optical phonons. This mobility can be described in relation to the Debye temperature and is proportional to $\exp\left(\frac{\theta}{T}\right) - 1$, where θ is the Debye temperature.[233]

As the coupling constant increases, the excess electron in the lattice localizes more strongly and the distortion is confined to a smaller volume. If the distortion is confined to within a few unit cells, then the continuum approximation begins to break down and a new approach is needed. This limit is referred to as the small polaron, where the distortion is localized essentially within a single unit cell. The stronger localization limits the mobility of the polaron to a “hopping” mode, which is induced by coupling with the LO phonons in the system. Therefore, the mobility of a small polaron increases with increasing lattice temperature, and therefore the LO phonon occupation. Since the small polaron only interacts with a small number of lattice ions it can be calculated using *ab initio* techniques rather than a continuum approximation.[233,234] Such *ab initio* approach is difficult for large polarons because it requires the use of very large unit cells.

Polarons are common in many semiconductor materials, and are particularly important in tetrahedral semiconductors. Incorporating the effect of electron-phonon interactions, and polarons in particular is important for reconciling theoretical calculations of the band structure and its change with temperature with that of experimental measurements.[227,237] These calculations generally assume a fixed crystallographic position of the lattice and ignore the phonon induced lattice vibrations. The effect of these vibrations on the band structure can be significant for semiconductors. [238]. Polarons have been found to be important in topics ranging from high temperature superconductivity, resistive switching, photocatalysis ,and multiple other phenomena and applications.[239-249]

Recently TiO_2 has been investigated for its polaronic properties in relation to how it affects the conductivity and charge transfer for photovoltaic and photocatalytic effects. In anatase TiO_2 the polaron has been theoretically and experimentally shown to be in the large limit.[186,223,250,251] However, in rutile the discussion has been more involved. Recent theoretical studies have shown the possibility of a large polaron, a small polaron or a mixed state of both.[252-255] This lack of consensus and paucity of detailed experiments was one of the motivations for the experiments discussed in this chapter.

In TiO_2 the excess electrons that form the polaron can be either introduced by band gap excitation or reduction. As has already been introduced, in reduced TiO_2 the source of excess electrons is either from Ti^{3+} interstitials or oxygen vacancies; both populate the Ti-3d bands, which can form polarons. These orbitals are derived from the d-bands at the bottom of the CB and have t_{2g} symmetry. Without the polaronic interaction, these electrons could occupy either the CB or remain bound to the defect. If the polaronic interaction is sufficiently strong, the electrons can be localized by lattice distortion rather than the charged defects. The Ti-3d orbitals associated with the defects form a defect band with maximum density-of-states (DOS) at 0.8 eV below the E_F . This DOS is broad and extends up to E_F at room temperature, which is 0.2 eV below the CBM.[180,256] There has been a debate whether this band should be attributed to polarons or electron localization by ionized impurities.[70,223,249,254,257-261]

Previous studies involving 2PP experiments with 400 nm Ti-Sapphire lasers have shown that surface preparation and molecular adsorption are very important for the understanding of photoemission from the defect band of TiO_2 . [36,70-72,262] In addition to these studies, molecule covered surface studies have also been conducted as discussed in the previous chapter. I build upon these results in order to further advance the understanding of the TiO_2 surface and charge transport properties. Here I show evidence for existence of a polaronic state through temperature dependent 2PP spectroscopic measurements. I probe the t_{2g} - e_g transition for the clean TiO_2 surface over the 30-633 K temperature range. These measurements show that both the t_{2g} and e_g states undergo a shift and broadening as the sample temperature is increased. These spectral changes can be attributed to the electron-phonon interaction as well as the thermal expansion of the lattice. The shift in the defect state density due to these interactions leads to a change in the resonant energy and width of the previously reported t_{2g} - e_g transition. By performing 2PP spectroscopy with tunable laser excitation I can determine both the temperature dependent resonance energy as well as the absolute energies of the t_{2g} and e_g bands with respect to the E_F . The ability to perform electronic spectroscopy over a wide energy and temperature range significantly improves our understanding of electron-phonon interactions in TiO_2 .

The electron phonon interaction and the effect of the formation of a polaron on the rutile TiO₂ surface has recently generated much of interest due to its potential to help understand the charge transport and photocatalytic properties of TiO₂. A number of theoretical studies have been conducted that aim to understand the origin of this polaron and how it affects the properties of rutile. Moses et al. found that the introduction of charge by oxygen vacancies causes a small polaron to form, in either a single or double polaron configuration. They also found that the presence of vacancies on the surface did not produce the gap state, but instead the polaron formed due to intrinsic and subsurface defects.[263] Several other groups have recently calculated the effect of oxygen vacancies on the polaron formation, with a similar conclusion that the excess electrons can localize into the polaron state.[220,221,264] This recent theoretical work agrees well with the results discussed in chapter 4 which indicated that the surface oxygen vacancy was not the primary source of the t_{2g} state. Further theoretical studies have compared the polaron formation of rutile with that of anatase and found that the strong localization of the excess electrons in rutile form a small polaron while the excess electrons in anatase favor a more delocalized configuration of a large polaron. [223,249]

5.2: Experimental Details

The experimental apparatus for mPP measurements on TiO₂ surfaces have been described previously in chapter 3 of this thesis. The sample is a TiO₂(110) rutile single crystal obtained from Princeton Scientific Corp. The preparation method is the same as used in the previous chapter. For experiments that require minimum contamination the UHV chamber is pumped with an additional cryopump, which improves the base pressure of the system to $\sim 8 \cdot 10^{-11}$ mbar and thereby reduces the surface contamination during measurements. Cryopumping of the chamber enables the work function to remain above 5 eV for several hours even when the sample is cooled to liquid helium temperatures. Flash heating the sample to 500 K after cooling the sample together with cryopumping further minimizes the impact of impurity adsorbates on the measurements.

The 2PP measurements are performed in a temperature range from 633 to 30 K in approximately 40 K intervals. The high temperature data is acquired by preparing the sample and then reheating it and manipulator above 633 K, and then allowing the system to equilibrate for 5 minutes. Subsequently, the 2PP spectra are recorded as the sample is cooled. LN₂ cooling is used for all experiments down to 80 K, and LHe₂ cooling is used to obtain data below that temperature.

5.3: Results and Discussion

In Chapter 4, I described the 2PP spectroscopy of the t_{2g} - e_g transition of $\text{TiO}_2(110)$ at room temperature; the analysis of the spectra revealed a pair of well defined peaks at 2.60 and 2.73 eV above the Fermi level due to e_g symmetry bands [265][84]. To review, the 2.73 eV band is more intense and sharp than the 2.60 eV band; it is excited when the electric field of the laser light is along the [110] direction, whereas the 2.60 eV band is isotropic. The temperature dependent measurements used to exclude OH as the carrier of the spectrum already demonstrated strong temperature dependence of the 2PP peak position and with associated with the t_{2g} - e_g transition.

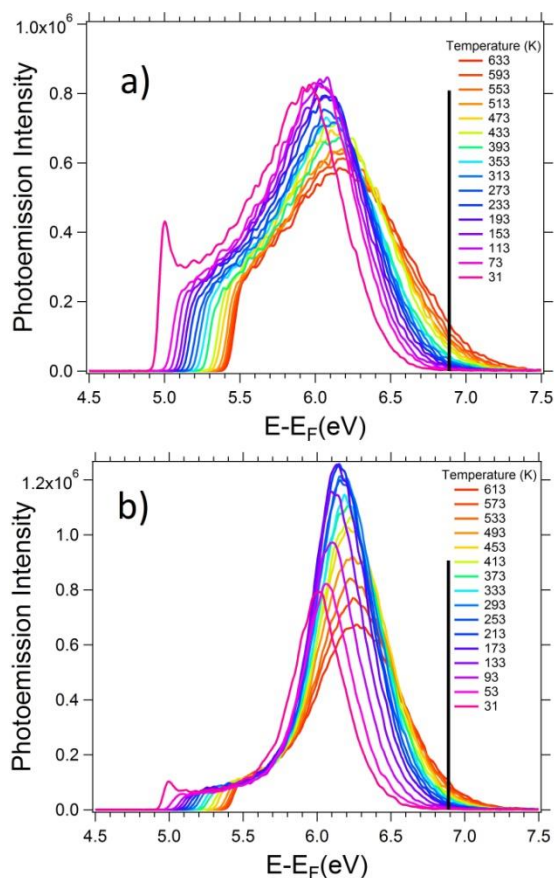


Figure 5.2- Temperature dependent line profiles for (a) p-polarized and (b) s-polarized light, with the sample oriented along the [001] direction for 360 nm light. The black vertical line corresponds to the expected two photon Fermi edge. As the Temperature decreases the peak shifts to lower energy and the linewidth sharpens; moreover, the DOS at the Fermi level decreases.

Figure 5.2 shows the change in 2PP spectra for 3.44 eV (360 nm) excitation with the [001] axis in the optical plane as the sample is cooled from 633 to 31 K. The spectra obtained with s- and p-polarizations undergo systematic changes, some of which can be attributed explicitly to the sample temperature. The

spectra also show a gradual decrease of the work function, which is due to adsorption of impurity molecules during the course of the experiments, which can take up to two hours, rather than more pertinent effects related to the e-p interaction. Below ~ 500 K dissociative chemisorption of H_2O at the bridging O atom vacancy sites is expected to produce the bridging OH species, and below 300 K H_2O begins to adsorb molecularly onto the surface. Although I use the specific example of H_2O , the true identity of impurity molecules is not known. The effect of the molecular adsorption can be reversed by flashing the spectra to desorb the contamination without affecting other temperature dependent features of the spectra (Figure 5.3). Therefore, the small amount of molecular adsorption during these measurements does not introduce extraneous spectroscopic features that would compromise the following analysis.

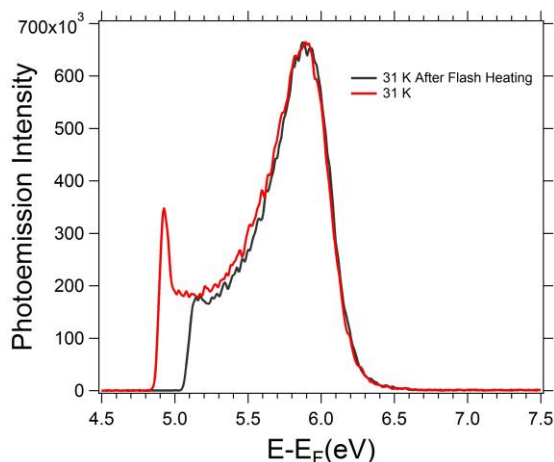


Figure 5.3- Adsorbate covered and clean surfaces probed at 380 nm at 31 K with the sample aligned to the [001] direction. The change in the work function due to contaminate adsorption has no effect on the peak position or the Fermi edge.

The other effects of the changing temperature can be then assigned to the temperature change and not the additional adsorption of molecules. First I observe that the position of the d-d transition peak resonance is changing in both energy and width. Along with this change in the resonance peak, there is also a change in the spectral density at the Fermi level, which is in the far wings of the peak. The black vertical line in figure 5.2 shows the expected Fermi level for 2PP on a clean TiO_2 surface, which is based on the two-phonon energy of the excitation. At high temperatures the spectral density actually extends above the E_F , while at low temperatures goes to zero at E_F . Since I ruled out the affect of adsorbed molecules as the cause of these spectral changes, instead I assign them to the polaron spectral density

that results from localization as well as electron-phonon interaction. As the temperature decreases the polaron becomes more localized and strongly bound. Consequently, the density at E_F decreases. This manifests itself in Figure 5.4 as a shift of the defect state energy to a larger binding energy below E_F , the narrowing of the peak, and reduction of DOS at E_F . As the temperature of the sample increases, the lattice experiences thermal expansion, and occupation of the acoustic and optical electron-phonon modes increases. These changes weaken the polaron confinement and consequently its energy shifts towards E_F and its profile broadens.

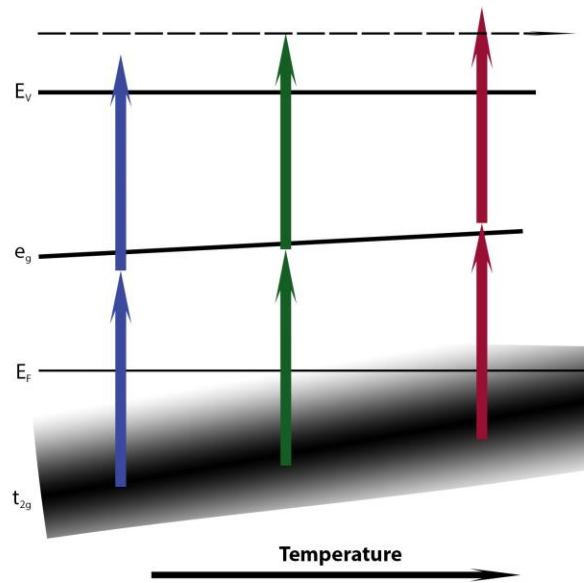


Figure 5.4- Energy level diagram for 2PP in our experiment. As the temperature changes the initial states and intermediate states shift in energy at different rates and the polaron linewidth broadens.

The characteristics of the t_{2g} - e_g peak shift in Figure 5.2 can be elaborated by determining how the resonance energy depends on the sample temperature. The change in the resonance energy with temperature can be obtained by measuring how 2PP resonance enhancement depends on the photon energy at different temperatures. The resonant 2PP process occurs when the excitation wavelength exactly matches the energy difference between the maximum DOS of the initial states and the intermediate e_g state, as suggested by the green arrows in figure 5.4. A measurement of the resonance energy at 300 K is illustrated in figure 5.5, where the green curve defines the resonant photon energy.

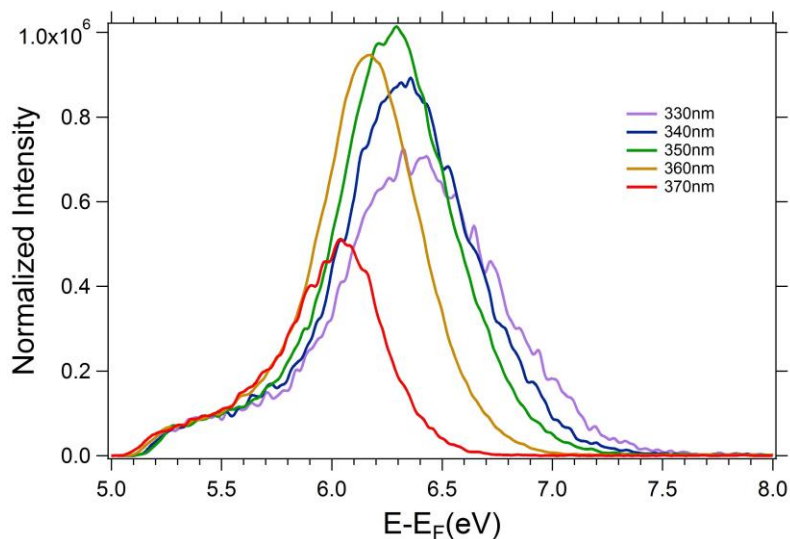


Figure 5.5- Resonance determination at 300 K for the sample aligned long the [1-10] axis with p-polarized light. The resonance occurs between 3.44-3.54 eV (350-360 nm) at this temperature.

By performing wavelength dependent 2PP measurements at different energies I can map out how the resonance energy depends on temperature. Taking the data such as in figure 5.5 at various temperatures I fit the peak intensity vs photon energy to a Gaussian to determine the exact wavelength the resonance appears at for a given temperature. This data is then plotted in figure 5.6 as the resonance energy vs temperature to show how it changes as the sample is cooled.

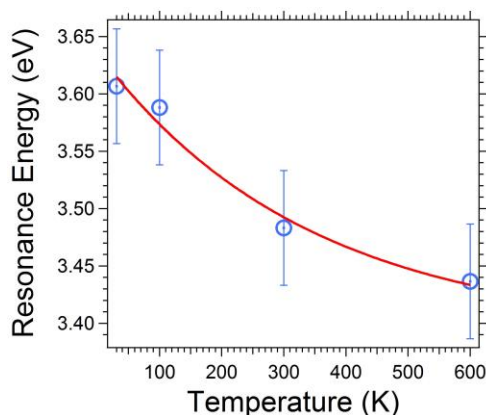


Figure 5.6- Fitted resonance energy vs temperature for the high energy d-d transition peak, extracted from fitting the data such as in figure 5.4 for multiple temperatures.

Figure 5.6 shows that the resonance energy decreases from 3.61 eV at 31 K to 3.44 eV at 600K. There are three possible explanations for the changing resonance energy. The t_{2g} position could be changing, the e_g position could be changing or both d-bands could be changing, but at different rates. In order to

determine which of these possible scenarios is occurring an additional piece of data is needed namely the energy of the intermediate (e_g) state. This can be extracted from the same data set by plotting the intermediate state energy vs photon energy for each of the sample temperatures, as shown in figure 5.7.

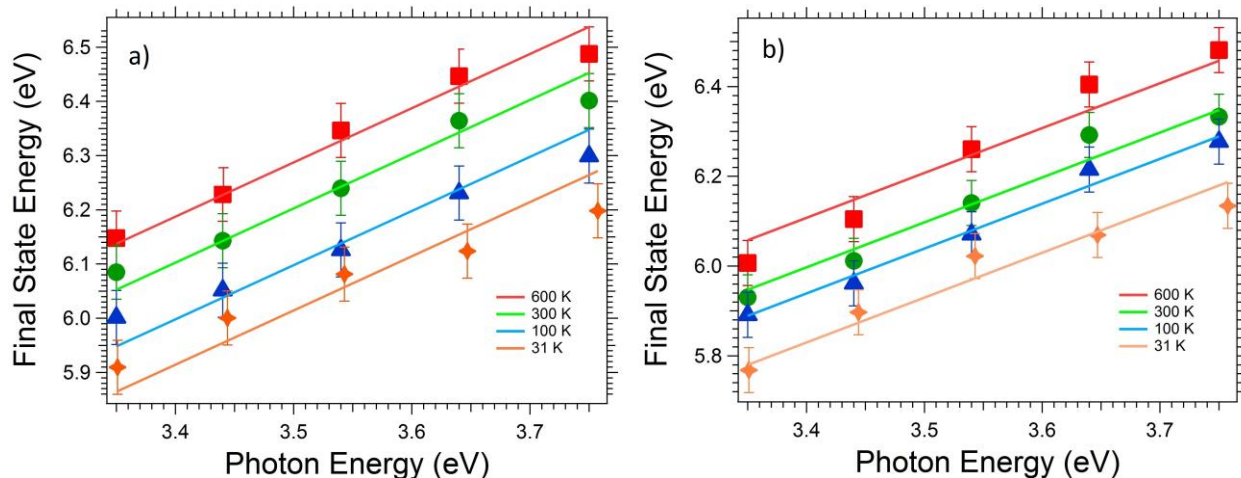


Figure 5.7- Wavelength dependent measurements for 600, 300, 100, and 31 K showing the position of the final state energy at which the e_g state is observed vs photon energy. The intermediate state position decreases with temperature. A slope of 1 is fixed at all temperatures. The intercept of each plot gives the e_g state energy relative to E_F . a) p-polarized spectra and b) s-polarized for the [001] aligned sample.

From this data it is evident that the e_g state energy increases with temperature for both orientations of the sample. However the rate at which the intermediate state energy is changing is not the same as the rate that the resonance energy is changing, thus the initial states (t_{2g} states) must also be shifting in energy. By taking the intermediate state energy and subtracting the resonance energy I obtain the position of the initial state as a function of temperature, as shown in figure 5.8.

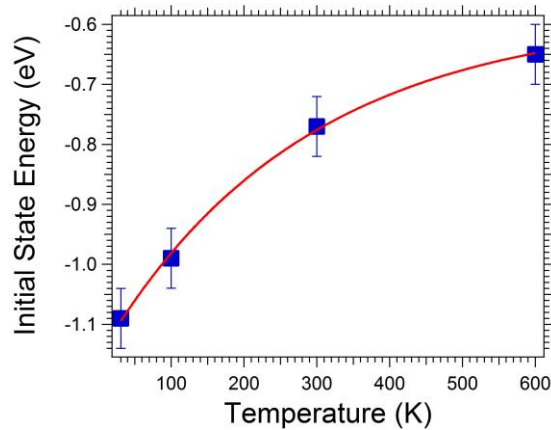


Figure 5.8- Maximum spectral density of the initial state (t_{2g}) vs. temperature. The maximum shifts from 0.6 eV below the Fermi level at 600 K down to 1.1 eV below the Fermi level at 31 K.

The results in figures 5.7 and 5.8 are plotted together in figure 5.9. Comparing how the two d-band energies shift with temperature helps to interpret the data in figure 5.6. As seen in figure 5.9 the t_{2g} and e_g states change in energy at different rates, which can be explained by the crystal field affecting them differently. The reduction of the t_{2g} - e_g resonance energy with temperature thus is a consequence of the much stronger destabilization of the t_{2g} initial polaronic state than the intermediate e_g state. These distinct changes in the d-band energies can be due to several different effects. The temperature dependent electron-phonon interaction should be able to account for the changes, particularly when looking at high temperature, but additional physics are needed to account for the accelerating change at low temperatures. In the simple picture of the polaron the energy decreases linearly with temperature as the electron localizes more strongly on a lattice site. At low temperatures the LO phonons begin to freeze out, causing the polaron energy to saturate at a minimum value as it can no longer hop between lattice sites. However this simple behavior is not what is observed in my experiments. Below 100 K the rate of change increases instead of saturating, indicating an additional effect must be driving the shift in energy. Low temperature measurements on the TiO_2 surface have shown the formation of a small polaron to be stable at temperatures of ~ 20 K, and capable of inducing ferromagnetic effects showing the potential importance of the polaron on the surface. [225]

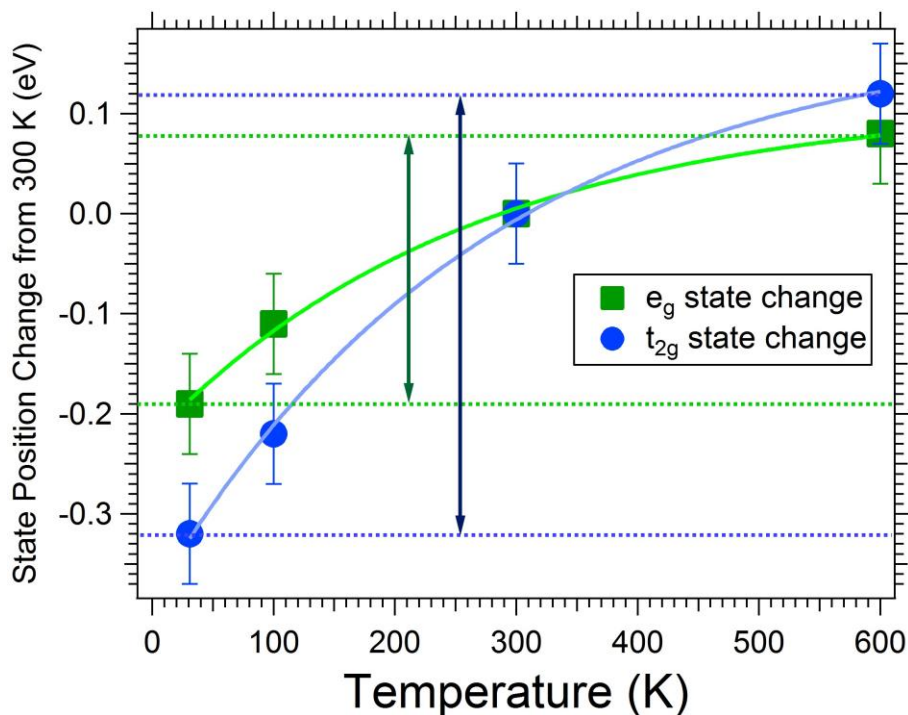


Figure 5.9- Combining the previous data yields the final picture showing the change of the e_g and t_{2g} states with temperature from their reference positions at 300 K.

Recently, several low temperature STM studies have measured the defect density of states of the TiO_2 surface and its origin. The injection of charge into the surface via oxygen desorption has been found to increase the defect state DOS, which is indicative of more charge localization and formation of polarons. Additionally it was found that while oxygen desorption can increase the amount of charge, sub-surface oxygen vacancies and interstitial Ti atoms also inject charge, which localizes around Ti^{3+} atoms.[34,205] Another study attempted to probe the TiO_2 polaron more directly using an STM to interact with the excess electrons. They observed a changing localization of electrons with temperature, becoming more asymmetric with decreasing temperature, and concluded that this must be due to the polaronic nature of the electrons in TiO_2 . By cooling the sample to below 78 K they were able to trap the electrons and manipulate them via the STM tip. At temperatures below 16 K they observe these electrons localize further and become trapped at certain lattice sites displaying a multi-lobed structure.[226] This behavior is similar to the change of the t_{2g} defect state energy with temperature in the fact that below 100 K, I observe a change in the behavior of the localized electrons. The observed asymmetric localization and multiple lobe structures they observe may be important for describing the additional effects seen in my experiments that cannot be described by simple theory.[226,266,267]

In order to interpret the experimental data on how electron-phonon interaction affects the 2PP spectra of the d-d transition, I collaborated with Dr. Honghui Shang at Fritz Haber Institute. First, the small polaron structure and energy was calculated by inserting an excess electron into the TiO₂ lattice and performing a calculation on lattice and electronic structure of bulk TiO₂. The calculation was carried out by using a 3x3x4 super cell (216 atoms), and calculated with HSE06 range-separated hybrid functional. The results after lattice relaxation are shown in figure 5.10 with the excess electron localizing around a Ti atom in a d like orbital ~ 1.0 eV below the Fermi level. This is consistent with previous calculations and consistent with the polaron being in the t_{2g} defect states. [220,223,268] Note, however, that defects and their interactions with polarons is not included in this calculation.

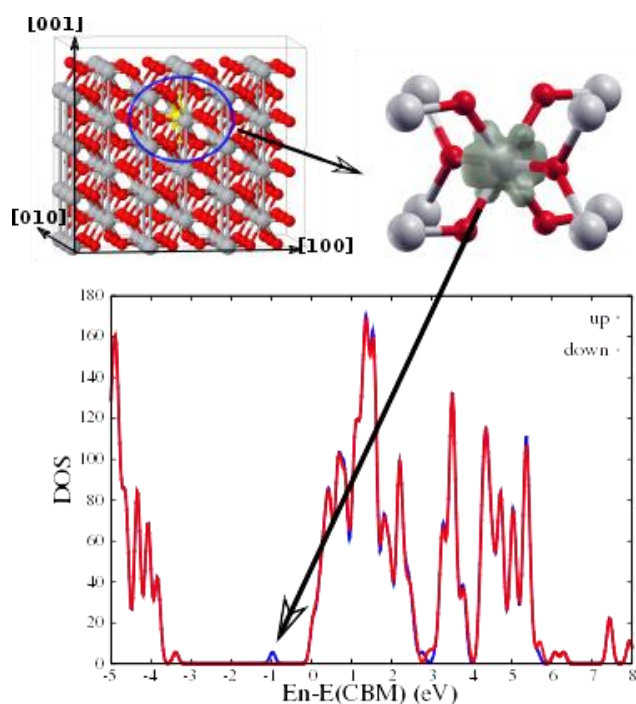


Figure 5.10- Structure and charge density of a small polaron in r-TiO₂. Large (grey) balls represent Ti, small (red) balls O. The polaron state is localized at Ti-3d orbital, 1.0 eV below CBM.

In order to describe the temperature dependent data a first principle calculation based on the theory of Allen, Heine, and Cardona (AHC) is used, which includes the calculation of band structure renormalization and temperature dependence due to electron-phonon coupling.[227,269-271] A primitive cell and LDA functional are used for the calculation, using a 4x4x6 grid of q-points. Upon optimization a primitive cell with lattice constants of $a = 4.549$ and $c = 2.919$ is obtained, consistent with previous calculations. The calculated temperature dependent changes in the t_{2g} and e_g energies are

shown in figure 5.11. The theory qualitatively reproduces the stronger temperature dependence of the t_{2g} energy, as compared with the e_g energy. This is consistent with the temperature dependent occupation of the phonon states via a Debye-Waller type electron phonon interaction. However, the calculated value of the change is underestimated by half and the low temperature behavior is not reproduced.

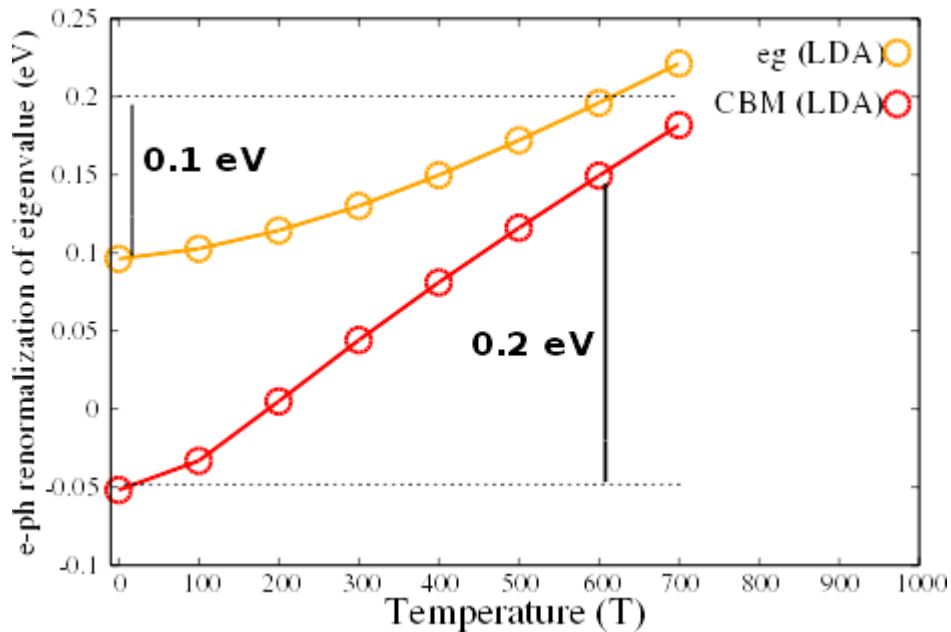


Figure 5.11- Theoretical temperature dependence of the e_g and CBM state using AHC theory calculations.

Again looking at figure 5.11 it can be seen that using electron-phonon temperature dependence does not reproduce the accelerating change in the energy levels below 100 K. This failure to reproduce both the magnitude and the curvature of the experiments suggests that there is some additional physics that is not yet understood. It may be that the inclusion of polarons and defects in the calculations will resolve this discrepancy but higher order interactions such as bipolarons at low temperatures, may also be important. A bipolaron is the coupling of two polarons in the lattice to form a larger overall structure. To see why this might be important we can look at recent theory that postulates that high temperature superconductivity may be due to bipolaron formation in a variety of materials, including metal-ammonia solutions.[272] This rapid change in material properties at low temperature is consistent with the experimental data in my experiments.[240,272,273] Additionally recent calculations on TiO_2 also predict the formation of a bipolaron due to oxygen vacancies on the surface. [263,267,274] Continuing research is needed in this area to finalize the assignment of the observed temperature induced changes to the d-bands. As of the writing of this chapter, additional calculations that include the temperature dependent

lattice effects have been able to account for some of the discrepancy and give an accurate energy difference between the e_g and t_{2g} states. However, the overall location of these bands is still underestimated by ~ 0.2 eV and the curvature is still inadequately reproduced.

5.4: Conclusion

Temperature dependent two photon photoemission was performed using an ultrafast (~ 20 fs) laser with 330-380 nm excitation energy on the clean TiO_2 surface. A shift in the t_{2g} to e_g transition as well as a broadening of the energy to above the Fermi edge was observed with changing temperature from 600 K down to 31 K. The shift in energy is assigned to the localization of charge on Ti^{3+} sites with decreasing temperature. This localization is described by a quasiparticle called a polaron which is the interaction of the localized charge with the surrounding lattice. [235,236]

Temperature and wavelength dependent measurements were carried out over a broad range in order to determine the shift in energy and position of the t_{2g} and e_g states. By comparing the resonance positions at different wavelength and temperatures the shift in the initial and intermediate state energies were revealed. At high temperatures the movement closely follows the predicted electron-phonon temperature dependence given by a Debye-Waller like interaction. This is confirmed by first principle calculations of the electron-phonon interaction. At low temperatures additional physics is needed to describe the accelerating shift in the energy change. This shift is not well described by current theory and needs additional explanation for a full description. Higher order effects such as bipolarons must be considered. The increased understanding of polarons in TiO_2 is important for improving photocatalytic and photovoltaic devices as it pertains to charge transport and temperature dependent effects on these processes. This work helps shed light on these interactions and advances the previously disputed understanding of polarons in TiO_2 .

6. Chapter Six: Multi-Photon Photoemission from Adsorbate Covered TiO₂

6.1: Introduction

The study of photocatalysis TiO₂ has been ongoing for many years, however only recently has our technology reached a point where we can begin to probe dynamical processes induced by band gap excitation at molecule decorated surfaces.[5,16,275] TiO₂ has been of interest for photocatalysis due to its chemical activity upon band gap excitation. From the photocatalytic splitting of water, dissociation of organic molecules in the so-called self-cleaning glass, to more recent experiments in carbon dioxide (CO₂) capture and remediation to reduce greenhouse gasses, TiO₂ has found many potential applications.[3,53,276-283] By improving our understanding of how photoexcited carriers drive these reactions, we can overcome their relatively low efficiency to produce better materials with activity in the visible spectrum. Here I present a study on the effects of adsorbates on the previously reported t_{2g} to e_g transition on the TiO₂ surface.[84,284] The effects that adsorbates have on this transition can be important in understanding the origin of photocatalytic processes and how the molecules interact with the TiO₂ surface to modify its physical and chemical properties. I present findings for methanol (CH₃OH), which has been investigated in the past with respect to the wet electron states on the TiO₂ surface, as well as CO₂ and O₂. [59,70-72,262,285,286] The interaction with these three different adsorbates is markedly different, with each molecule having a different interaction with the surface that substantially impacts the d-d transition. The effects are all highly coverage and temperature dependent, with drastic changes happening in a small temperature or coverage ranges. These changes provide important information on how adsorbates change the surface electronic structure with potential implications for photocatalysis.

6.2: Experimental Details

Sample preparation, heating, and cooling are all done via the same processes as discussed in the previous experimental chapters. The clean surface is prepared in an identical way and then molecular dosing is done at various temperatures and flow rates. The dosing is accomplished as described in chapter 3 with a leak valve connected to a long tube allowing the molecules to be dosed directly onto

the sample surface. This allows for precise dosing at a given temperature, producing the exact amount of coverage desired.

6.3: Results and Discussion

6.3.1. 2PP spectroscopy of CH₃OH/TiO₂

Past experiments with 3.1 eV excitation focused on the formation of the wet electron state on the water or methanol covered TiO₂ surface.[63,70,72,262,287-289] Under such excitation conditions the only spectral feature that appeared in 2PP spectra was due to resonant excitation from the Ti-3d defect states to the wet electron state at the methanol/vacuum interface. In the photocatalysis literature, the liquid methanol/TiO₂ interface has been studied extensively in the past due to its ability to scavenge holes on the TiO₂ surface, which can be used to enhance the photocatalytic splitting of water.[290,291] Methanol has also been reported to dissociate under UHV conditions at sub-monolayer coverage under band gap excitation of single crystal TiO₂(110) surface.[64,66,292,293] Additionally the simple structure of CH₃OH compared to more complex organic molecules allows us to study the dynamics and changes it has on the TiO₂ surface and relate those changes to the reduction of more complex organic molecules.[4,294] By using our systems unique ability to probe over a wide range of wavelengths as well as orient the sample as desired, we are able to probe the adsorption, desorption and chemistry on the surface in a much more sensitive and revealing manner than the previous photoemission studies.

Previous studies have looked at methanol temperature programmed desorption (TPD) and have found that multilayer desorption of CH₃OH occurs at ~150 K.[295] Additional TPD peaks occur at 165 K, 295 K, 350 K, and 480 K, corresponding to various species and adsorption sites on the surface. The primary desorption peaks from the first monolayer are at 295 K and 350 K and indicating that methanol is present on TiO₂ surface even at room temperature.[296] Comparing the TPD results to the work function change, I can estimate the approximate coverage of methanol on the surface. At ~200 K the desorption of the first monolayer begins, with about half a monolayer remaining at the primary desorption peak of 295 K.[295] The temperature where the first monolayer begins to desorb corresponds to a work function of ~3.9 eV. Adsorption of second and higher layers causes further reduction of the work function. Additionally previous measurements have found that exposure of about 1.2 Langmuir's (L) methanol corresponds to 1 ML coverage.[70,72] The typical total dosage of methanol

onto my surface is ~ 4 L, and combining this information with the work function change I can estimate that in typical experiments I stop deposition at ~ 3 ML coverage.

Because methanol desorbs from TiO_2 surface above room temperature, the experiments are carried out at 80 K. The 2PP measurements are performed with 350-370 nm excitation with the sample oriented such that the optical plane bisects the $[001]$ and $[1\bar{1}0]$ directions unless otherwise noted. This causes both p and s polarized light to excite t_{2g} to e_g transition equally on the clean TiO_2 surface, allowing us to discern any features caused by dosing of methanol onto the surface. This configuration was already reported in chapter 4 of this work, where it was used to distinguish between the wet electron and e_g intermediate states in 2PP process from the t_{2g} initial defect state.[192,284] At low coverages the wet electron and e_g states provide competing excitation channels, with nearly equal probability, but as the coverage is increased to a multilayer range, methanol adsorption quenches the t_{2g} to e_g transition as well as the wet electron state. As shown in Figure 6.1, a CH_3OH covered surface at 80 K shows both the wet electron and t_{2g} to e_g transition are present, immediately ruling out that they are the same transition as claimed in Ref. [192].

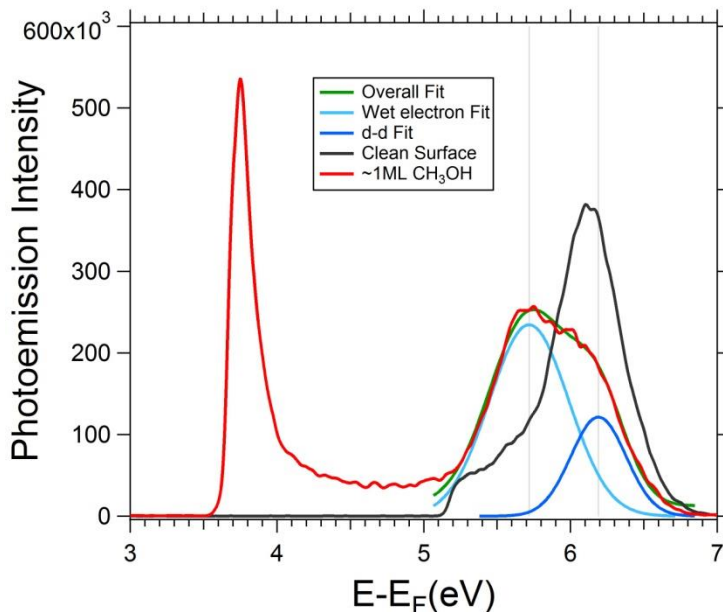


Figure 6.1- $\sim 1\text{ML}$ coverage of CH_3OH on the TiO_2 surface at 80 K. At this moderate coverage, there are clearly two close but separate peaks on the surface. The lower energy peak (2.3 eV above E_F) is the wet electron state while the higher energy (2.7 eV above E_F) is the t_{2g} to e_g transition. The spectra are measured with p-polarized 350 nm light.

As can be seen in Figure 6.1, the adsorption of CH₃OH reduces the 2PP intensity of the t_{2g} to e_g transition as compared to the clean surface. How the d-d transition is quenched with CH₃OH deposition is reported in Figure 6.2 for s-polarized excitation. The wet electron state is only visible for p-polarized excitation so s-polarized light is utilized to remove competing contribution by the wet electron state. The quenching proceeds gradually with increasing coverage until the transition is completely suppressed when a 2.5 ML coverage of CH₃OH is deposited on the surface. Concomitant with the d-d transition quenching, the progressive adsorption of CH₃OH decreases the work function. A decrease in the work function is expected if the dipoles of adsorbed molecules point with their negative end towards the surface; this reduces the energy required to transport electrons through the dipole layer into the vacuum. It is also consistent with charge transfer from methanol to TiO₂, which is predicted by theory, but does not seem to have spectroscopic consequences beyond the change in the work function. [70,297]

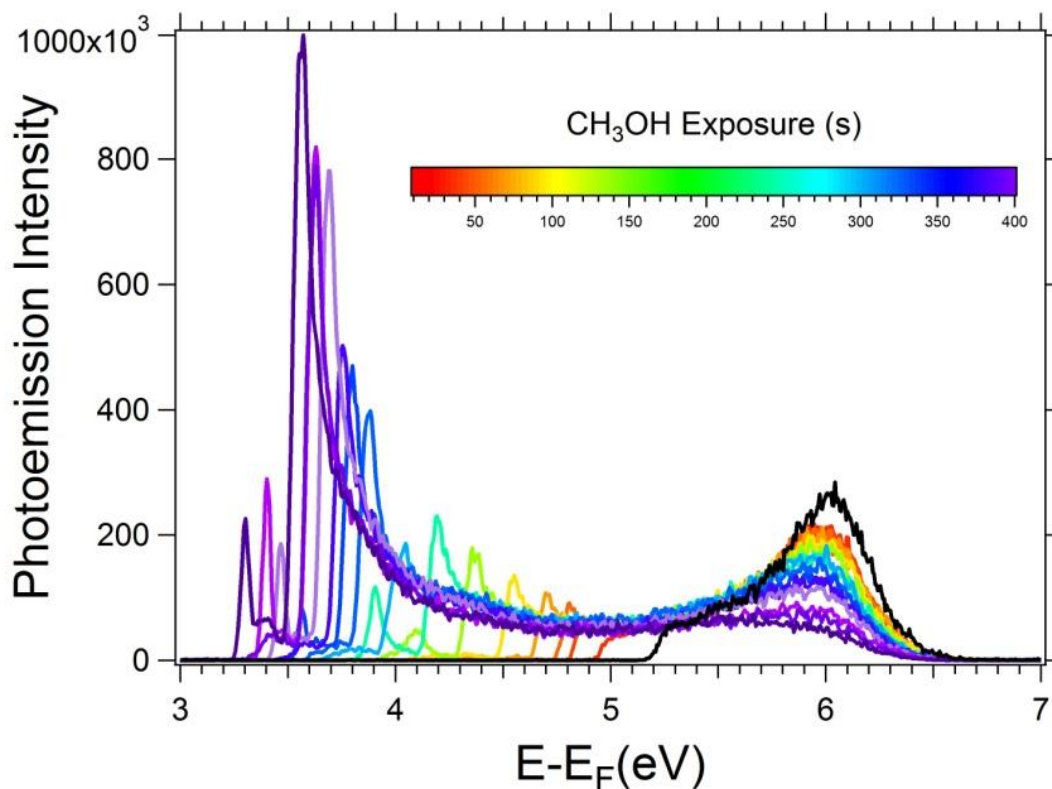


Figure 6.2- The CH₃OH coverage dependence of the d-d transition in 2PP spectra of TiO₂ surface with 370 nm, s-polarized excitation. Increasing coverage of CH₃OH on the surface quenches the d-d transition and reduces the work function. The black line indicates the 2PP spectrum of the clean TiO₂ surface.

As methanol is deposited onto the surface at ~80 K, it does not have enough thermal energy to reorganize into a thermodynamically stable crystalline form. Rather it forms an amorphous structure

where the O atoms of CH₃OH in the first monolayer interact preferentially with the undercoordinated Ti atoms of the substrate, and the subsequent layer contributes to the dipolar field of the first layer by making a hydrogen bond with OH of methanol to the bridging O atoms of the substrate.[297,298] The deposited structure has a strong interaction with the surface causing a quenching of the d-d transition peak, but the mechanism is not immediately obvious. The d-d transition intensity, however, can be recovered abruptly by heating the sample to 120 K, as shown in Figure 6.3a. This temperature is too low for methanol at a multilayer coverage to desorb from the surface. The change in the spectra occur all at once in a narrow temperature range near 120 K, and upon further heating to 145 K, the spectra remain unchanged indicating that there is no significant thermal desorption of CH₃OH.[299-301] 2PP spectra recorded with p-polarized light in Figure 6.3b show that the same intensity jump occurs for the wet electron state at ~120 K.

The effects of thermal desorption on 2PP spectra can be seen in Figure 6.4 for a series taken from 140 to 290 K. With s-polarization, the dominant resonant d-d contribution recovers slightly as the temperature is increased to 290 K. The main effect of sample warming in Figure 6.4a is to increase the sample work function due to CH₃OH desorption. The same change is observed in Figure 6.4b for p-polarization, but in addition, the dominant t_{2g}-wet electron resonance disappears as CH₃OH desorbs. The t_{2g}-wet electron resonance in p-polarized spectra causes the resonance peak to shift to higher energy as CH₃OH is desorbed and the wet electron acceptor state is no longer available. The s-polarized spectra show no such shift in the same temperature range because of their pure t_{2g}-e_g origin. Thus, the spectral changes for heating the CH₃OH/TiO₂ surface above 140 K can be attributed to CH₃OH desorption.

Instead of heating above 140 K, it is also instructive to heat the CH₃OH/TiO₂ surface from 80 to 140 K, thereby recovering the t_{2g}-e_g transition, and then recooling it again to 80 K through the 120 K transition temperature. This procedure tellingly does not reverse the spectral changes indicating that whatever caused the spectra to reappear at 120 K is not a thermally reversible process. Thus, the observations are consistent with the removal of the Ti-3d defect DOS that is the initial state for both the t_{2g}-e_g and t_{2g}-wet electron transitions. We note that some of the initial DOS is never removed, so the 2PP spectra have contributions from DOS that is not affected by methanol adsorption.

Based on these observations, we postulate that the discontinuous and irreversible change in the t_{2g}-e_g and t_{2g}-wet electron transitions at 120 K occurs on account of an amorphous-to-crystalline phase transition in the methanol overlayer. Mathiessen et al. reported that such transition occurs for a CH₃OH film on Pt(111) substrate at 115 K based on rare gas diffusion experiments.[298] The slightly higher

temperature in our measurements may reflect the fact that we use a different observable, the substrate might have a modest effect on the transition temperature, or differences in the temperature calibrations.

I propose this scenario. The initial deposition of CH₃OH is dominated by the CH₃OH-TiO₂ interactions, which locks the first monolayer in structure where the dipoles are aligned with the negative charges pointing into the surface. The second CH₃OH layer cannot make bond optimally with the exposed CH₃ groups of the first layer molecules. Rather, it is known to make weak hydrogen bonds with the bridging O atoms of the substrate, again presenting the weakly interacting CH₃ groups to the subsequent layers.[302] Thus, the first two CH₃OH layers are ordered by the substrate and have unfavorable interactions with subsequent layers. The ordering of the dipoles gives the film a ferroelectric character, which presents a strong field to the substrate. The substrate responds by screening the dipole field through a depolarization field.[303] In other words, the itinerant Ti-3d electrons are repelled from the surface by the dipole field of the adsorbates, thereby removing the initial states for the t_{2g} - e_g and t_{2g} -wet electron transitions from the surface region. The CH₃OH film, however, is in a metastable amorphous state not being able to optimize the bonding of CH₃OH crystalline state. Heating the substrate to 120 K provides the thermal energy, which enables CH₃OH molecules to undergo the amorphous-crystalline phase transition, and thereby quench the ferroelectric ordering reorienting the surface dipoles. This decoupling of the dipoles from the substrate is thermodynamically irreversible, and it allows the Ti-3d electrons to return to the surface region, where they can be detected spectroscopically by 2PP.

The above scenario is consistent with CH₃OH being a hole scavenger. The formation of a surface dipole field repels the substrate electrons and attracts the holes. Therefore, at CH₃OH covered surfaces, electrons are repelled from the surface and holes are attracted where they can interact with adsorbed molecules to induce photocatalytic reactions. An added benefit of the dipole field is that the charge separation slows down electron hole recombination. A similar scenario for surface dipole-induced hole interactions has recently been proposed by Shirai et al. in a hole trapping study of H₂O covered anatase TiO₂ nanoparticles.[304]

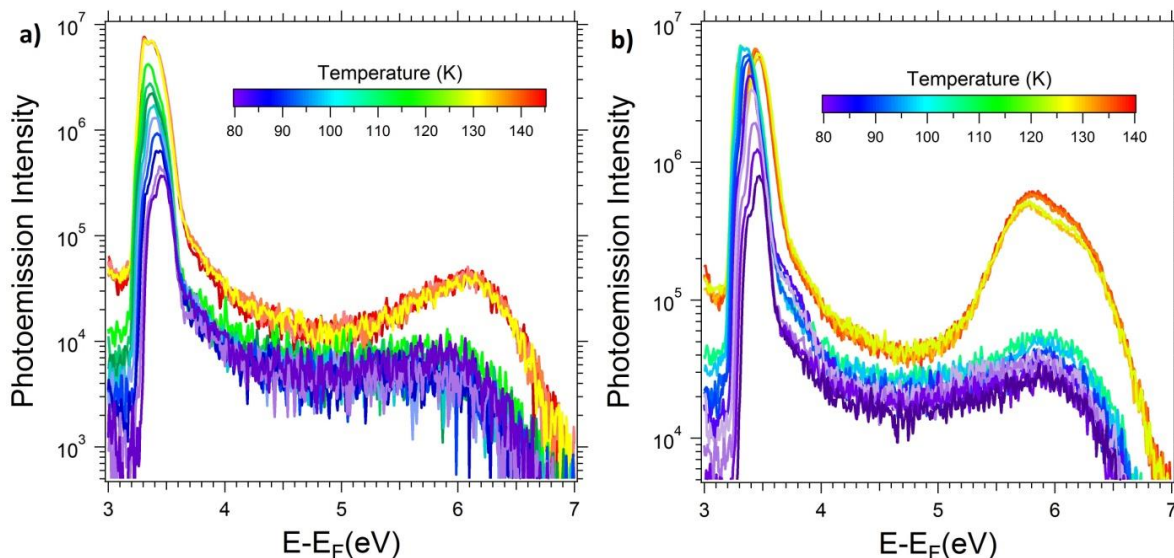


Figure 6.3-a) s-polarized spectra at 350 nm for the warming of the CH₃OH covered sample. At high coverage the work function is low enough to allow for 1 photon photoemission, requiring a log scale to see the d-d transition. Below 120 K the transition is quenched, but heating above 120 K shows a sudden recovery of the d-d transition peak, strongly indicating a change in the structure of the CH₃OH at that temperature. b) p-polarized spectra shows both the wet electron and d-d transitions turning back on after the CH₃OH phase transition.

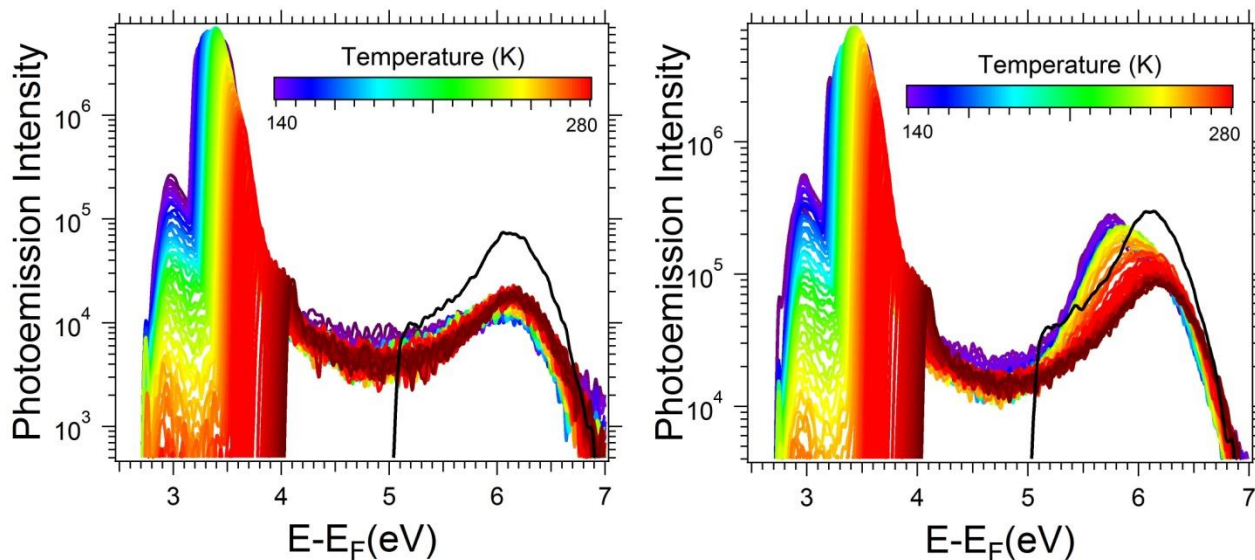


Figure 6.4- CH₃OH covered surface warmed from 124 K to 280 K measuring every 2 K with 350 nm excitation. a) s-polarized spectra show hardly any change from 120 K to the surface at 300 K, the peak being unaffected. b) p-polarized spectra show a decrease in the wet electron state intensity as the methanol coverage decreases below 1 ML. Log scale used for photoemission intensity due to presence of 1PPE on the surface due to low work function energy. Black curve gives the spectra at 300 K after sample preparation but before any CH₃OH is dosed.

I have also investigated the effect of CH₃OH adsorption at high (>293K) temperature, where CH₃OH cannot adsorb in the molecular form. CH₃OH can only be present on such surfaces as a dissociation

product at O atom vacancy sites, where dissociation produces OH and CH₃ on the bridging O atom rows. At high temperatures, two bridging OH can recombine to form H₂O and desorb from the surface at 490 K. The fate of CH₃ is more complicated, since C-H bonds can break to form more bridging OH, or CH₃ and its products can recombine to desorb as some form of C₂H_{2n} molecules.

In these experiments the sample is heated up to 900 K, and 2PP spectra are measured from 700 K to lower temperatures. The surface is exposed to CH₃OH when it reaches 523 K. Figure 6.5 shows the high temperature dependence of the sample. As the sample is cooled from 700 K, the 2PP spectra are characteristic of the clean surface with no adsorbates, including OH. At this temperature the d-d transition is still detected but with reduced intensity because the 360 nm excitation is above the resonant t_{2g}-e_g transition, as discussed in detail in chapter 5. As the sample cools to 523 K the transition moves closer to resonance and resonance sharpens causing its intensity to increase, but there is no evidence of molecular adsorption. When the sample is exposed to CH₃OH at 523 K, there is a jump in the d-d transition intensity and the work function decreases by 0.4 eV, as expected for molecular adsorption. The increase in the d-d peak intensity can be attributed to H and CH₃ on the bridging O atom rows being electron donors to the Ti-3d orbitals of the undercoordinated Ti atoms at the surface.[305] The contribution from dissociated CH₃OH, however, immediately saturates when all of the O atom vacancy defect sites have undergone a reaction leading to a relatively constant intensity from 473-373 K. Below 373 K, the sample can support additional species of methanol, which now cause the d-d transition intensity and the work function [306] to decrease and the resonance peak to shift to the wet electron energy. These changes are characteristic of CH₃OH adsorption at the undercoordinated surface Ti atoms, which is responsible for the low temperature behavior such as in Figure 6.3. This is accompanied by a sharp decrease in the work function.

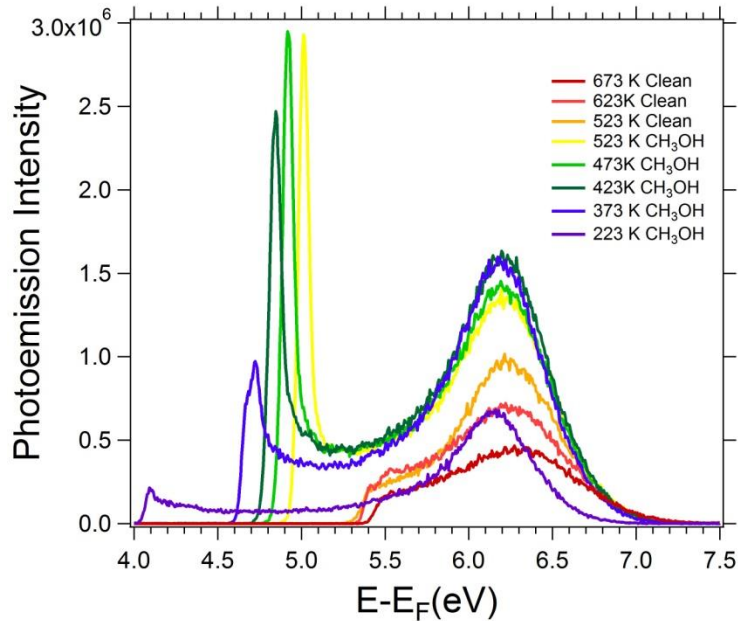


Figure 6.5- High temperature dosing of CH₃OH on clean TiO₂. At high temperature CH₃OH dissociates so that OH and CH₃ are deposited on the bridging O atom rows on the surface. As the sample cools below room temperature CH₃OH begins to deposit, sharply decreasing the d-d transition intensity. The excitation is with 360 nm p-polarized light with the [110] axis aligned in the optical plane.

By performing spectroscopic measurements on the methanol covered TiO₂ surface I was able to examine the change in the electronic transitions on the surface due to increasing coverage at various temperatures. I found that the ability to excite the d band transitions on the surface of TiO₂ is sensitive to the structure of the adsorbed molecules on the surface and can thus be controlled by cooling and heating the sample to specific temperatures. Additionally I found that this system can support the excitation of both the d-d transitions as well as the wet electron state transition simultaneously, further clarifying previous misconceptions about this system. Finally I studied the increased intensity due to the adsorption of OH and CH₃ on the surface at high temperature and speculated that the increase in the d-d transition strength is caused by charge transfer from these adsorbates to the TiO₂ substrate.

The 2PP studies of CH₃OH/TiO₂ surface in the 80-673 K temperature range unequivocally show that the near surface Ti-3d defect density depends on molecular adsorption. Electron donating molecules such as CH₃OH have a repulsive interaction with electrons occupying the defect states, and by extension to the CB electrons. Thus, because the molecule-induced interfacial fields attract holes and repel electrons, this in part explains why under photocatalytic conditions TiO₂ surfaces with CH₃OH or H₂O are efficient hole scavengers. These studies, therefore, demonstrate how 2PP spectroscopy of CH₃OH/TiO₂ surface can provide important information on carrier dynamics of relevance to photocatalysis.

6.3.2 2PP spectroscopy of CO₂/TiO₂

The adsorption of CH₃OH on TiO₂ demonstrated how an ostensibly charge donor can paradoxically suppress the 2PP signal from the defect charge that occupies the conduction band orbitals. Next, I dosed CO₂ onto the TiO₂ surface, which has amphoteric properties, that is its O atoms are charge donors, and C atom is a charge acceptor.

CO₂ capture, storage, and transformation into useful chemical feedstocks is an important issue for the environment. By studying the adsorption of CO₂ on the TiO₂ surface I hope to determine the photoinduced dynamics and to further our understanding of how to improve methods of photocatalysis on this and similar surfaces. In these experiments the TiO₂ surface is aligned to the [001] direction unless otherwise noted due to the lack of any polarization dependent differences. It has been shown in previous studies that UV irradiation CO₂ covered TiO₂ surfaces can reduce CO₂ into hydrocarbons such as CH₄. [279,307] Additional studies have looked at the adsorption of CO₂ under different pressure, temperature, and coverage conditions. [60,62,278,308] Acharya et al. conducted a low temperature STM study of the CO₂ covered surface and looked at the adsorption and desorption from different sites. They found that CO₂ preferentially adsorbs onto the oxygen vacancy sites but also can adsorb in multiple configurations on the undercoordinated Ti sites. As CO₂ is adsorbed from the gas phase, it initially scatters on the surface until it loses thermal energy. This initial motion on the surface enables it to find favorable adsorption sites such as the undercoordinated Ti or oxygen vacancy sites. These two adsorption centers behave differently with an activation barrier separating them and preventing an adsorbed CO₂ molecule from switching sites. Additionally they found that at a tip bias of 2 V or more the CO₂ could be selectively dissociated via tunneling electrons. Injecting an electron into the unoccupied orbitals of CO₂ adsorbed at bridging oxygen vacancies sites can cause its dissociation thereby healing the vacancy and causing the CO molecule fragment to desorb. This has important implications for photocatalysis since it shows that non thermal methods can be used to induce CO₂ reduction on the surface. It is therefore possible that sufficiently energetic photons could also induce a similar reaction and give rise to a favorable photocatalytic effect. Finally, coadsorption of CO₂ with other molecules on the TiO₂ surface has been studied to see how different photocatalytic processes can interact to alter the chemistry. [61,309-311] The goal of my study is to advance the understanding of CO₂ adsorption and electronic structure on TiO₂ surface by use the same methods as for methanol covered surfaces. The primary information obtained concerns the interaction of CO₂ with the Ti-3d defect states and the potential photoinduced formation of CO₂⁻, which is a precursor to CO₂ reduction. Due to the negative vertical electron affinity of CO₂ in the gas phase, it is necessary first to reduce the adsorbed molecule to

a CO_2^- species.[312,313] CO_2 is normally fairly inert with a linear bond structure which converts to a much more reactive bent structure upon a charge transfer to CO_2^- . [314] CO_2 interaction with the surface of TiO_2 is important in order to understand any potential charge transfer processes that would increase the photocatalytic potential of the adsorbed molecules.

The thermal desorption of CO_2 has been studied by Henderson et al. using TPD over a 120 to 200 K temperature range. They found two peaks corresponding to desorption of CO_2 from the undercoordinated Ti^{4+} site at 137 K, and oxygen vacancy site at 167 K.[315] Additionally, Acharya et al. looked at adsorption and desorption via STM from 80 K to 180 K and found similar desorption temperatures, with an additional desorption from the bridging oxygen sites at 115 K.[62] More recently Smith et al. studied the desorption of CO_2 at lower temperatures, finding that the CO_2 multilayer desorbs at 84 K.[61]

I performed 2PP measurements of CO_2 covered TiO_2 surfaces as a function of coverage up to 2 ML over the 31 to 300 K temperature range. As in the case of CH_3OH , CO_2 adsorption on the surface decreases the intensity of the d-d transition in 2PP spectra. As indicated above, at 80 K, the CO_2 is only able to form a monolayer with some molecules potentially at the bridging O atom sites; [62,316,317] this is enough to decrease the d-d transition intensity, but not to quench it entirely. In order to observe the effect of multilayer coverage on TiO_2 , liquid helium was used to cool the sample to 31 K. At this temperature, multilayer CO_2 is established on the surface and the d-d transition is nearly completely quenched. This decrease and quenching of the surface is shown in Figure 6.6a for 80 K and Figure 6.6b for 31 K. As shown in previous TPD measurements the CO_2 on the surface is adsorbed onto three different sites. The most favorable adsorption site is on the bridging oxygen vacancies but as those are filled the CO_2 physisorbs onto the remaining Ti^{4+} and eventually on the oxygen sites. As the coverage is increased at lower temperatures a multi-layer is formed. As CO_2 adsorbs onto the Ti sites it forms a zig-zag pattern with the neighboring molecules tilted towards the opposite bridging oxygen sites. This blocks adsorption from half the oxygen sites meaning an additional 0.5 ML can adsorb onto these sites.[318]

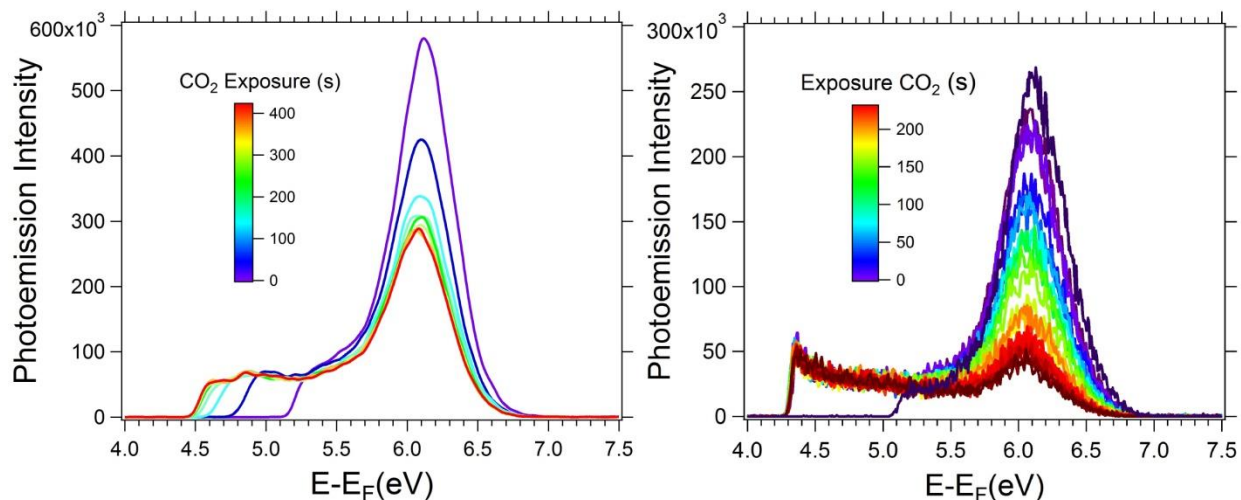


Figure 6.6- CO₂ dosing at a) 80 K and b) 31 K for 360 nm s-polarized excitation. At 80 K the d-d transition is partially quenched and the work function gradually decreases by ~0.7 eV. At 31 K the work function immediately decreases by additional 0.2 eV and the d-d transition is nearly completely, but gradually quenched by the multilayer CO₂ coverage.

Another unexpected consequence of CO₂ adsorption is the large shift of the work function to lower energies. I observe a sharp drop in the work function, followed by a decrease in the d-d transition. The drop in the work function suggests that a charge transfer from CO₂ to TiO₂ may be occurring, as in the case of CH₃OH, but the decrease in the d-d transition intensity suggests a depletion of the t_{2g} defect states. The work function change and d-d peak suppression do not appear to be correlated since at 31 K the work function change is nearly immediate, dropping to its minimum value before I can collect the first set of data, while the d-d peak suppression requires CO₂ molecules to accumulate. The prompt work function change appears to be associated with the first monolayer formation, whereas the d-d suppression appears to be due to the subsequent multilayer adsorption.

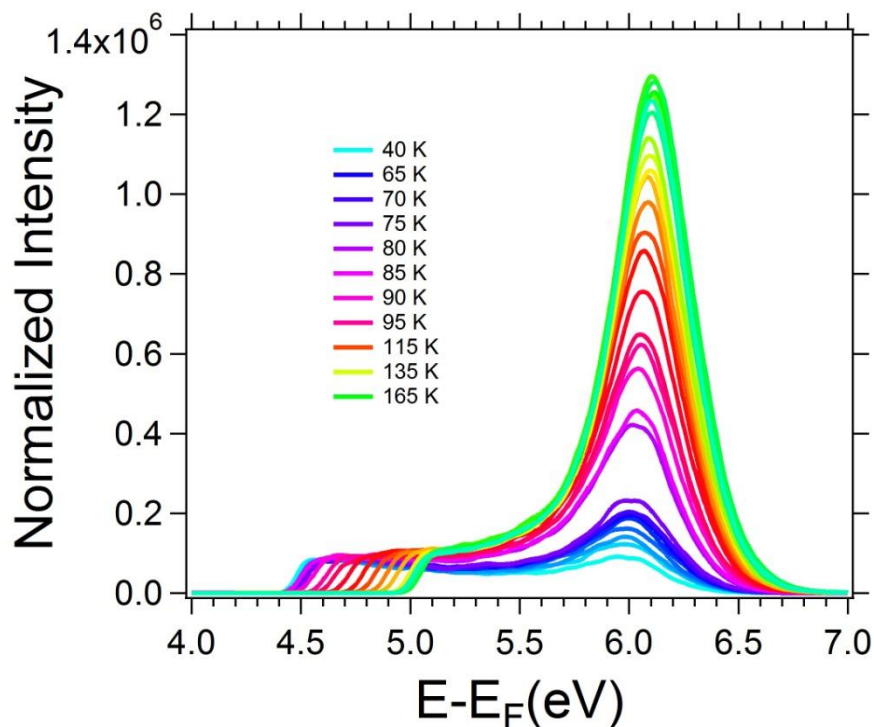


Figure 6.7- Warming the CO₂ covered surface recovers the d-d transition at ~85 K, corresponding to the desorption of the multi-layer of CO₂ on the surface. The excitation is with 360nm, s-polarized light.

To further confirm the multi-layer adsorption was responsible for the quenching behavior, the sample was heated after dosing to recover the transition intensity. As shown in figure 6.7, there is a jump in the d-d transition intensity at 85 K, corresponding to desorption of the multilayer of CO₂ from the surface. The intensity continues to change and increase even after the multilayer desorbs, indicating that the monolayer coverage still suppresses the d-d peak intensity. Finally, the sample is heated to 700 K and allowed to equilibrate until 530 K at which point CO₂ is also dosed again onto the sample. However, the 2PP spectra (not shown) do not indicate CO₂ interaction with the surface at elevated temperatures. This is consistent with the fact that CO₂ does not adsorb on or react with the surface at higher temperatures.

In order to understand the complex electronic changes induced by CO₂ adsorption, theoretical calculations were performed by Jin Zhao's group at USTC, revealing the changes in the d-d transition intensity as different coverages of CO₂ are adsorbed. Consistent with the experimental results they find a sharp decrease in the work function with the adsorption of CO₂, as well as a decrease in the d-d transition intensity.

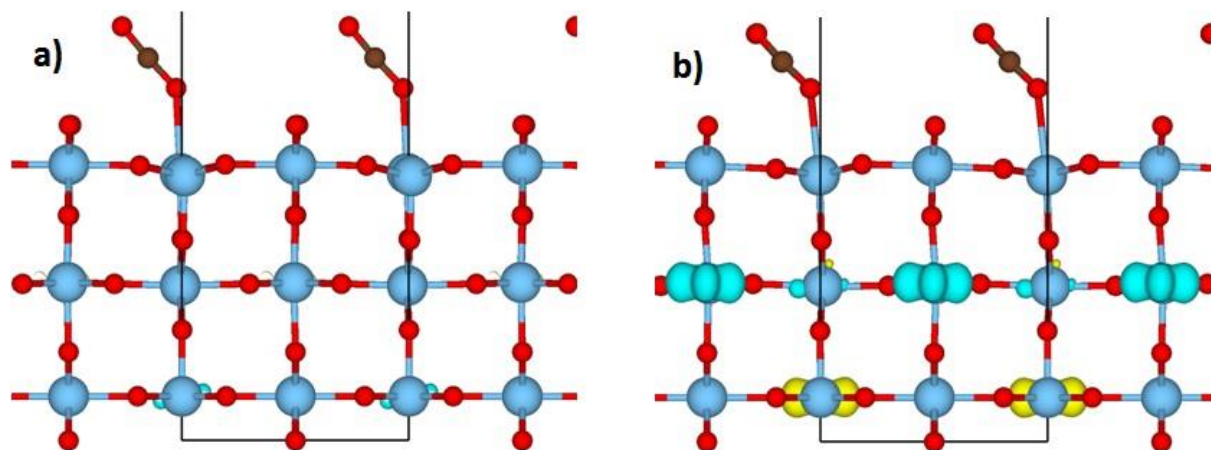


Figure 6.8- Change in the TiO_2 charge density distribution for a) 0.5 ML and b) 1 ML coverage of CO_2 on a stoichiometric TiO_2 surface. Very little change occurs in the lattice for small CO_2 coverages, but as the coverage exceeds 1 ML the d-orbital charge distribution changes causing a quenching of the d-d transition intensity.

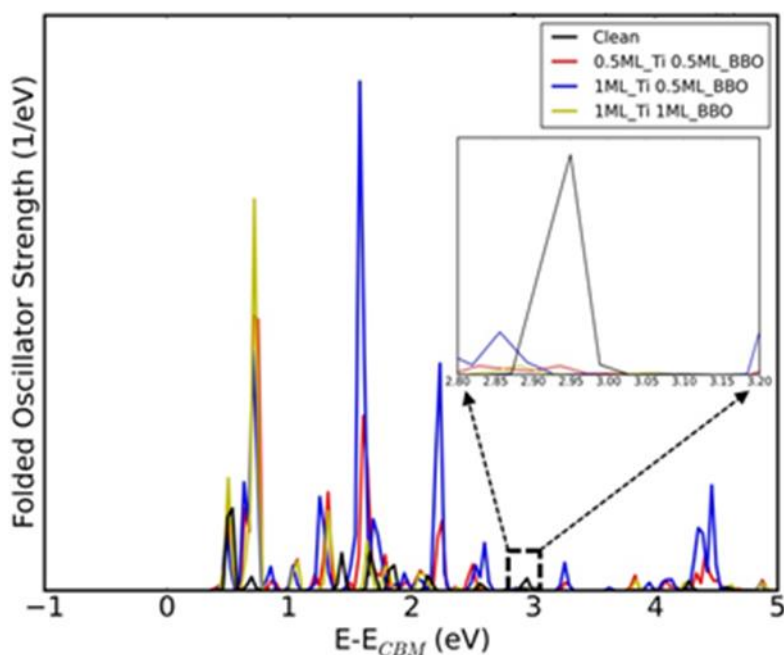


Figure 6.9- Theoretical calculation for d-d transition with multilayer CO_2 on the surface. The coverage is applied to the Ti_{5c} (Ti) sites as well as the bridging oxygen atoms (BBO). The initial state is $\text{CBM}+1$, with and without CO_2 adsorption. The d-d transition at about 3 eV above the CBM is quite sensitive to CO_2 adsorption as can be seen in the expanded region of the calculated oscillator strength.

The origin of the quenching behavior is revealed by scrutinizing the transition oscillator strengths as a function of CO_2 adsorption. As CO_2 is adsorbed onto the surface the structure of the TiO_2 lattice is distorted, leading to a change in charge density. The Ti-O bond lengths near the surface and in the subsurface layers stretch in response to the adsorbed CO_2 . For the clean surface the Ti-O bond length at

the surface is $\sim 1.95 \text{ \AA}$, but upon CO_2 adsorption it is found to stretch to as much as 2.51 \AA . Figure 6.8 shows the effect of this change on the surrounding charge density distribution. As shown in figure 6.9 the addition of a CO_2 multilayer quenches the d-d transition. In the calculation, there is a contribution from CO_2 adsorption on both the Ti sites as well as on bridging oxygen atoms [62,308]. The calculations indicate that while the individual contribution of the Ti site adsorption is slightly greater than the oxygen atom adsorption, the overall effect from the combination of these contributions is greater than the individual parts. The source of this added contribution is not clear and additional calculations are needed to clarify the overall effect. This structural relaxation causes the CBM+1 orbital, related to the Ti 3d orbitals as discussed in chapter 4, to restructure and redistribute their charge, leading to a drastic decrease in the transition intensity of the d-d transition. This change also only occurs with 1 ML coverage or more, as shown in figure 6.8. In figure 6.8a the change in the charge distribution with 0.5 ML CO_2 coverage is shown, with very little effect. This is hard to reconcile with the fact that other surface sensitive studies of CO_2 have found significant change in the charge distribution on TiO_2 with very low initial CO_2 coverage. [319] The most likely explanation for this discrepancy is that the current theoretical calculation does not include defects, which are the primary adsorption sites for low coverages of CO_2 on TiO_2 . [60,308,320] Figure 6.8b shows the much more significant change that 1 ML coverage has on the charge distribution, consistent with the quenching only occurring for high coverages at low temperatures for my system.

In addition to looking at the low temperature quenching of the d-d transitions, I also looked at the changes in the spectrum at mid range temperatures from $\sim 100 \text{ K}$ to 200 K . In this temperature range the work function of the sample is rapidly changing as the sample is heated due to desorption of CO_2 from different adsorption sites. My initial goal was to look for spectroscopic changes between the different adsorption sites of CO_2 on the surface. As discussed above CO_2 desorbs from the Ti sites at $\sim 137 \text{ K}$ and from the oxygen vacancy sites at $\sim 167 \text{ K}$. By adsorbing CO_2 onto the sample and then warming up the sample through this range I was able to look for changes in the work function, and in the d-d transition for signs of changes due to differing adsorption sites. As shown in figure 6.10, I found a non-monotonic change in the work function behavior near the desorption temperature of CO_2 . Near the Ti site desorption temperature, the work function increased linearly to nearly the clean surface value before quickly decreasing again until 200 K . Above 200 K the work function again increased until it reached its clean surface value and stayed there.

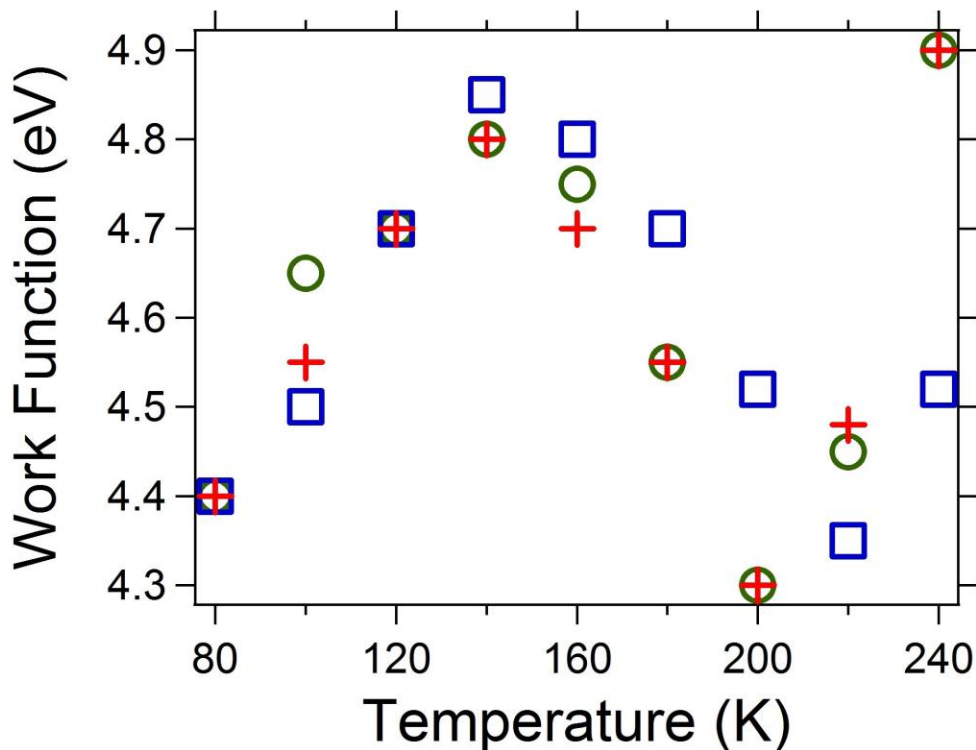


Figure 6.10: work function change vs. temperature for CO₂/H₂O on TiO₂ at 400 nm. Measurement was repeated in three times for verification

After examining the surface desorption products with the mass spectrometer, I found that residual H₂O in the chamber adsorbed onto the surface after CO₂ was removed from the Ti sites. This caused a decrease in the work function and also the formation of the wet electron state. This process is not reversible as re-cooling the sample maintains the water on the surface and also maintains the wet electron state. This state should not be confused with the LUMO of CO₂ on TiO₂ which is located at 2.3 eV.[59] To confirm this assignment, I improved the vacuum and repeated the experiment, but this time by co-adsorbing CO₂ and water on the surface in this temperature range. This resulted in the same change in work function and onset of the wet electron state as found with inadequate vacuum. Smith et al. studied a similar effect with the co-adsorption of CO₂ and H₂O and found that water can displace the CO₂ on the surface for certain temperatures.[61] Their TPD measurements were consistent with my data in that the H₂O replaced the CO₂ on the Ti sites after 140 K and on the oxygen vacancy sites at 160 K. Above 220 K the water desorbs from the surface, resulting in the recovery of the work function.

The adsorption of CO₂ onto the surface of TiO₂ gives us a different perspective on how adsorbates can impact the molecular and electronic structures of surfaces of semiconductor materials. Unlike the dipole field of CH₃OH there is no physical mechanism for the quenching of the t_{2g} to e_g transition. Instead a

much more subtle change in the Ti-O bond length caused by CO₂ adsorption changes the surface electronic structure, showing that even small changes in the lattice structure can lead to substantial redistribution of charge in the bulk and on the surface of materials.

6.3.3 2PP spectroscopy of O₂/TiO₂

Oxygen on the surface of TiO₂ has been extensively studied in the past. Its ability to heal oxygen vacancies on the surface of TiO₂ and produce a defect free surface in UHV conditions is important for study of the perfect vs. defect covered surface.[36] Yates and coworkers extensively studied the O₂/TiO₂ surface and the use of O₂ as an electron scavenger. This electron scavenging behavior enhances the hole transport ability of TiO₂ allowing better photocatalytic activity to occur on the surface.[321,322] Additional studies have looked at the photodesorption of O₂ from the TiO₂ surface using 3-4 eV photons from a lamp source, in order to provide information on photocatalytic reactions of adsorbed molecules.[2,323,324] These studies have mostly focused on the surface interactions of TiO₂ with adsorbed oxygen where the majority of the chemistry is thought to take place.[69,202,325] The interaction of the adsorbed molecules with the subsurface has not been studied as thoroughly although it may be important for understanding the interactions.[29,326] Here I present a study of the adsorption of oxygen on the TiO₂ surface and its interaction with the mostly subsurface defect derived t_{2g} to e_g transition. The effect that adsorbed molecules have on this transition was seen to be very important in the case of CH₃OH and CO₂, and continues to be of importance here.

The final experiment performed was dosing oxygen onto the reduced TiO₂ surface. This was again done at 31 K, 80 K, and high temperature. Unlike the previous measurements, O₂ dosed onto the TiO₂ surface at 31 K did not lead to a significant change in the d-d intensity. As seen in figure 6.11, the work function increased in accordance to previous studies, however the d-d transition was mostly unaffected.[36] This lack of interaction at low temperature can be understood by noting that O₂ dissociation on both the stoichiometric TiO₂ surface as well as at the defect sites is an activated process, which does not occur below 150 K.[202,327,328] Kimmel et al. studied the TPD of oxygen and also its interaction with the stoichiometric and reduced surfaces.[327] They found that oxygen molecules on the stoichiometric surface can only physisorb below 60 K by a weak van der Waal's force. On the reduced TiO₂ surface, O₂ can both physisorb and chemisorb with the oxygen preferentially adsorbing onto the bridging oxygen vacancy sites. At temperatures above 150 K the adsorbed O₂ dissociates and heals the vacancy leaving

an oxygen adatom on a nearby under coordinated Ti site.[202,327,328] At 410 K another desorption process occurs, removing oxygen adatoms from the remaining Ti sites leaving only O atoms that have healed the oxygen vacancy sites.[57] At low temperatures oxygen molecules cannot dissociate on the surface, and therefore their interactions are weaker as compared with atomic oxygen. In order to investigate the interaction of atomic oxygen on the surface the dosing of oxygen was repeated at 80 K and again at 300-500 K where the surface allows for dissociation of oxygen.

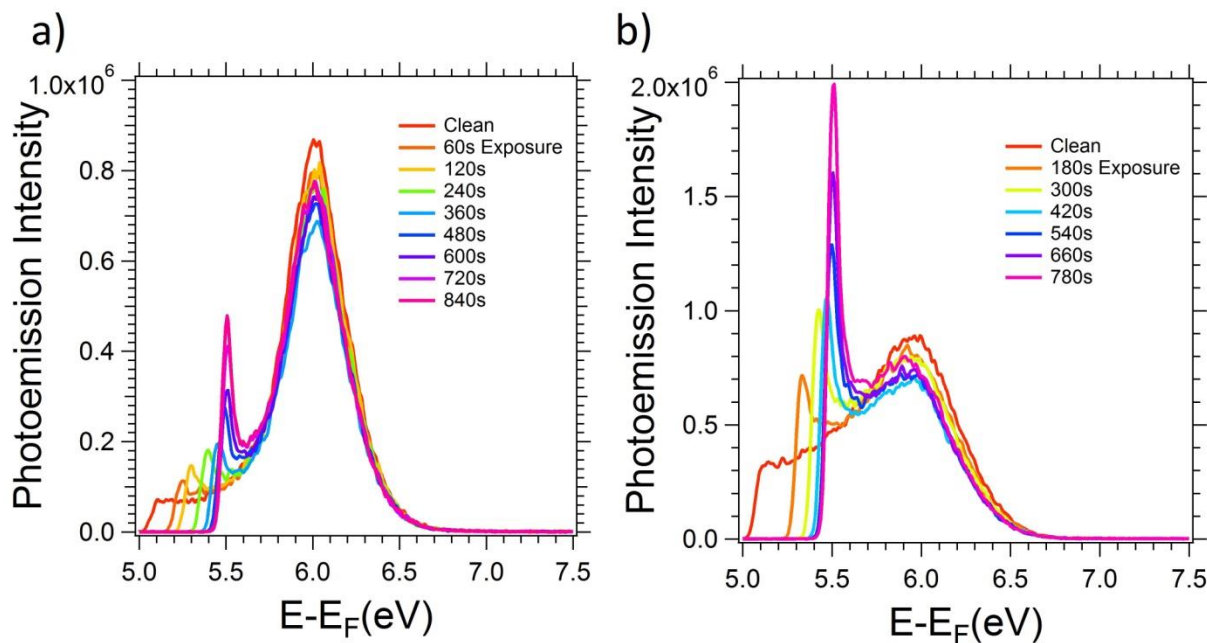


Figure 6.11- O_2 adsorption on the TiO_2 [001] aligned surface at 31 K for 360 nm excitation. a) 2PP spectra with s-polarized and b) p-polarized excitation show no significant change in intensity with increasing coverage.

Additionally, theoretical studies have found that oxygen interacts with the surface better at low coverages, so the experiment was repeated at 80 K where less than 1 ML coverage is expected.[327,329] Figure 6.12 shows the effect of low exposure O_2 on the surface. At this temperature there is a decrease in intensity, but the effect on the interaction is significantly less than with both methanol and CO_2 . I found no conditions under which the d-d transition was fully quenched by adsorption of oxygen. This is puzzling because in previous studies O_2 has been used to quench the Ti-3d defect signal in conventional photoemission spectra of TiO_2 with UV light. [34,36]

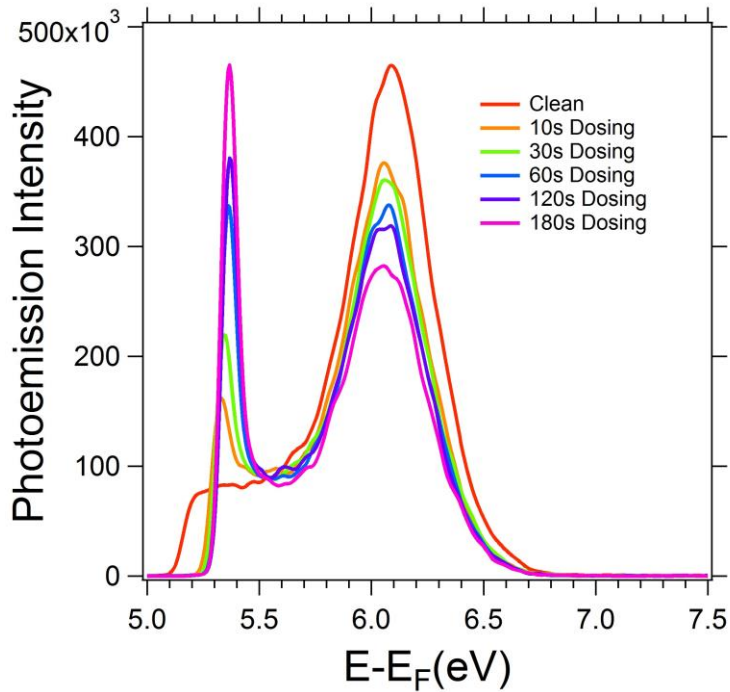


Figure 6.12 - O₂ adsorption at 80 K on the TiO₂ surface. Intensity decreased for low coverage, but is never fully quenched. The excitation is with 360 nm, s-polarized light with the [001] axis aligned in the optical plane.

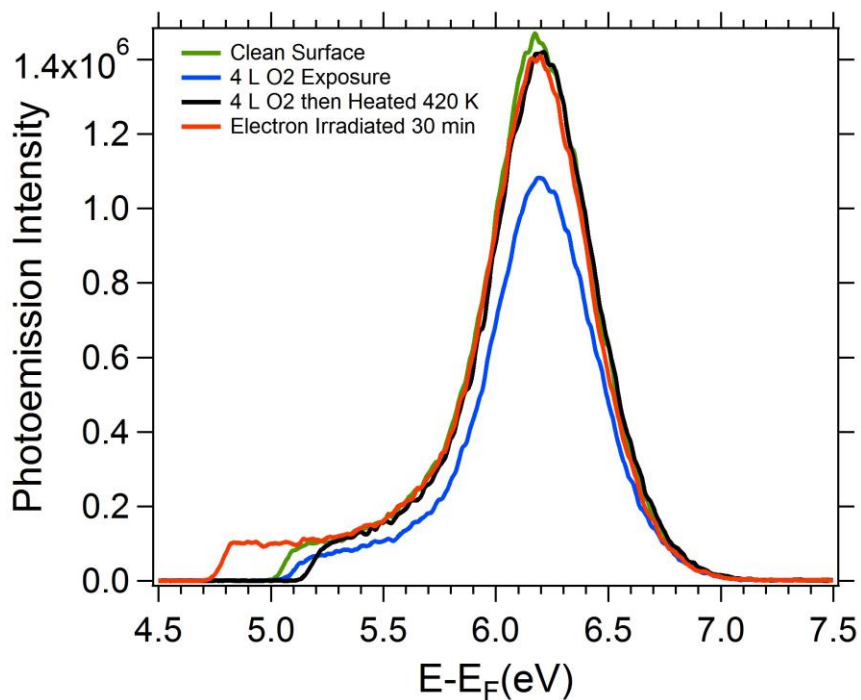


Figure 6.13- O₂ adsorption at 300 K with 360 nm light on with the [001] axis aligned in the optical plane. After 4 L of exposure the intensity is reduced but then recovered upon removal of oxygen from the Ti sites. Sample is then irradiated with 500 eV electrons at 50 nA to recovery oxygen vacancies but no additional intensity is gained.

The effect, or more accurately the lack of effect of oxygen adsorption is important as it shows the origin of the d-d transition state is not just due to surface oxygen vacancies, which should be quenched when O_2 is adsorbed at above 160 K, but instead it has dominant contributions from the bulk defects or Ti interstitials. It also lends credence to the recent studies that show the origin of the TiO_2 defect state are primarily due to the interstitial Ti states and not oxygen vacancies as has previously been reported.[29,330]

To verify this conclusion, I performed the following set of experiments. Oxygen was dosed at room temperature where the molecules should dissociate on the surface and completely heal the oxygen vacancies as shown in figure 6.13. This was discussed in chapter 4 in regards to removing OH from the surface. In summary, the t_{2g} to e_g transition intensity is initially decreased by about 25%, which is reasonable if oxygen vacancies make some contribution to the defect state density. The healing of the defect states, and the increase of the work function additionally indicate that any residual OH on the surface is likely removed and may be responsible for some of the decrease in the transition intensity due to the removal of electron density that accompanies the removal of OH on the surface. Next, the sample was heated to 420 K in order to remove oxygen atoms from the Ti sites, leaving only the clean surface with a minimum concentration of surface vacancies.[57] This immediately recovers 100% of the initial d-d transition intensity. Next the surface was irradiated with 500 eV electrons from an electron gun at 50 nA current to recover the surface oxygen vacancies, but without introducing the surface OH. In this case the transition intensity is unaffected, whereas the work function decreased.

To investigate further, oxygen was dosed at high temperature and the d-d transition intensity was observed. Previous studies have reported that the defect states on TiO_2 are healed by dosing oxygen at higher temperature onto the TiO_2 surface.[57,331-333] If the transition is caused by OH adsorption or the defect state is caused by surface oxygen vacancies alone, then dosing oxygen should remove or decrease the transition intensity. As shown in Figure 6.14 dosing oxygen at 533 K has little effect on the transition intensity. The intensity of the transition matches the expected electron-phonon temperature dependence increase at high temperatures. As the temperature lowers oxygen is dosed at a constant rate, which leads to an increase in the work function, consistent with the healing of oxygen vacancies on the surface. However from 533 K down to 453 K the intensity of the transition levels off and does not show any change beyond what is expected due to the electron phonon temperature dependence discussed in chapter 5. Dosing oxygen fills the majority of the defect sites, preventing OH from adsorbing onto the surface. This stops the charge transfer to the defect states, keeping the peak intensity

constant. Once the oxygen dosing is turned off, OH begins to adsorb on the surface, decreasing the work function and causing a slight increase in the peak intensity.

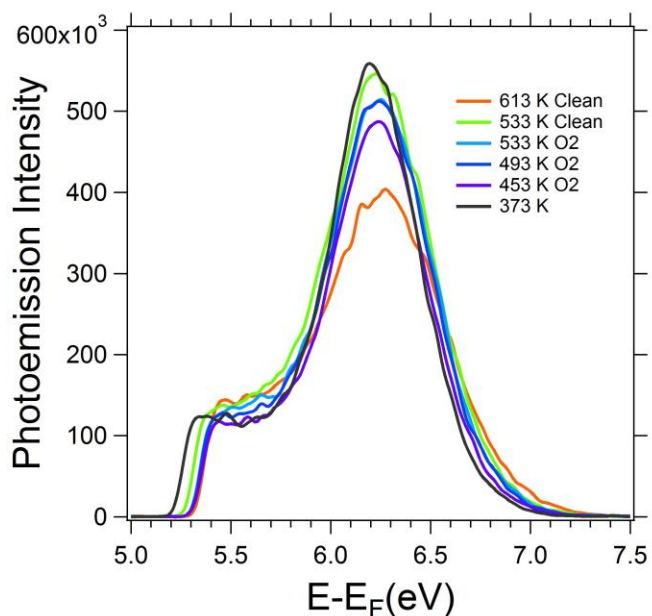


Figure 6.14- High temperature oxygen dosing on the TiO₂ surface. Intensity remains constant while dosing O₂, giving merit to the idea that defect states do not originate entirely from oxygen vacancies but instead from interstitial Ti.

This set of results while initially surprising is important in our understanding of adsorbates on the TiO₂ surface. Unlike the previous adsorbates, oxygen did not have a large effect on the lattice or on the charge density distribution of the bulk. This shows that while surface effects can be important it is also important to look at the subsurface and bulk contributions as they can play a significant role in the interaction between a substrate and adsorbates. My measurements look at the subsurface contribution to these interactions and show that the resultant chemistry is not limited to just the surface layer as is frequently studied. It is important to consider the contribution from not only the surface layer but from the subsurface as well which can have additional effects on the interactions. Even when this interaction is not as strong as the surface effects, as in the case here for oxygen, the smaller changes can be just as important to form an overall picture.

6.4 Conclusion

Multiphoton photoemission was used to study the adsorbate covered TiO₂ surface for a variety of molecules. ~20 fs laser pulses from 3.3-3.6 eV were used to probe the rutile TiO₂(110) single crystal surface, along both crystalline directions. The principle interaction was observed by the changing

interaction of the t_{2g} to e_g transition with the addition of adsorbates. A stronger impact on these states was observed for both methanol and carbon dioxide, as compared to oxygen. Past results and theoretical calculations led to the conclusion that changes in the lattice as well as the interaction of subsurface and bulk defects play a significant role in the interaction between the surface and adsorbates. Additionally the structure and form of the adsorbed molecules plays an important role in the interaction with the surface. By correctly tuning temperature and dosing rates different interactions can be studied giving the ability to tune the surface and molecule interaction to varying degrees. Further research in this area is needed to explore the possible implications for photocatalytic reactions using this newfound insight.

7. Chapter Seven: Conclusions and Future Work

This work set out to investigate the fundamental dynamics of the TiO_2 surface using photoemission spectroscopy to probe the sample surface. The rutile TiO_2 surface has been extensively studied, but the fundamental processes that define its use for photocatalytic and photovoltaic remain poorly understood. In order to gain additional insight of the dynamics on the surface and the interaction of the surface with adsorbed molecules I employed the newly designed and built NOPA laser system to probe the clean surface over a wide range of excitation wavelengths. The understanding of how surface adsorbents interact and adsorb onto the surface is important for increasing the potential of future materials in photocatalytic applications.

Multi-photon photoemission is uniquely suited for this study since it allows one to probe the fundamental electronic transitions on the surface to obtain energy, momentum, and time resolved information. The excitation of the surface with UV light allows us to probe both the surface and bulk of the material owing to its penetration depth. The probing depth is estimated to be several nanometers due to the electron escape depth for the few eV energy range. Additionally the use of ultra short pulses gives us time resolved data down to only a few tens of femtoseconds and allows us to probe even weak interactions due to the high peak intensity of the pulses. These factors combine to make photoemission spectroscopy a powerful technique to probe the surface of many different materials. By combining this technique with the wide excitation range of the NOPA along with the high sensitivity of our detector, I was able to uniquely probe the TiO_2 surface in a novel and informative manner. By adding an interferometer time resolved experiments can be performed, giving information on the dynamics of the interactions. In the case of time resolved two photon photoemission the first pulse excites an electron

from below E_F into a transiently populated intermediate state. The second pulse then further excites this electron from that state, between E_F and E_V out of the sample above E_V which it can then be collected by the detector. This provides the ability to probe both occupied and unoccupied states in a material with both energy and time resolution.

The use of these photoemission techniques led to the discovery of a new electronic transition between the d-bands of TiO_2 . I located a pair of these states at 2.60 and 2.73 eV above the Fermi level using UV excitation. The origin of these states is the interaction of the Ti-3d orbitals with the crystal field, which causes them split into the t_{2g} and e_g states. The t_{2g} states are lower in energy and occupied by excess electrons from the predominantly bulk defects in the sample, while the e_g states are unoccupied. The dynamics of this transition were also studied but the lifetime of the electrons in the e_g state was found to be <20 fs, making it unlikely to be useful for photocatalytic reactions. Additionally, this transition highlights the importance of the anisotropy of the sample during study and provided a framework for additional experiments. By selecting the correct sample and polarization orientation I was able to selectively excite the transition of either a single or both e_g states. The ability to precisely tune the excitation wavelength into the resonance of this d-band transition allows us to monitor the change in the sample under various conditions.

To illustrate this, temperature dependent measurements were performed to observe the effect of temperature on the electronic transitions. This revealed the polaronic behavior of the t_{2g} electrons and the electron phonon interaction was investigated in detail for a more complete explanation. Excess electrons localized around the Ti atoms cause a distortion of the lattice, creating a polaron located ~ 0.8 eV below the Fermi level. This distortion changes with temperature and theoretical calculations of the electron phonon interaction show a shift in the t_{2g} and e_g energies consistent with the experimental results down to 100 K. This shift in energy manifests itself as change in the resonant energy, resulting in a shift of the energy where the t_{2g} to e_g transition appears in 2PP spectra. Below 100 K the energy of the transition decreases rapidly, due to an unknown additional interaction. This low temperature change needs to be further explored in future work and may be the result of a bi-polaron or other more complex interactions. More careful study using even lower temperatures would be ideal for further characterization, and combined with a more detailed theoretical model, which includes the effects of defects, should be able to provide further insights.

With the additional insight on the clean surface electronic structure, electron-phonon interactions, and dynamics, the final set of experiments investigated the interaction of adsorbed molecules on the

surface. Understanding the electron interactions between the surface and adsorbed molecules is important in understanding the process and limits of photocatalytic reactions. Methanol, CO₂ and Oxygen were independently adsorbed on to the surface and the change in the t_{2g} to e_g transition was observed. The interaction of the molecules with the TiO₂ surface varied greatly with both temperature and coverage, with even small changes making large differences in the 2PP spectra. In the case of methanol, adsorbing at low temperature resulted in a strongly interacting amorphous layer on the surface, which quenched the t_{2g} to e_g transition. When heated to ~120 K the amorphous layer restructured resulting in the crystallization of the adsorbed molecules, which reduced the interaction strength to nearly zero, recovering the d-band transition. A similar strong interaction was observed with CO₂ at low temperatures, but the mechanism turned out to be very different. Theoretical calculations showed that the strong interaction with the surface, leading to the quenching of the t_{2g} to e_g transition was due to structural changes induced by the adsorption of the CO₂. These changes produced large changes in the Ti-3d electron distributions in the material for coverages of >1 ML. Finally oxygen on the surface was found to have very little interaction with the t_{2g} to e_g transition, lending credence to the assignment of this state as primarily originating from bulk defects as opposed to surface defects. The oxygen on the surface fills the majority of the surface oxygen vacancies leading to an increase in the work function, but had only a small effect on the t_{2g} to e_g transition. This shows the importance of subsurface and bulk defects on the properties of adsorbates and with the interaction these adsorbates have with the TiO₂ substrate. Future studies should look at the interaction of multiple molecules on the TiO₂ surface simultaneously in order to understand the chemistry that happens on the surface under irradiation.

The results of these experiments and the impact they will have on future work shows the importance of 2PP experiments and the usefulness of having a broadly tunable femtosecond excitation source. The development and implementation of the NOPA system when combined with 2PP allows for many exciting and interesting experiments to be performed that were previously out of reach. The use of this system will continue to produce exciting new results for years to come. My work in this thesis has advanced the understanding of the TiO₂ system and its interaction with adsorbed molecules for use as a photocatalytic material. This new understanding will pave the way for future studies on the limitations of these reactions and how they can be overcome.

Bibliography

- [1] A. Fujishima and K. Honda, *Nature* **238**, 37 (1972).
- [2] A. Fujishima, X. Zhang, and D. A. Tryk, *Surf. Sci. Rep.* **63**, 515 (2008).
- [3] M. Gratzel, *Nature* **414**, 338 (2001).
- [4] M. A. Henderson, *Surf. Sci. Rep.* **66**, 185 (2011).
- [5] M. R. Hoffmann, S. T. Martin, W. Choi, and D. W. Bahnemann, *Chemical Reviews* **95**, 69 (1995).
- [6] C. Lun Pang, R. Lindsay, and G. Thornton, *Chemical Society reviews* **37**, 2328 (2008).
- [7] T. L. Thompson and J. T. Yates, Jr., *Chem. Rev.* **106**, 4428 (2006).
- [8] U. Diebold, *Surf. Sci. Rep.* **48**, 53 (2003).
- [9] M. I. Ahmad, C. Fasel, T. Mayer, S. S. Bhattacharya, and H. Hahn, *Applied Surface Science* **257**, 6761 (2011).
- [10] C. Popescu, J. A. Sans, D. Errandonea, A. Segura, R. Villanueva, and F. Sapiña, *Inorganic Chemistry* **53**, 11598 (2014).
- [11] M. Xu, Y. Gao, E. M. Moreno, M. Kunst, M. Muhler, Y. Wang, H. Idriss, and C. Wöll, *Phys. Rev. Lett.* **106**, 138302 (2011).
- [12] H. Zhang and J. F. Banfield, *Journal of Materials Chemistry* **8**, 2073 (1998).
- [13] D. A. H. Hanaor and C. C. Sorrell, *Journal of Materials Science* **46**, 855 (2011).
- [14] Rutile Crystal, <https://commons.wikimedia.org/wiki/File:Rutile-122157.jpg>.
- [15] V. E. Henrich, *The Surface Science of Metal Oxides* (Cambridge University Press, Cambridge, 1996), 1 edn., Vol. 1.
- [16] N. Serpone, *Photocatalysis : fundamentals and applications* 1989).
- [17] L. Chiodo, J. M. García-Lastra, A. Iacomino, S. Ossicini, J. Zhao, H. Petek, and A. Rubio, *Phys. Rev. B* **82**, 045207 (2010).
- [18] A. Bouzoubaa, A. Markovits, M. Calatayud, and C. Minot, *Surf. Sci.* **583**, 107 (2005).
- [19] P. M. Kowalski, B. Meyer, and D. Marx, *Phys. Rev. B* **79**, 115410 (2009).
- [20] M. Landmann, E. Rauls, and W. G. Schmidt, *Journal of Physics: Condensed Matter* **24**, 195503 (2012).
- [21] O. Byl and J. T. Yates, *The Journal of Physical Chemistry B* **110**, 22966 (2006).
- [22] A. K. See, M. Thayer, and R. A. Bartynski, *Phys. Rev. B* **47**, 13722 (1993).
- [23] C. Di Valentin, *J. Chem. Phys.* **127**, 154705 (2007).
- [24] D. W. Fischer, *Phys. Rev. B* **5**, 4219 (1972).
- [25] G. Charlton *et al.*, *Physical Review Letters* **78**, 495 (1997).
- [26] N. M. Harrison, X. G. Wang, J. Muscat, and M. Scheffler, *Faraday Discussions* **114**, 305 (1999).
- [27] P. J. Møller and M.-C. Wu, *Surface Science* **224**, 265 (1989).
- [28] C. Di Valentin, G. Pacchioni, and A. Selloni, *Phys. Rev. Lett.* **97**, 166803 (2006).
- [29] S. Wendt *et al.*, *Science* **320**, 1755 (2008).
- [30] T. Bredow and G. Pacchioni, *Chem. Phys. Lett.* **355**, 417 (2002).
- [31] X. Cui, B. Wang, Z. Wang, T. Huang, Y. Zhao, J. Yang, and J. G. Hou, *J. Chem. Phys.* **129**, 044703 (2008).
- [32] M. V. Ganduglia-Pirovano, A. Hofmann, and J. Sauer, *Surf. Sci. Rep.* **62**, 219 (2007).
- [33] P. J. Hardman, N. S. Prakash, C. A. Muryn, G. N. Raikar, A. G. Thomas, A. F. Prime, G. Thornton, and R. J. Blake, *Phys. Rev. B* **47**, 16056 (1993).
- [34] C. M. Yim, C. L. Pang, and G. Thornton, *Phys. Rev. Lett.* **104**, 036806 (2010).
- [35] S. Wendt, R. Bechstein, S. Porsgaard, E. Lira, J. Ø. Hansen, P. Huo, Z. Li, B. Hammer, and F. Besenbacher, *Phys. Rev. Lett.* **104**, 259703 (2010).
- [36] K. Onda, B. Li, and H. Petek, *Phys. Rev. B* **70**, 045415 (2004).

- [37] V. Sametoglu, 2009).
- [38] X. Y. Zhu, *Surface Science Reports* **56**, 1 (2004).
- [39] M. Cardona and G. Harbeke, *Physical Review* **137**, A1467 (1965).
- [40] A. Amtout and R. Leonelli, *Physical Review B* **51**, 6842 (1995).
- [41] Y. Tezuka, S. Shin, T. Ishii, T. Ejima, S. Suzuki, and S. Sato, *Journal of the Physical Society of Japan* **63**, 347 (1994).
- [42] S. Rangan, S. Katalinic, R. Thorpe, R. A. Bartynski, J. Rochford, and E. Galoppini, *The Journal of Physical Chemistry C* **114**, 1139 (2010).
- [43] P. J. Hardman, G. N. Raikar, C. A. Muryn, G. van der Laan, P. L. Wincott, G. Thornton, D. W. Bullett, and P. A. D. M. A. Dale, *Physical Review B* **49**, 7170 (1994).
- [44] A. K. Ghosh, F. G. Wakim, and R. R. Addiss, *Physical Review* **184**, 979 (1969).
- [45] S. Hufner and G. K. Wertheim, *Physical Review B* **7**, 2333 (1973).
- [46] F. M. F. de Groot, M. Grioni, J. C. Fuggle, J. Ghijsen, G. A. Sawatzky, and H. Petersen, *Physical Review B* **40**, 5715 (1989).
- [47] K. Watanabe, K. Inoue, and F. Minami, *Physical Review B* **46**, 2024 (1992).
- [48] M. Arai, S. Kohiki, H. Yoshikawa, S. Fukushima, Y. Waseda, and M. Oku, *Physical Review B* **65**, 085101 (2002).
- [49] N. Vast, L. Reining, V. Olevano, P. Schattschneider, and B. Jouffrey, *Physical Review Letters* **88**, 037601 (2002).
- [50] W. Kang and M. S. Hybertsen, *Physical Review B* **82**, 085203 (2010).
- [51] H. M. Lawler, J. J. Rehr, F. Vila, S. D. Dalosto, E. L. Shirley, and Z. H. Levine, *Phys. Rev. B* **78**, 205108 (2008).
- [52] D. C. Cronmeyer and M. A. Gilleo, *Physical Review* **82**, 975 (1951).
- [53] R. Asahi, T. Morikawa, T. Ohwaki, K. Aoki, and Y. Taga, *Science* **293**, 269
- [54] (2001). Chem Wiki Crystal Field Theory, http://chemwiki.ucdavis.edu/Core/Inorganic_Chemistry/Crystal_Field_Theory/Crystal_Field_Theory.
- [55] C. L. Pang, R. Lindsay, and G. Thornton, *Chem. Rev.* **113**, 3887 (2013).
- [56] M. A. Henderson, W. S. Epling, C. H. F. Peden, and C. L. Perkins, *J. Phys. Chem. B* **107**, 534 (2003).
- [57] M. A. Henderson, W. S. Epling, C. L. Perkins, C. H. F. Peden, and U. Diebold, *The Journal of Physical Chemistry B* **103**, 5328 (1999).
- [58] M. Li, W. Hebenstreit, U. Diebold, M. A. Henderson, and D. R. Jennison, *Faraday Discuss.* **114**, 245 (1999).
- [59] S. Tan *et al.*, *Phys. Rev. B* **84**, 155418 (2011).
- [60] D. C. Sorescu, J. Lee, W. A. Al-Saidi, and K. D. Jordan, *J. Chem. Phys.* **134**, 104707 (2011).
- [61] R. S. Smith, Z. Li, L. Chen, Z. Dohnálek, and B. D. Kay, *The Journal of Physical Chemistry B* **118**, 8054 (2014).
- [62] D. P. Acharya, N. Camillone, and P. Sutter, *The Journal of Physical Chemistry C* **115**, 12095 (2011).
- [63] S. P. Bates, M. J. Gillan, and G. Kresse, *The Journal of Physical Chemistry B* **102**, 2017 (1998).
- [64] R. Sánchez de Armas, J. Oviedo, M. A. San Miguel, and J. F. Sanz, *J. Phys. Chem. C* **111**, 10023 (2007).
- [65] J. Oviedo, R. Sánchez de Armas, M. Á. San Miguel, and J. F. Sanz, *J. Phys. Chem. C* **112**, 17737 (2008).
- [66] S. Liu, A.-a. Liu, B. Wen, R. Zhang, C. Zhou, L.-M. Liu, and Z. Ren, *The Journal of Physical Chemistry Letters* **6**, 3327 (2015).
- [67] R. Lindsay *et al.*, *Surf. Sci.* **547**, L859 (2003).
- [68] J. Schnadt *et al.*, *J. Chem. Phys.* **119**, 12462 (2003).

- [69] E. Wahlström, E. K. Vestergaard, R. Schaub, A. Ronnau, M. Vestergaard, E. Laegsgaard, I. Stensgaard, and F. Besenbacher, *Science* **303**, 511 (2004).
- [70] B. Li, J. Zhao, K. Onda, K. D. Jordan, J. Yang, and H. Petek, *Science* **311**, 1436 (2006).
- [71] K. Onda, B. Li, J. Zhao, K. D. Jordan, J. Yang, and H. Petek, *Science* **308**, 1154 (2005).
- [72] K. Onda, B. Li, J. Zhao, and H. Petek, *Surf. Sci.* **593**, 32 (2005).
- [73] M. A. Henderson, *Langmuir* **12**, 5093 (1996).
- [74] I. M. Brookes, C. A. Muryn, and G. Thornton, *Phys. Rev. Lett.* **87**, 266103 (2001).
- [75] R. Schaub, P. Thostrup, N. Lopez, E. Lagsgaard, I. Stensgaard, J. K. Norskov, and F. Besenbacher, *Phys. Rev. Lett* **87**, 266104 (2001).
- [76] T. Fauster, *Progress in Surface Science* **46**, 177 (1994).
- [77] J. H. Bechtel, W. Lee Smith, and N. Bloembergen, *Physical Review B* **15**, 4557 (1977).
- [78] K. F. W. a. A. Sanchez, *The Lincoln Laboratory Journal* **3** (1990).
- [79] J. A. Giordmaine and R. C. Miller, *Physical Review Letters* **14**, 973 (1965).
- [80] A. Galvanauskas, A. Hariharan, D. Harter, M. A. Arbore, and M. M. Fejer, *Opt. Lett.* **23**, 210 (1998).
- [81] L. Gundlach, R. Ernstorfer, and F. Willig, *Prog. Surf. Sci.* **82**, 355 (2007).
- [82] L. Gundlach, R. Ernstorfer, E. Riedle, R. Eichberger, and F. Willig, *Applied Physics B* **80**, 727 (2005).
- [83] E. Riedle, M. Beutter, S. Lochbrunner, J. Piel, S. Schenkl, S. Spörlein, and W. Zinth, *Applied Physics B* **71**, 457 (2000).
- [84] A. Argondizzo, X. Cui, C. Wang, H. Sun, H. Shang, J. Zhao, and H. Petek, *Physical Review B* **91**, 155429 (2015).
- [85] X. Cui, C. Wang, A. Argondizzo, S. Garrett-Roe, B. Gumhalter, and H. Petek, *Nat Phys* **10**, 505 (2014).
- [86] A. Einstein, *Annalen der Physik* **322**, 132 (1905).
- [87] C. R. a. B. Brundle, A. D., *Electron Spectroscopy: Theory, Techniques, and Applications* (Academic Press, New York, New York, 1977), Vol. 1.
- [88] S. Hufner, *Photoelectron Spectroscopy: Principles and Applications* (Springer, 2003), 3 edn., Vol. 1, p. 50-51.
- [89] M. a. L. L. Cardona, *Photoemission in Solids* (Springer, 1978), Vol. 2.
- [90] R. Courths and S. Hufner, *Physics Reports* **112**, 53 (1984).
- [91] D. Andrea, *Physica Scripta* **2004**, 61 (2004).
- [92] H. Puff, *physica status solidi (b)* **4**, 125 (1964).
- [93] C. N. Berglund and W. E. Spicer, *Physical Review* **136**, A1030 (1964).
- [94] M. A. V. H. Wolfgang Schattke, *Solid-State Photoemission and Related Methods: Theory and Experiment* (Wiley, 2003).
- [95] P. M. Echenique, R. Berndt, E. V. Chulkov, T. Fauster, A. Goldmann, and U. Höfer, *Surface Science Reports* **52**, 219 (2004).
- [96] P. S. Kirchmann, *Ultrafast Dynamics in Low-Dimensional Materials* (University of Berlin, University of Berlin, 2008).
- [97] H. Ueba and T. Mii, *Applied Physics A* **71**, 537 (2000).
- [98] J. Braun and M. Donath, *Journal of Physics: Condensed Matter* **16**, S2539 (2004).
- [99] M. P. Seah and W. A. Dench, *Surface and Interface Analysis* **1**, 2 (1979).
- [100] C. J. Powell, *Journal of Electron Spectroscopy and Related Phenomena* **47**, 197 (1988).
- [101] S. Tanuma, C. J. Powell, and D. R. Penn, *Surface and Interface Analysis* **37**, 1 (2005).
- [102] L. D. Laude and M. Wautelet, *Il Nuovo Cimento B (1971-1996)* **39**, 734 (2007).
- [103] M. Wautelet and L. D. Laude, *Physical Review Letters* **38**, 40 (1977).
- [104] H. Petek, *The Journal of Chemical Physics* **137**, 091704 (2012).

- [105] H. Petek and S. Ogawa, *Progress in Surface Science* **56**, 239 (1997).
- [106] E. P. Halevi, Elsevier, Amsterdam, *Two-photon photoemission spectroscopy of image states* (1995), p.^pp. 347-411.
- [107] H. Petek, A. P. Heberle, W. Nessler, H. Nagano, S. Kubota, S. Matsunami, N. Moriya, and S. Ogawa, *Physical Review Letters* **79**, 4649 (1997).
- [108] N.-H. Ge, C. M. Wong, R. L. Lingle, J. D. McNeill, K. J. Gaffney, and C. B. Harris, *Science* **279**, 202 (1998).
- [109] A. D. Miller, I. Bezel, K. J. Gaffney, S. Garrett-Roe, S. H. Liu, P. Szymanski, and C. B. Harris, *Science* **297**, 1163 (2002).
- [110] W. Martin, *Journal of Physics: Condensed Matter* **14**, R1099 (2002).
- [111] N. V. Smith, *Reports on Progress in Physics* **51**, 1227 (1988).
- [112] R. Haight, *Surface Science Reports* **21**, 275 (1995).
- [113] K. Giesen, F. Hage, F. J. Himpsel, H. J. Riess, and W. Steinmann, *Physical Review Letters* **55**, 300 (1985).
- [114] P. Lambropoulos, *Physical Review A* **9**, 1992 (1974).
- [115] J. Hermanson, *Solid State Communications* **22**, 9 (1977).
- [116] W. Steinmann, *Progress in Surface Science* **42**, 89 (1993).
- [117] J. Appel, *Physical Review* **122**, 1760 (1961).
- [118] V. F. Gantmakher, *Reports on Progress in Physics* **37**, 317 (1974).
- [119] M. G. Holland, *Physical Review* **134**, A471 (1964).
- [120] P. J. Price, *Annals of Physics* **133**, 217 (1981).
- [121] V. P. Zhukov, V. G. Tyuterev, and E. V. Chulkov, *Journal of Physics: Condensed Matter* **24**, 405802 (2012).
- [122] S. Ogawa, H. Nagano, and H. Petek, *Physical Review Letters* **88**, 116801 (2002).
- [123] M. J. Weida, S. Ogawa, H. Nagano, and H. Petek, *Applied Physics A* **71**, 553.
- [124] J. Piel, E. Riedle, L. Gundlach, R. Ernstorfer, and R. Eichberger, *Opt. Lett.* **31**, 1289 (2006).
- [125] D. C. Edelstein, E. S. Wachman, L. K. Cheng, W. R. Bosenberg, and C. L. Tang, *Applied Physics Letters* **52**, 2211 (1988).
- [126] D. A. Kleinman, *Physical Review* **126**, 1977 (1962).
- [127] M. Bradler, P. Baum, and E. Riedle, *Applied Physics B* **97**, 561 (2009).
- [128] G. Cerullo and S. De Silvestri, *Review of Scientific Instruments* **74**, 1 (2003).
- [129] W. Y. CHEN, *Chinese Journal of Physics* **16**, 9 (1978).
- [130] D. N. Nikogosyan, *Applied Physics A* **52**, 359 (1991).
- [131] D. Eimerl, L. Davis, S. Velsko, E. K. Graham, and A. Zalkin, *Journal of Applied Physics* **62**, 1968 (1987).
- [132] J. M. Manley and H. E. Rowe, *Proceedings of the IRE* **44**, 904 (1956).
- [133] H. E. Rowe, *Proceedings of the IRE* **46**, 850 (1958).
- [134] K. L. Cheng, W. Bosenberg, F. W. Wise, I. A. Walmsley, and C. L. Tang, *Applied Physics Letters* **52**, 519 (1988).
- [135] T. Imran and G. Figueira, *AIP Conference Proceedings* **1228**, 370 (2010).
- [136] J. A. Armstrong, *Applied Physics Letters* **10**, 16 (1967).
- [137] K. Sala, G. Kenney-Wallace, and G. Hall, *IEEE Journal of Quantum Electronics* **16**, 990 (1980).
- [138] R. K. Jain, J. E. Brown, and W. P. Robinson, *Appl. Opt.* **21**, 4073 (1982).
- [139] A. Weiner, *IEEE Journal of Quantum Electronics* **19**, 1276 (1983).
- [140] B. M. van Oerle and G. J. Ernst, *Appl. Opt.* **35**, 5177 (1996).
- [141] SPECS, *SPECS Pheibos 100 Electron Analyser Manual* (SPECS, p.^pp. 40).
- [142] SPECS, *SPECS Delay Line Detector Manual* (SPECS).
- [143] H. Viehhaus, *Materials and Corrosion* **38**, 404 (1987).

- [144] Wiki Commons LEED, https://en.wikipedia.org/wiki/Low-energy_electron_diffraction#/media/File:LEED_Experimental_Diagram.jpg.
- [145] R. A. Bennett, P. Stone, N. J. Price, and M. Bowker, *Physical Review Letters* **82**, 3831 (1999).
- [146] M. Blanco-Rey, J. Abad, C. Rogero, J. Mendez, M. F. Lopez, J. A. Martin-Gago, and P. L. de Andres, *Physical Review Letters* **96**, 055502 (2006).
- [147] C. M. Yim, C. L. Pang, and G. Thornton, *Surface Science* **650**, 71 (2016).
- [148] Agilent, *Varian Dry Scroll Pump Manual* (Agilent, p. 31).
- [149] Pfeiffer, *Pfeiffer Vacuum Turbopump Manual* (Pfeiffer).
- [150] Ion Pump Figure, http://www.lesker.com/newweb/vacuum_pumps/vacuumpumps_technicalnotes_1.cfm.
- [151] R. A. Bennett, S. Poulston, P. Stone, and M. Bowker, *Physical Review B* **59**, 10341 (1999).
- [152] D. M. Adams *et al.*, *The Journal of Physical Chemistry B* **107**, 6668 (2003).
- [153] J. i. Kanasaki, H. Tanimura, and K. Tanimura, *Physical Review Letters* **113**, 237401 (2014).
- [154] J. B. Asbury, E. Hao, Y. Wang, H. N. Ghosh, and T. Lian, *The Journal of Physical Chemistry B* **105**, 4545 (2001).
- [155] T. Yoshihara, R. Katoh, A. Furube, Y. Tamaki, M. Murai, K. Hara, S. Murata, H. Arakawa, and M. Tachiya, *The Journal of Physical Chemistry B* **108**, 3817 (2004).
- [156] E. Hendry, F. Wang, J. Shan, T. F. Heinz, and M. Bonn, *Phys. Rev. B* **69**, 081101 (2004).
- [157] Y. Tamaki, A. Furube, M. Murai, K. Hara, R. Katoh, and M. Tachiya, *J. Am. Chem. Soc.* **128**, 416 (2006).
- [158] Y. Tamaki, A. Furube, M. Murai, K. Hara, R. Katoh, and M. Tachiya, *Physical Chemistry Chemical Physics* **9**, 1453 (2007).
- [159] F. J. Knorr, C. C. Mercado, and J. L. McHale, *J. Phys. Chem. C* **112**, 12786 (2008).
- [160] Y. Tamaki, K. Hara, R. Katoh, M. Tachiya, and A. Furube, *J. Phys. Chem. C* **113**, 11741 (2009).
- [161] T. Nomoto, A. Sasahara, and H. Onishi, *J Chem Phys* **131**, 084703 (2009).
- [162] R. Katoh, M. Murai, and A. Furube, *Chemical Physics Letters* **500**, 309 (2010).
- [163] K. Ishioka and H. Petek, *Phys. Rev. B* **86**, 205201 (2012).
- [164] E. M. Bothschafter, A. Paarmann, E. S. Zijlstra, N. Karpowicz, M. E. Garcia, R. Kienberger, and R. Ernstorfer, *Phys. Rev. Lett.* **110**, 067402 (2013).
- [165] J. T. Yates and H. Petek, *Chemical Reviews* **106**, 4113 (2006).
- [166] H. Petek and J. Zhao, *Chemical Reviews* **110**, 7082 (2010).
- [167] D. Ino, K. Watanabe, N. Takagi, and Y. Matsumoto, *J. Phys. Chem. B* **109**, 18018 (2005).
- [168] L. Gundlach, R. Ernstorfer, and F. Willig, *Phys. Rev. B* **74**, 035324 (2006).
- [169] L. Gundlach, J. Szarko, L. D. Socaciu-Siebert, A. Neubauer, R. Ernstorfer, and F. Willig, *Phys. Rev. B* **75**, 125320 (2007).
- [170] V. P. Zhukov and E. V. Chulkov, *Journal of physics. Condensed matter : an Institute of Physics journal* **22**, 435802 (2010).
- [171] K. Ali, *Physica Scripta* **90**, 025804 (2015).
- [172] W. A. Tisdale, M. Muntwiler, D. J. Norris, E. S. Aydil, and X. Y. Zhu, *The Journal of Physical Chemistry C* **112**, 14682 (2008).
- [173] J. C. Deinert, D. Wegkamp, M. Meyer, C. Richter, M. Wolf, and J. Stähler, *Physical Review Letters* **113**, 057602 (2014).
- [174] R. Huber, J.-E. Moser, M. Grätzel, and J. Wachtveitl, *The Journal of Physical Chemistry B* **106**, 6494 (2002).
- [175] V. Eyert, *Annalen der Physik* **11**, 650 (2002).
- [176] N. B. Aetukuri *et al.*, *Nat Phys* **9**, 661 (2013).
- [177] D. Wegkamp *et al.*, *Physical Review Letters* **113**, 216401 (2014).

- [178] D. A. Panayotov, S. P. Burrows, and J. R. Morris, *The Journal of Physical Chemistry C* **116**, 4535 (2012).
- [179] K. Vos, *J. Phys. Chem.* **10**, 3917 (1977).
- [180] V. E. Henrich, *Progress in Surface Science* **9**, 143 (1979).
- [181] J. Zhao, B. Li, K. D. Jordan, J. Yang, and H. Petek, *Phys. Rev. B* **73**, 195309 (2006).
- [182] M. V. Khomenko, K. Langer, H. Rager, and A. Fett, *Physics and Chemistry of Minerals* **25**, 338.
- [183] L. A. Grunes, *Physical Review B* **27**, 2111 (1983).
- [184] L. Fleming, C. C. Fulton, G. Lucovsky, J. E. Rowe, M. D. Ulrich, and J. Lüning, *J. Appl. Phys.* **102**, 033707 (2007).
- [185] A. Migani, D. J. Mowbray, J. Zhao, H. Petek, and A. Rubio, *Journal of Chemical Theory and Computation* **10**, 2103 (2014).
- [186] W. Kang and M. S. Hybertsen, *Phys. Rev. B* **82**, 085203 (2010).
- [187] M. S. Hybertsen and S. G. Louie, *Physical Review B* **34**, 5390 (1986).
- [188] B. A. Ruzicka, L. K. Werake, H. Samassekou, and H. Zhao, *Applied Physics Letters* **97**, 262119 (2010).
- [189] J. P. Perdew, K. Burke, and M. Ernzerhof, *Physical Review Letters* **77**, 3865 (1996).
- [190] <http://link.aps.org/supplemental/10.1103/PhysRevB.91.155429>.
- [191] Z. Wang *et al.*, *Journal of the American Chemical Society* **137**, 9146 (2015).
- [192] Y. Zhang, D. T. Payne, C. L. Pang, H. H. Fielding, and G. Thornton, *The Journal of Physical Chemistry Letters* **6**, 3391 (2015).
- [193] M. Cardona, *Solid State Commun.* **133**, 3 (2005).
- [194] J. Zhao, B. Li, K. Onda, M. Feng, and H. Petek, *Chem. Rev.* **106**, 4402 (2006).
- [195] N. G. Petrik and G. A. Kimmel, *J. Phys. Chem. C* **119**, 23059 (2015).
- [196] S. Wendt *et al.*, *Surf. Sci.* **598**, 226 (2005).
- [197] Z. Zhang, O. Bondarchuk, B. D. Kay, J. M. White, and Z. Dohnálek, *J. Phys. Chem. B* **110**, 21840 (2006).
- [198] X. Cui, Z. Wang, S. Tan, B. Wang, J. Yang, and J. G. Hou, *J. Phys. Chem. C* **113**, 13204 (2009).
- [199] M. A. Henderson, W. S. Epling, C. L. Perkins, C. H. F. Peden, and U. Diebold, *J. Phys. Chem. B* **103**, 5328 (1999).
- [200] Z. Zhang, Y. Du, N. G. Petrik, G. A. Kimmel, I. Lyubinetsky, and Z. Dohnálek, *The Journal of Physical Chemistry C* **113**, 1908 (2009).
- [201] E. Lira, J. ÿ. Hansen, P. Huo, R. Bechstein, P. Galliker, E. LÊgsgaard, B. r. Hammer, S. Wendt, and F. Besenbacher, *Surf. Sci.* **604**, 1945 (2010).
- [202] N. G. Petrik and G. A. Kimmel, *J. Phys. Chem. Lett.* **2**, 2790 (2011).
- [203] M. A. Henderson, *Surf. Sci.* **419**, 174 (1999).
- [204] Q. Guo, I. Cocks, and E. M. Williams, *J. Chem. Phys.* **106**, 2924 (1997).
- [205] C. M. Yim, C. L. Pang, and G. Thornton, *Phys. Rev. Lett.* **104**, 259704 (2010).
- [206] G. Drera, G. Salvinelli, A. Brinkman, M. Huijben, G. Koster, H. Hilgenkamp, G. Rijnders, D. Visentin, and L. Sangaletti, *Phys. Rev. B* **87**, 075435 (2013).
- [207] M. P. Seah and W. A. Dench, *Surf. Interface Anal.* **1**, 2 (1979).
- [208] Z. Wang *et al.*, *J. Am. Chem. Soc.* **137**, 9146 (2015).
- [209] F. Bisio, M. Nývlt, J. Franta, H. Petek, and J. Kirschner, *Physical Review Letters* **96**, 087601 (2006).
- [210] A. Yamakata, T.-a. Ishibashi, and H. Onishi, *J. Mol. Catal. A* **199**, 85 (2003).
- [211] Z. Zhang and J. T. Yates, *Chemical Reviews* **112**, 5520 (2012).
- [212] M. J. Weida, S. Ogawa, H. Nagano, and H. Petek, *J. Opt. Soc. Am. B* **17**, 1443 (2000).
- [213] P. Rossitza and E. P. Warren, *J. Phys.: Condens. Matter* **22**, 043001 (2010).
- [214] W. Meevasana, P. D. C. King, R. H. He, S. K. Mo, M. Hashimoto, A. Tamai, P. Songsiriritthigul, F. Baumberger, and Z. X. Shen, *Nat Mater* **10**, 114 (2011).

- [215] G. Cheng *et al.*, *Nature* **521**, 196 (2015).
- [216] Z. Jin, H. Ma, G. Li, Y. Xu, G. Ma, and Z. Cheng, *Appl. Phys. Lett.* **100**, 021106 (2012).
- [217] J. Vura-Weis, C.-M. Jiang, C. Liu, H. Gao, J. M. Lucas, F. M. F. de Groot, P. Yang, A. P. Alivisatos, and S. R. Leone, *J. Phys. Chem. Lett.* **4**, 3667 (2013).
- [218] M. M. Waegele, H. Q. Doan, and T. Cuk, *J. Phys. Chem. C* **118**, 3426 (2014).
- [219] D. Wegkamp and J. Stähler, *Prog. Surf. Sci.* **90**, 464 (2015).
- [220] A. Janotti, C. Franchini, J. B. Varley, G. Kresse, and C. G. Van de Walle, *physica status solidi (RRL) – Rapid Research Letters* **7**, 199 (2013).
- [221] T. Shibuya, K. Yasuoka, S. Mirbt, and B. Sanyal, *Journal of physics. Condensed matter : an Institute of Physics journal* **24**, 435504 (2012).
- [222] H. Sezen, M. Buchholz, A. Nefedov, C. Natzeck, S. Heissler, C. Di Valentin, and C. Wöll, *Scientific Reports* **4**, 3808 (2014).
- [223] C. Spreafico and J. VandeVondele, *Physical chemistry chemical physics : PCCP* **16**, 26144 (2014).
- [224] D. M. Savory and A. J. McQuillan, *The Journal of Physical Chemistry C* **118**, 13680 (2014).
- [225] S. Yang, A. T. Brant, N. C. Giles, and L. E. Halliburton, *Physical Review B* **87**, 125201 (2013).
- [226] C. M. Yim, M. B. Watkins, M. J. Wolf, C. L. Pang, K. Hermansson, and G. Thornton, *Physical Review Letters* **117**, 116402 (2016).
- [227] M. Cardona, *Solid State Communications* **133**, 3 (2005).
- [228] A. Marini, *Physical Review Letters* **101**, 106405 (2008).
- [229] A. Yildiz, F. Iacomi, and D. Mardare, *Journal of Applied Physics* **108**, 083701 (2010).
- [230] C. Di Valentin and A. Selloni, *The Journal of Physical Chemistry Letters* **2**, 2223 (2011).
- [231] B. J. Morgan, D. O. Scanlon, and G. W. Watson, *Journal of Materials Chemistry* **19**, 5175 (2009).
- [232] A. Fujimori, A. E. Bocquet, K. Morikawa, K. Kobayashi, T. Saitoh, Y. Tokura, I. Hase, and M. Onoda, *Journal of Physics and Chemistry of Solids* **57**, 1379 (1996).
- [233] S. J. F. Byrnes, (University of California Berkeley, University of California Berkeley, 2008), pp. 1.
- [234] J. T. Devreese, *Encyclopedia of Applied Physics* (Wiley, 1996), Vol. 14, p. 383-409.
- [235] E. M. Lifshitz, *Soviet Physics Uspekhi* **12**, 135 (1969).
- [236] H. Fröhlich, H. Pelzer, and S. Zienau, *The London, Edinburgh, and Dublin Philosophical Magazine and Journal of Science* **41**, 221 (1950).
- [237] K. G. Rana, T. Yajima, S. Parui, A. F. Kemper, T. P. Devereaux, Y. Hikita, H. Y. Hwang, and T. Banerjee, *Scientific Reports* **3**, 1274 (2013).
- [238] D. Rønnow, L. F. Lastras-Martínez, and M. Cardona, *The European Physical Journal B - Condensed Matter and Complex Systems* **5**, 29 (1998).
- [239] M. Wang, C. Bi, L. Li, S. Long, Q. Liu, H. Lv, N. Lu, P. Sun, and M. Liu, *Nature Communications* **5**, 4598 (2014).
- [240] A. A. S. Salje E.K., Liang W.Y, *Polarons and Bipolarons in High Tc Superconductors* 2005).
- [241] H. M. Rønnow, C. Renner, G. Aeppli, T. Kimura, and Y. Tokura, *Nature* **440**, 1025 (2006).
- [242] K. P. McKenna, M. J. Wolf, A. L. Shluger, S. Lany, and A. Zunger, *Physical Review Letters* **108**, 116403 (2012).
- [243] J.-F. Jerratsch, X. Shao, N. Nilius, H.-J. Freund, C. Popa, M. V. Ganduglia-Pirovano, A. M. Burow, and J. Sauer, *Physical Review Letters* **106**, 246801 (2011).
- [244] A. C. Papageorgiou, N. S. Beglitis, C. L. Pang, G. Teobaldi, G. Cabailh, Q. Chen, A. J. Fisher, W. A. Hofer, and G. Thornton, *Proceedings of the National Academy of Sciences* **107**, 2391 (2010).
- [245] J. Miranda, T. Mertelj, V. Kabanov, and D. Mihailovic, *Physical Review B* **83**, 125308 (2011).
- [246] A. C. Luntz, V. Viswanathan, J. Voss, J. B. Varley, J. K. Nørskov, R. Scheffler, and A. Speidel, *The Journal of Physical Chemistry Letters* **4**, 3494 (2013).
- [247] F. Ortmann, F. Bechstedt, and K. Hannewald, *Physical Review B* **79**, 235206 (2009).
- [248] N. A. Deskins and M. Dupuis, *Physical Review B* **75**, 195212 (2007).

- [249] L. Yan, J. E. Elenewski, W. Jiang, and H. Chen, *Physical Chemistry Chemical Physics* **17**, 29949 (2015).
- [250] C. Di Valentin and A. Selloni, *J. Phys. Chem. Lett.* **2**, 2223 (2011).
- [251] S. Moser *et al.*, *Physical Review Letters* **110**, 196403 (2013).
- [252] P. Deák, B. Aradi, and T. Frauenheim, *Physical Review B* **92**, 045204 (2015).
- [253] D. Berger, H. Oberhofer, and K. Reuter, *Physical Review B* **92**, 075308 (2015).
- [254] N. A. Deskins, R. Rousseau, and M. Dupuis, *The Journal of Physical Chemistry C* **113**, 14583 (2009).
- [255] M. Setvin, C. Franchini, X. Hao, M. Schmid, A. Janotti, M. Kaltak, C. G. Van de Walle, G. Kresse, and U. Diebold, *Physical Review Letters* **113**, 086402 (2014).
- [256] C. L. Pang, R. Lindsay, and G. Thornton, *Chem. Soc. Rev.* **37**, 2328 (2008).
- [257] N. A. Deskins, R. Rousseau, and M. Dupuis, *J. Phys. Chem. C* **114**, 5891 (2010).
- [258] C. Di Valentin, G. Pacchioni, and A. Selloni, *J. Phys. Chem. C* (2009).
- [259] G. Mattioli, P. Alippi, F. Filippone, R. Caminiti, and A. Amore Bonapasta, *The Journal of Physical Chemistry C* **114**, 21694 (2010).
- [260] B. J. Morgan and G. W. Watson, *The Journal of Physical Chemistry C* **114**, 2321 (2010).
- [261] E. Finazzi, C. Di Valentin, and G. Pacchioni, *The Journal of Physical Chemistry C* **113**, 3382 (2009).
- [262] K. Onda, B. Li, and H. Petek, in *Ultrafast Phenomena XIV*, edited by T. O. T. Kobayashi, T. Kobayashi, K. Nelson, and S. De Silvestri (Springer-Verlag, Berlin, 2005), pp. 416.
- [263] P. G. Moses, A. Janotti, C. Franchini, G. Kresse, and C. G. Van de Walle, *J. Appl. Phys.* **119**, 181503 (2016).
- [264] C. Lin, D. Shin, and A. A. Demkov, *Journal of Applied Physics* **117**, 225703 (2015).
- [265] Previously this was reported as 2.7 and 2.85 eV. However due to a calibration error in our spectrometer this has now been corrected to the stated values.
- [266] N. A. Deskins, R. Rousseau, and M. Dupuis, *The Journal of Physical Chemistry C* **115**, 7562 (2011).
- [267] T. Shibuya, K. Yasuoka, S. Mirbt, and B. Sanyal, *The Journal of Physical Chemistry C* **118**, 9429 (2014).
- [268] P. Deák, B. Aradi, and T. Frauenheim, *Physical Review B* **86**, 195206 (2012).
- [269] M. Cardona, *Science and Technology of Advanced Materials* **7**, **Supplement 1**, S60 (2006).
- [270] P. B. Allen and M. Cardona, *Physical Review B* **23**, 1495 (1981).
- [271] P. B. Allen and V. Heine, *Journal of Physics C: Solid State Physics* **9**, 2305 (1976).
- [272] P. P. Edwards, *Journal of Superconductivity* **13**, 933 (2000).
- [273] N. F. Mott, *Physica A: Statistical Mechanics and its Applications* **200**, 127 (1993).
- [274] A. T. Brant *et al.*, *Physical Review B* **89**, 115206 (2014).
- [275] A. L. Linsebigler, G. Lu, and J. T. Yates, *Chem. Rev.* **95**, 735 (1995).
- [276] J. Raskó, *Catalysis Letters* **56**, 11 (1998).
- [277] J. Nowotny, T. Bak, M. K. Nowotny, and L. R. Sheppard, *International Journal of Hydrogen Energy* **32**, 2651 (2007).
- [278] K. Kočí, L. Obalová, L. Matějová, D. Plachá, Z. Lacný, J. Jirkovský, and O. Solcová, *Appl. Catal. B* **89**, 494 (2009).
- [279] O. K. Varghese, M. Paulose, T. J. LaTempa, and C. A. Grimes, *Nano Lett.* **9**, 731 (2009).
- [280] D. C. Sorescu, *J. Chem. Phys.* **135**, 124701 (2011).
- [281] C. Zhou, Z. Ma, Z. Ren, X. Mao, D. Dai, and X. Yang, *Chemical Science* **2**, 1980 (2011).
- [282] X. Lang, W. Ma, C. Chen, H. Ji, and J. Zhao, *Accounts of Chemical Research* **47**, 355 (2013).
- [283] C. Xu, W. Yang, Q. Guo, D. Dai, M. Chen, and X. Yang, *Journal of the American Chemical Society* **136**, 602 (2013).
- [284] A. Argondizzo, S. Tan, and H. Petek, *The Journal of Physical Chemistry C* **120**, 12959 (2016).
- [285] J. Zhao, B. Li, K. Onda, M. Feng, and H. Petek, *Chemical Reviews* **106**, 4402 (2006).

- [286] Z. Wang, Y. Zhao, X. Cui, S. Tan, A. Zhao, B. Wang, J. Yang, and J. G. Hou, *J. Phys. Chem. C* **114**, 18222 (2010).
- [287] H. Onishi, T. Aruga, C. Egawa, and Y. Iwasawa, *Surf. Sci.* **193**, 33 (1988).
- [288] L.-Q. Wang, K. F. Ferris, J. P. Winokur, A. N. Shultz, D. R. Baer, and M. H. Engelhard, *J. Vac. Sci. Tech. A* **16**, 3034 (1998).
- [289] C. Zhou *et al.*, *Chem. Sci.* **1**, 575 (2010).
- [290] T. Kawai and T. Sakata, *Journal of the Chemical Society, Chemical Communications*, 694 (1980).
- [291] Q. Guo, C. Xu, Z. Ren, W. Yang, Z. Ma, D. Dai, H. Fan, T. K. Minton, and X. Yang, *Journal of the American Chemical Society* **134**, 13366 (2012).
- [292] R. S. n. de Armas, J. Oviedo, M. A. San Miguel, and J. F. Sanz, *The Journal of Physical Chemistry C* **111**, 10023 (2007).
- [293] D. A. Panayotov, P. A. DeSario, J. J. Pietron, T. H. Brintlinger, L. C. Szymczak, D. R. Rolison, and J. R. Morris, *J. Phys. Chem. C* **117**, 15035 (2013).
- [294] M. A. Henderson and I. Lyubinetsky, *Chemical Reviews* **113**, 4428 (2013).
- [295] Z. Li, R. S. Smith, B. D. Kay, and Z. Dohnálek, *The Journal of Physical Chemistry C* **115**, 22534 (2011).
- [296] M. A. Henderson, S. Otero-Tapia, and M. E. Castro, *Faraday Discuss.* **114**, 313 (1999).
- [297] J. Zhao, J. Yang, and H. Petek, *Phys. Rev. B* **80**, 235416 (2009).
- [298] J. Matthiesen, R. S. Smith, and B. D. Kay, *Physical Review Letters* **103**, 245902 (2009).
- [299] R. S. Smith, J. Matthiesen, and B. D. Kay, *The Journal of Physical Chemistry A* **118**, 8242 (2014).
- [300] M. A. Henderson, S. Otero-Tapia, and M. E. Castro, *Faraday Discussions* **114**, 313 (1999).
- [301] D. A. Bennett, M. Cargnello, T. R. Gordon, C. B. Murray, and J. M. Vohs, *Physical chemistry chemical physics : PCCP* **17**, 17190 (2015).
- [302] R. Wang and H. Fan, *Science China Chemistry* **58**, 614 (2015).
- [303] T. Sugimoto, N. Aiga, Y. Otsuki, K. Watanabe, and Y. Matsumoto, *Nat Phys* **12**, 1063 (2016).
- [304] K. Shirai, T. Sugimoto, K. Watanabe, M. Haruta, H. Kurata, and Y. Matsumoto, *Nano Letters* **16**, 1323 (2016).
- [305] T. Minato, S. Kajita, C.-L. Pang, N. Asao, Y. Yamamoto, T. Nakayama, M. Kawai, and Y. Kim, *ACS Nano* **9**, 6837 (2015).
- [306] M. A. Henderson, S. Otero-Tapia, and M. E. Castro, *Surf. Sci.* **412-413**, 252 (1998).
- [307] B. Han, W. Wei, L. Chang, P. Cheng, and Y. H. Hu, *ACS Catalysis* **6**, 494 (2016).
- [308] S. Funk and U. Burghaus, *Phys. Chem. Chem. Phys.* **8**, 4805 (2006).
- [309] Y. Kohno, T. Yamamoto, T. Tanaka, and T. Funabiki, *Journal of Molecular Catalysis A: Chemical* **175**, 173 (2001).
- [310] S. Krischok, O. Höfft, and V. Kempter, *Surf. Sci.* **507-510**, 69 (2002).
- [311] J. Nerlov, S. V. Christensen, S. Weichel, E. H. Pedersen, and P. J. Møller, *Surf. Sci.* **371**, 321 (1997).
- [312] V. P. Indrakanti, J. D. Kubicki, and H. H. Schobert, *Energy Environ. Sci.* **2**, 745 (2009).
- [313] V. P. Indrakanti, H. H. Schobert, and J. D. Kubicki, *Energy Fuels* **23**, 5247 (2009).
- [314] J. Rasko and F. Solymosi, *The Journal of Physical Chemistry* **98**, 7147 (1994).
- [315] M. A. Henderson, *Surface Science* **400**, 203 (1998).
- [316] T. L. Thompson, O. Diwald, and J. T. Yates, *The Journal of Physical Chemistry B* **107**, 11700 (2003).
- [317] T. L. Thompson and J. T. Yates, *Topics in Catalysis* **35**, 197 (2005).
- [318] X. Lin *et al.*, *J. Phys. Chem. C* **116**, 26322 (2012).
- [319] M. A. Henderson, *Surf. Sci.* **400**, 203 (1998).
- [320] T. L. Thompson, O. Diwald, and J. T. Yates, *J. Phys. Chem. B* **107**, 11700 (2003).
- [321] T. L. Thompson and J. T. Yates, Jr., *J. Phys. Chem. B* **110**, 7431 (2006).

- [322] Z. Zhang and J. T. Yates, *The Journal of Physical Chemistry Letters* **1**, 2185.
- [323] C. L. Perkins and M. A. Henderson, *The Journal of Physical Chemistry B* **105**, 3856 (2001).
- [324] D. Sporleder, D. P. Wilson, and M. G. White, *J. Phys. Chem. C* **113**, 13180 (2009).
- [325] A. Yamakata, T.-a. Ishibashi, and H. Onishi, *J. Phys. Chem. B* **105**, 7258 (2001).
- [326] M. Setvín, U. Aschauer, P. Scheiber, Y.-F. Li, W. Hou, M. Schmid, A. Selloni, and U. Diebold, *Science* **341**, 988 (2013).
- [327] G. A. Kimmel and N. G. Petrik, *Physical Review Letters* **100**, 196102 (2008).
- [328] N. G. Petrik, Z. Zhang, Y. Du, Z. Dohnálek, I. Lyubinetzky, and G. A. Kimmel, *The Journal of Physical Chemistry C* **113**, 12407 (2009).
- [329] M. A. Henderson, M. Shen, Z.-T. Wang, and I. Lyubinetzky, *The Journal of Physical Chemistry C* **117**, 5774 (2013).
- [330] B. Michael and A. B. Roger, *Journal of Physics: Condensed Matter* **21**, 474224 (2009).
- [331] O. Bikondoa, C. L. Pang, R. Ithnin, C. A. Muryn, H. Onishi, and G. Thornton, *Nat. Mater.* **5**, 189 (2006).
- [332] Y. Du, Z. Dohnálek, and I. Lyubinetzky, *The Journal of Physical Chemistry C* **112**, 2649 (2008).
- [333] W. S. Epling, C. H. F. Peden, M. A. Henderson, and U. Diebold, *Surf. Sci.* **412-413**, 333 (1998).